

ABSTRACT

Title of Dissertation: DYNAMICS OF GLOBAL SURFACE
WATER 1999 - PRESENT

Amy Hudson Pickens,
Doctor of Philosophy, 2021

Dissertation directed by: Professor Matthew C. Hansen,
Department of Geographical Sciences

Inland surface waters are critical to life, supplying fresh water and habitat, but are constantly in flux. There have been considerable advances in surface water monitoring over the last decade, though the extent of surface water has not been well-quantified per international reporting standards. Global characterizations of change have been primarily bi-temporal. This is problematic due to significant areas with multi-year cycles of wet and dry periods or anomalous high water or drought years. Many areas also exhibit strong seasonal fluctuations, such as floodplains and other natural wetlands. This dissertation aims to characterize open surface water extent dynamics by employing all of the Landsat archive 1999-present, and to report area estimates with associated uncertainty measures as required by policy guidelines. From 1999 to 2018, the extent of permanent water (in liquid or ice state) was 2.93 (standard error ± 0.09) million km², representing only 60.82 (± 1.93)% of the total area that had water for some duration of the period. The unidirectional loss and gain areas

were relatively small, accounting for only 1.10 (± 0.23)% and 2.87 (± 0.58)% of total water area, respectively. The area that transitioned multiple times between water and land states on an annual scale was over four times larger (19.74 (± 2.16)%), totaling 0.95 (± 0.10) million km², establishing the need to evaluate the time-series from the entire period to assess change dynamics. From a seasonal perspective, June has over double the amount of open surface water as January, with 3.91 (± 0.19) million km² and 1.59 (± 0.21) million km², respectively. This is due to the vast network of lakes and rivers across the high-latitudes of the northern hemisphere that freeze over during the winter, with a maximum extent of ice over areas of permanent and seasonal water in February, totaling 2.49 (± 0.25) million km². This is the first global study to estimate the areas of extent and change with associated uncertainty measures and evaluate the seasonal dynamics of surface water and ice in a combined analysis. The methods developed here provide a framework for continuing to evaluate past trends and monitoring current dynamics of surface water and ice.

DYNAMICS OF GLOBAL SURFACE WATER 1999 - PRESENT

by

Amy Hudson Pickens

Dissertation submitted to the Faculty of the Graduate School of the
University of Maryland, College Park, in partial fulfillment
of the requirements for the degree of
Doctor of Philosophy
2021

Advisory Committee:

Dr. Matthew C. Hansen, Chair

Dr. Peter V. Potapov

Dr. Tatiana Loboda

Dr. Jonathan Higgins

Dr. Joseph Sullivan

© Copyright by
Amy Hudson Pickens
2021

Dedication

soli Deo gloria

Acknowledgements

Thank you to my committee, Matt Hansen, Peter Potapov, Tatiana Laboda, Jonathan Higgins, and Joe Sullivan. In particular, thank you, Matt. Your storytelling, deep knowledge, and enthusiasm ignited a love of geography in me as well. I have loved the many hours brainstorming in your office and your friendship through the years. Thank you for your patient mentoring. Thank you, Peter, for enabling so much of this research through your knowledge of big data processing and the many scripts you have shared, and for sharing travels around the world. Tatiana and Jonathan, you have spurred me explore new directions and our conversations have led to more impactful research, thank you. And thank you, Joe, for your service.

Thank you to the co-authors of this research, who have helped shape and enable it.

I am so grateful for all the dear people of GLAD past and present and the Hartwick Hawks, who have made this process a lot of fun, who I have gotten to share research and life with, and who have shaped me. Thank you, Viviana, Qing, Diana, Janet, Kris and so very many others.

Thank you to my dear friends and church family who have shared my joys and sorrows as we walk through this life together. Thank you for the adventures and long conversations. Thank you, Dad, for your love, curiosity, understanding of the process, and help in so many things that were new to me.

Jon, thank you. I am so grateful to be married to you and to share all of life together. Thank you for the immensity of your love and how you have sacrificed for

me. Thank you for your abundant support of me and my work, and how you point me to what is better. I love you, Jonny.

To the God of all, who alone can “measure the waters in the hollow of his hand” and who carries me close to his heart where no one can snatch me out of his hand (Isaiah 40, John 10), thank you—for everything.

Table of Contents

Dedication.....	ii
Acknowledgements.....	iii
Table of Contents.....	v
List of Tables.....	vii
List of Figures.....	viii
Chapter 1: Introduction.....	1
1.1 Importance of water monitoring and current progress.....	1
1.1.1 The dynamic nature and value of surface water.....	1
1.1.2 International call for monitoring changes in surface water.....	4
1.1.3 Remote sensing of surface water.....	5
1.1.4 Area estimation.....	12
1.2. Dissertation research objectives and structure.....	13
Chapter 2: Ensemble approach for Landsat water detection with sub-pixel evaluation.....	17
Abstract.....	17
2.1. Introduction.....	18
2.2 Methods.....	19
2.2.1 Scene classification.....	19
2.2.2 Sample-based assessment.....	22
2.3 Results.....	28
2.4 Discussion.....	30
2.5 Conclusion.....	31
Chapter 3: Mapping and sampling to characterize global inland water dynamics from 1999 to 2018 with full Landsat time-series.....	33
Abstract.....	33
3.1 Introduction.....	34
3.2 Methods.....	38
3.2.1 Creation of annual percent water time-series.....	38
3.2.2 Dynamic type classification.....	39
3.2.3 Dynamic class mapping.....	42
3.2.4 Landsat time-series sample.....	45
3.2.5 Comparison with Pekel et al. (2016) dataset.....	50
3.3 Results.....	53
3.3.1 Maps.....	53
3.3.2 Sample-based area estimates.....	56
3.3.3 Accuracy of classes of water dynamics derived from time-series.....	58
3.4 Discussion.....	64
3.4.1 Area comparison.....	66
3.4.2 Maps.....	71
3.5 Conclusion.....	72
Chapter 4: Global seasonal inland water and ice dynamics.....	74

Abstract.....	74
4.1 Introduction.....	75
4.2 Methods.....	78
4.2.1 Sample-based assessment	78
4.2.2 Landsat time-series	83
4.3 Results.....	86
4.3.1 Area estimates.....	86
4.3.2 Accuracy	90
4.3.3 10m vs 30m reference data area estimates.....	92
4.4 Discussion.....	93
4.4.1 Water and ice dynamics.....	93
4.4.2 Seasonal surface water.....	97
4.4.3 Future monitoring	98
4.5 Conclusion	100
Chapter 5: Conclusion.....	102
5.1 Summary of contributions.....	102
5.2 Potential improvements and outstanding issues	105
5.3 Future research.....	107
5.4 Conclusion	111
Appendices.....	112
A.I Area estimation of water dynamics classes	112
A.II Accuracy estimation of water dynamics classes	113
Bibliography	115

List of Tables

Table 3.1: Area estimates of trends with associated uncertainty of open water within the continental area between 75°N and 56°S as delineated by the Global Administrative Areas dataset (University of California, Berkeley 2012) and excluding Greenland. The last four categories are aggregates of the classes above.	57
Table 3.2: The user's and producer's accuracies of the classes of water dynamics from the time-series data of this study and of Pekel et al. (2016) when the water dynamics model is applied to each monthly water history dataset and to the reference data. The last four categories are aggregates of the classes above and a sample pixel is considered correct for the aggregate if it is in one of the contributing classes. See Table 3.1 for class definitions.	60
Table 3.3: Confusion matrix of GLAD water dynamics map with the reference classification. In row i and column j , the left half of the cell represents in a gray gradient the estimated percent of pixels labeled i in the reference data and that were mapped j in GLAD, and the right half of the cell represents in a green gradient the estimated percent of pixels mapped j in GLAD that were labeled i in the reference data. The grays not along the center diagonal of correct classification show the distribution of omission and the greens show the distribution of commission. The percent estimates were derived from the estimated area of each (i,j) cell.	61
Table 3.4: Confusion matrix of Pekel et al. (2016) transition map 1999-2018 with the reference classification. In row i and column j , the left half of the cell represents in a gray gradient the estimated percent of pixels labeled i in the reference data and that were mapped j by Pekel et al. (2016), and the right half of the cell represents in an orange gradient the estimated percent of pixels mapped j by Pekel et al. (2016) that were labeled i in the reference data. The percent estimates were derived from the estimated area of each (i,j) cell.	63

List of Figures

Figure 1.1: Outline of dissertation. 14

Figure 2.1: Distribution of strata and sampled blocks for 5m assessment. The thresholds of the percent of block area covered by surface water for the very low, low, medium, and high strata are 0%, 0-0.08%, 0.08%-2%, and >2%..... 24

Figure 2.2: Zoom within a sample block in the high water stratum. Top-left: RapidEye data (NIR-Red Edge-Red) from August 21, 2013. Top-middle: Landsat data (SWIR1-NIR-Red) from August 15, 2013. Top-right: Landsat data (SWIR1-NIR-Red) from August 24, 2013. Bottom-left: 5m RapidEye classification of water and land with the distance to the closest water-land boundary, the blue gradients are classified as water and the gray gradients are classified as land. Bottom-middle: GLAD percent water for August 2013. Bottom-right: Pekel et al. (2016) not water and water classification for August 2013. Image centered at 46.52°N, 31.84°E on the Ukrainian coast of the Black Sea. 27

Figure 2.3: Error rates at 5m resolution of the monthly Landsat water detection as a function of distance from the land-water boundary as defined in the 5m reference data. Top: The left half of the figure has distances extending further into land and displays commission error rates of water for both this study and Pekel et al. (2016) and the right half has distances extending further into water bodies and displays omission error rates of water. Each vertical line represents 30m from the land-water boundary. The space within 30m on either side of the land-water boundary represents the mixed pixel space at Landsat resolution. Bottom: The area within each stratum at the given distance from the land-water boundary. The area of water that the low and the very low water strata contribute drops off very quickly due to small water body size. There is no area at 0m because this is the boundary line between land and water. 30

Figure 3.1: Workflow of time-series analysis starting with the monthly water and land counts and resulting in dynamic class labels. 41

Figure 3.2: Examples of classes of the water dynamics map. Each example has the annual water percent time-series and resulting R-G-B reduction for a given pixel. For the stable seasonal and high frequency examples, the 17-year monthly mean water percent is also shown. (A) Dry period: Chicamba Real Dam, Mozambique. (B) Gain: Bakun Dam, Malaysia. (C) Stable seasonal: Meghna River floodplain, Bangladesh. (D) Loss: Razazza Lake, Iraq. (E) Wet period: Lake Gregory, Australia. (F) High frequency: Ob River floodplain, Russia..... 44

Figure 3.3: Distribution of sampled pixels of the Landsat time series. 46

Figure 3.4: Example sampled pixel from the wet period stratum, centered at 16.189375°N, 77.659375°E within the fluctuating footprint of Rayalumpad Reservoir

in Telangana, India. The reservoir was constructed in 2009, first flooded the sampled pixel in 2013 and remained flooded through 2015, and then seasonally inundated the sampled pixel 2016-2018. The pixel is outlined in red in each of the Landsat thumbnails (SWIR1-NIR-red) and in the images from Google Earth, with an additional yellow outline for the source UTM pixel footprint. The graphs at the top are time series of the spectral reflectance of the pixel to aid interpretation (Green reflectance in light green, red reflectance in red, NIR in black, SWIR1 in dark green, SWIR2 in purple, and NDWI in blue). Each Landsat scene could be individually marked as land, water, or bad data or a month, year, or the whole collection could be labeled as one of these classes. The full reference html page includes all months and years 1999-2018 and can be viewed here:

<https://glad.geog.umd.edu/timeSeriesReference/pagesUTM/sample419.html>. 49

Figure 3.5: 1999-2018 inter-annual water dynamics map examples for all 12 months with hues representing the type of change dynamic, saturation the intensity of the change, and value or brightness representing the maximum percent of a year that was inundated. All examples are shown at the same scale. (a) Expansion of aquaculture and shifting management practices on the coast of India. (b) Dramatic reduction of Lake Urmia in Iran, with slight recovery. (c) Increase of lakes across the Tibetan Plateau. (d) Shifting open water patterns in the Pantanal in Brazil, the largest wetland in the world. (e) Meandering of the Meghna River in Bangladesh by 10km and the growth of new islands in the Bay of Bengal. 54

Figure 3.6: 1999-2018 seasonal water examples. Both examples are shown at the same scale. Left: R-G-B of monthly mean water percent of April-June-August showing the seasonal floodplains of the Ob River, Russia. Right: R-G-B of monthly mean water percent of June-August-October showing the various rice and aquaculture flooding cycles in the Mekong Delta, Vietnam with the magenta areas experiencing two separate open water flooding periods and the green areas experiencing three separate open water flooding periods. 55

Figure 3.7: Global area estimates from this study and other previously published studies based on Landsat data. Each estimate from this study is the area with open water for the given percent of the year, and the gray area bounding it corresponds to the standard error of the estimate. Confidence intervals were not provided for the other studies. 68

Figure 4.1: Stratification represented in geographic projection..... 79

Figure 4.2: Example of Sentinel-2 and PlanetScope data for a selected cluster of 10m sample pixels centered at 173.3305011°W, 64.2007883°N. Since there is a mix of land and water in the 30m cluster, this sample was interpreted using the 3m Planet labs data. The 30m cluster is identified with a red outline in the Sentinel-2 image and the 10m pixels with a yellow outline in the PlanetScope image..... 81

Figure 4.3: Area of open surface water surface water per month (km²). The regions with diagonal lines represent +/- one standard error (SE) of the single class total

beneath it. The uncertainty associated with the total area of water per month is represented by +/- one SE. 87

Figure 4.4: Area of ice cover per month (km²) over permanent water bodies and areas that had seasonal water presence. The regions with diagonal lines represent +/- one standard error (SE) of the single class total beneath it. The uncertainty associated with the total area of ice per month is represented by +/- one SE. 88

Figure 4.5: Month of ice melt, month of freeze, and the number of months with ice cover for permanent water bodies $\geq 40^\circ\text{N}$ aggregated with a mean function to roughly 5km resolution. 89

Figure 4.6: Accuracy of monthly water and ice maps. 91

Figure 4.7: Accuracy of binary maps of water presence $\geq X\%$ of the year. 91

Figure 4.8: Comparison of the area estimates of annual water extent for varying temporal percent thresholds for two different annual aggregation methods. The stacked area graph represents the extent of open liquid water present $\geq X\%$ of the entire year. The orange line represents the extent of water present $\geq X\%$ of the portion of the year without ice (ice is considered no-data), with the area estimate of 100% water equal to the combined area of permanent liquid water and permanent water that freezes. There is a widening difference between the two estimates, such that the previous practice of ignoring ice results in an estimate of 100% water that is 2.5x larger than the area of permanent liquid water. 94

Figure 4.9: Landsat derived month of ice melt over permanent water bodies for 2019 with many small lakes melting two months earlier than the large lakes. Centered on 125.5°W, 66.0°N..... 95

Figure 4.10: Map based areas from the Landsat time series. Area of no data for permanent water classes is most likely water, however, in the seasonal water classes, the no-data months could be water or land. 100

Chapter 1: Introduction

1.1 Importance of water monitoring and current progress

1.1.1 The dynamic nature and value of surface water

Intuitively, we all understand the importance of water. We cannot survive more than a few days without water. Earth has an abundance of water; however, the majority is held in the world's saltwater seas and oceans. Water is also found inland in underground aquifers, the soil, the atmosphere, and, of course, on the surface. While humans, plants, and animals acquire water from all these different sources, inland surface water is the most accessible to much of life. Despite this, it only covers about 3% of the continental surface (Pekel et al., 2016), with immense geographic variation leading to abundance and scarcity (Postel et al., 1996).

Surface water and the systems surrounding them are of immense value, providing critical ecosystem services. These include the direct use of water for human consumption, irrigation supply, and electricity generation, as well as the mitigating services of regulating flow and filtration of pollution (de Groot et al., 2012; Mitsch and Gosselink, 2015). Surface water and wetland ecosystems account for more than 20% of the total valuation of all global ecosystem service benefits and almost 40% of total terrestrial ecosystem service benefits (Costanza et al., 2014). Surface water also plays a significant role in local and global climate systems, storing immense amounts of carbon but also the source of more than a third of global methane emissions (Kayranli et al., 2010; Kirschke et al., 2013). Wetlands are among the most biodiverse

habitats, and seasonal waters are congregational spots for local and global animal migrations (Haig et al., 2019; Jin, 2008; Reid et al., 2019). While there are many lakes and rivers that remain mostly constant, much of the earth's surface water is in flux with many natural and human-induced dynamics (Papa et al., 2010; Pekel et al., 2016; Yamazaki et al., 2015).

There are vast floodplains that inundate annually across the tropics, including those of the Zambezi, Parana, Brahmaputra, and Amazon rivers, to the boreal, including the Ob and the Mackenzie rivers. Some floodplains have only short vegetation cover and the inundation dynamics can be clearly observed from above, whereas others, such as the Amazon River, occur primarily under dense tree canopies and cannot be observed from above. The periodic flooding is critical to maintaining ecosystem integrity, with many plant and animal species adapted to be dependent on those cycles (Poff et al., 1997). While there is increasing awareness of their value, floodplains are under intense human land use and are continuing to be regulated and converted (Tockner and Stanford 2002, Hansen et al. 2020 (forthcoming)). Though not well-quantified, vast areas of floodplains, deltas, and other natural wetlands have been engineered for food production (Davidson, 2014; Tessler et al., 2016; Zhao et al., 2008). Rivers have been harnessed to provide stable water supplies for irrigation and consumption, meet electricity demands, enable transportation, and minimize flood risk. As a result, over half of the river systems of the world are moderately to severely fragmented by dams, levees, and other structures (Grill et al. 2015), and only 37% of rivers >1000 km² are free-flowing (Grill et al., 2019). While providing many

benefits, these structures impede the rivers' natural flow, inundation cycles and extent.

The International Commission on Large Dams documents 58,713 dams with height >15m or with impoundments greater than three million m³ with thousands of additional large dams under construction or in advanced planning stages (Zarfl et al., 2015). However, there are many more smaller dams with 91,457 total dams inventoried in the United States alone (U.S. Army Corps of Engineers, 2018). Irrigation is the largest driver of reservoir construction, with half of large dams built for that purpose (International Commission on Large Dams, 2020). This diversion of water for irrigation is driving a decline of saline lakes globally (Wurtsbaugh et al., 2017). Additionally, due to high levels of extraction and low recharge, there is large-scale groundwater depletion in the major semi-arid agricultural areas of the world, including portions of central Asia, India, and the USA (Rodell et al., 2018). Humans are now a significant actor in the global water cycle, with human water use (green, blue, and gray) amounting to half of global river discharge to oceans and exceeding groundwater recharge (Abbott et al., 2019).

In addition to changes that affect water once it comes into a watershed, climate factors also affect the total amount of water available. As our climate system continues to gain energy, there is a global increasing temperature trend with the last six years being the warmest six on record (NOAA, 2020), but both the observed and modeled local temperature and precipitation trends vary in direction and magnitude around the world. Dai et al. (2009) found that a third of the largest 200 rivers globally had statistical increasing or decreasing trends over 1948-2004, with over twice as

many having a decreasing trend. Climate model simulations predict severe and widespread drought by the end of the century (Dai, 2013). Already four billion people are estimated to face water scarcity (Mekonnen and Hoekstra, 2016). Warming temperatures are also increasing glacier melt, which in the short term increases runoff, but leaves an uncertain future for river systems that rely on them (Chevallier et al., 2011; Lutz et al., 2014). Impacts are already seen in the Arctic with a documented increase in the ice-free season of lakes and rivers (Šmejkalová et al., 2016; Xiao Yang et al., 2020) and projections estimating a 15-50 day increase by late century (Dibike et al., 2011; Prowse et al., 2011) with feedback effects on climate (Wik et al., 2016).

1.1.2 International call for monitoring changes in surface water

Due to how important surface water systems are and yet how threatened they are, numerous international organizations have set monitoring and conservation targets. The United Nations set Sustainable Development Goal 6.6, “By 2020, protect and restore water-related ecosystems, including mountains, forests, wetlands, rivers, aquifers, and lakes”. This is a broad-reaching target with one indicator, Indicator 6.6.1: “the change in water-related ecosystems over time”, which has been further defined as the change in spatial extent, quantity, and quality of water over time (UN Water, 2018). The United Nations Conference on Biodiversity and the Ramsar Convention on Wetlands have also set targets for protecting inland water ecosystems (CBD, 2010; Rebelo et al., 2018).

The World Meteorological Organization has also issued a call to monitor the surface water and ice extent of lakes as Essential Climate Variables (ECV) (World

Meteorological Organization (WMO) et al., 2016). ECVs provide a long-term data record to monitor changes in the climate and the interactions of these changes with the land surface. WMO cites a need for both water and ice extent of lakes to be monitored daily with 20m resolution for water and 300m resolution for ice. These ambitious goals are far from being met, though there is limited progress towards these targets (Pekel et al., 2016; Xiao Yang et al., 2020).

To meet these global targets, Earth observation data must be employed. Unlike other land covers, such as agriculture or impervious surfaces, surface water is not a human land use and is often far from transportation networks, making field assessments difficult (Alsdorf et al., 2003). However, the rise of satellite imagery has given us the opportunity to observe and measure vast regions without ever visiting them (Wulder et al., 2019).

1.1.3 Remote sensing of surface water

Surface water is more distinct from other land covers and can be effectively mapped in a single observation, whereas, for many other land covers, particularly vegetation type mapping, a time-series is often critical. Water absorbs nearly all the radiation of the longer wavelengths, but can have different properties in the shorter wavelengths (Boland, 1976; Han et al., 1994; Rundquist and Han, 1994). During an algal bloom, surface water can appear bright green in the visual bands (Binding et al., 2013; Han et al., 1994), or, in a river with high sediment load in the upper water column, surface water can appear bright (Han and Rundquist, 1994). Additionally, factors such as water depth, submerged aquatic vegetation, or other water quality measures can affect the spectral reflectance (Boland, 1976). Exploiting the difference

in reflection of the long and short wavelengths, McFeeters (1996) developed the Normalized Difference Water Index (NDWI), which is the normalized difference ratio of the green and near-infrared reflectance, to identify water presence. To more accurately distinguish surface water from built-up areas Xu (2006) proposed the Modified NDWI (MNDWI), which is the normalized difference ratio of green and short wave infrared (1.55 to 1.75 μm) reflectance. Other indices employing the combination of more bands and ratios have been shown to have efficacy for different environments (Crist, 1985; Danaher and Collett, 2006; Feyisa et al., 2014; Wang et al., 2018). However, each proposed water index for monitoring water performs better or worse depending on each of these factors and on the surrounding land cover, with no one index always the most accurate (Fisher et al., 2016). Thus, it is valuable to employ numerous bands and indexes with a collection of thresholds through machine learning approaches or iterative evaluation (Fisher et al., 2016; Pekel et al., 2016; Tulbure et al., 2016).

Earth-observing satellite missions of recent decades and improved computing power enable global scale time-series analysis (Hansen et al., 2013; Pekel et al., 2016). The Landsat missions provide the longest consistent record of earth observation. Landsat 1 was launched in 1972, inaugurating a new era of earth studies. For the first time, users could see anywhere in the world with publicly available data. There have been improvements in the sensors' imaging and data transfer capabilities with each successive satellite, though the launch of Landsat 5 brought the advent of 30m resolution spectral data and a thermal band. The Landsat program went through changes in management from 1985-2003, resulting in variable data volumes with

some parts of the world having 5-8 year gaps and others not even being imaged until 1998 (Wulder et al., 2016). 1999 brought with it the launch of Landsat 7 and the institution of the Long Term Acquisition Plan, one of the most influential management changes in Landsat data provisioning began (Arvidson et al., 2006). This placed two comparable sensors in complementary orbits that enabled revisit rates of 8 days at the equator. However, due to data transfer limits, this was not actually obtained for most areas of the world, with Landsat 7 collecting <50% of potential sunlit land scenes per day and Landsat 5 even less (Wulder et al., 2016).

Unfortunately, Landsat 7 had a considerable setback in May 2003 with the failure of its scan line corrector. While some users have declined to use these data due to the striping that resulted, 78% of the data remain uncorrupted (Chen et al., 2011). The number and quality of Landsat images significantly increased with Landsat 8 in 2013. Landsat 8 brought much higher data transfer capabilities such that most areas of the world actually are imaged every 16 days, plus what is captured by Landsat 7. The OLI and TIRS sensors onboard also provide increased radiometric resolution of 12-bit data and additional spectral data with three new bands.

Free and open access data is critical to large scale studies. In 2008, all the data from the Landsat program was made freely available to the benefit of the world (Wulder et al., 2012). From 1982-2007, broad-scale studies were limited by the prohibitive cost of obtaining Landsat scenes. The cost per scene before the opening of the archive was \$600USD, down from the previous decade's cost of \$4400 (Wulder et al., 2012). Studies from the last decade would have been impossible at this rate; Hansen et al. (2013) would have cost half a billion dollars and Pekel et al. (2016)

would have cost multiple billion. It is estimated that in 2017 alone, the Landsat program provided \$3.45 billion in benefits (Straub et al., 2019).

Other public sensors were launched in the 1980s through the 2000s, but with much coarser spatial resolution, including AVHRR (1979-2019, 1.1km), MODIS TERRA and AQUA (1999 and 2002, 250-1000m), MERIS (2002, 300m). These sensors represent the tradeoff between spatial and temporal resolution with sub-daily to every three day revisit times. MODIS and MERIS also represent the tradeoff between spatial and spectral resolution with 36 and 15 bands, respectively. The improved temporal and spectral resolutions enable more detailed assessment of extensive landscape features, including large lakes. On a global scale, there are official MODIS annual water maps representing all areas with water cover $\geq 50\%$ of the year (Carroll et al., 2017). Klein et al. (2017) harnessed the daily revisit rate to create maps of the number of days of water presence for 2015, providing the densest global seasonal examination of surface water presence. However, surface water has many fine-scale features, with rivers demonstrating a fractal nature (Tarboton et al., 1988), and the size versus the abundance of lakes can be modeled with a power-law distribution (Cael and Seekell, 2016; Downing et al., 2006). As subpixel water bodies are more difficult to map, MODIS is insufficient to capture these abundant small rivers and lakes (Klein et al., 2017; Ticehurst et al., 2014).

The European Space Agency brought a valuable new data stream with the Sentinel-2 mission. Sentinel-2A was launched in 2016 and Sentinel-2B in March 2017, and full acquisition began in April 2017. The Sentinel-2 satellites are equipped with MSI sensors that capture the visible and NIR wavelengths with 10m spatial

resolution, narrower red edge spectral bands and longer wavelengths with 20m, and atmospheric bands at 60m resolution. Additionally, with the pair, the whole globe is imaged every 5 days. This offers an unprecedented opportunity to measure the seasonality of surface water and the extent of smaller water bodies. However, the lack of a thermal sensor on the Sentinel-2 satellites makes cloud detection more difficult (Tarrío et al., 2020). Various models have made strides to overcome this, some of which are adaptations of models initially developed for Landsat (Doxani et al., 2018; Louis et al., 2016; Qiu et al., 2019; Vermote et al., 2016). In an evaluation by Tarrío et al. (2020), an ensemble approach of these methods was most effective, but there is still much room for improvement. There have been no global Sentinel-2 studies to date, however, there have been some regional time-series studies demonstrating the potential of the data for broader studies (Wieland and Martinis, 2020; Xiucheng Yang et al., 2020).

The last decade has brought huge leaps in our understanding of global inland surface water. Before this point, there was a 90m map derived from the Shuttle Radar Topography Mission (SRTM) elevation data, but this dataset only covered south of 60°N and excluded small water bodies. Several circa 2000 Landsat based maps were produced (Chen et al., 2015; Feng et al., 2016; Verpoorter et al., 2014), and Yamazaki et al. (2015) produced a map with a limited delineation of temporary and permanent water from multiple observations. These demonstrated the reach of surface water, but are all limited through the use of only the Global Land Survey collection (Gutman et al., 2008; Tucker et al., 2004), which includes one Landsat image per circa 1990, 2000, 2005, 2010, each selected from a window of up to +/- 3 years, and

for some areas of the world, there are no completely cloud-free images, leaving data gaps where there was cloud cover. Hansen et al. (2013) classified all Landsat 7 growing season images 2000-2012 but only provided a binary water and land map based on a threshold of 50% of the clear observations. Pekel et al. (2016) greatly moved forward the field in 2016 with the release of a time-series of surface water maps 1985-2015. They mapped water at a monthly scale and also aggregated it into annual layers and various summary maps, including percent water occurrence over the entire period. They mapped change in two different ways: relative increase or decrease of water percent between the two epochs of 1985-1999 and 2000-2015 (now updated to 2000-2019), and a transition map between the first representative year and 2015 (in the update 2019). This latter map is also primarily bi-temporal, with all the intervening years ignored except in the case where both the first and last year were land. In that case, the years between were checked to see if there was ever permanent or seasonal water and if so was labeled either ephemeral permanent or ephemeral seasonal based on a majority rule. If there was water in either the first or last year, the resulting transition class is the combination of the classes of those two years: permanent, new permanent (land and permanent), lost permanent (permanent and land), seasonal water, new seasonal (land and seasonal), lost seasonal (seasonal and land), seasonal to permanent, and permanent to seasonal. Thus, though Pekel et al. (2016) mapped surface water with high temporal resolution (monthly), their synthesis of change is primarily bi-temporal and while both of these maps are valuable, they ignore much of the complexity of surface water dynamics and much of what is labeled stable in the transition map may not actually be.

Due to surface water extent's high rate of variability, it is necessary to assess the entire time period of interest. With only ≤ 4 observations per pixel, Yamazaki et al. (2015) found that 13% of the total water area was temporary. With their much deeper assessment, Pekel et al. (2016) found that the area with temporary water was 46% of the total water area. While some of this corresponds to monotonic changes such as reservoir creation (Zarfl et al., 2015) or stable seasonal water, much of it is in areas with significant interannual variability. Many systems exhibit significant variability between years such as lakes in arid and semi-arid regions of the Sahel (Kaptué et al., 2013) and Australia (Mueller et al., 2016; Tulbure et al., 2016); river systems such as the Magdalena River (Restrepo and Kjerfve, 2000), Ob River (Frappart et al., 2010), and Rio Negro (Frappart et al., 2008), that also have high seasonal variability; and saturated landscapes like the Prairie Potholes of North America (Liu and Schwartz, 2012).

All of the aforementioned satellites have optical sensors. These are limited in their ability to capture the full scale of surface water due to cloud cover and its co-occurrence with short-duration floods, which is of particular importance for monsoonal regions (Pham-Duc et al., 2017), and vegetation cover over surface water such as in the forested wetlands of the Amazon basin (Hess et al., 2015). Satellites equipped with radar sensors, which actively emit long wavelength radiation and measure the return, can overcome some of these issues (DeVries et al., 2020; Hess et al., 2015; Pham-Duc et al., 2017; White et al., 2015).

1.1.4 Area estimation

According to the Intergovernmental Panel on Climate Change (IPCC) of the United Nations (Eggleston et al., 2006), it is essential for international reporting to adhere to the current guidelines of area estimation through a probability-based sample to obtain unbiased area estimators of known uncertainty as quantified by standard errors. Often maps are used directly to assess the area of a given class through summing pixel areas (Feng et al., 2016; Pekel et al., 2016; Yamazaki et al., 2015). While valuable, this leaves users without a measure of its certainty or rigor, and will carry whatever biases are present in the classification into the area totals. According to good practice guidelines, area reporting requires the use of a statistical sample of reference data (Olofsson et al., 2014). Reference data must be of higher quality than the map itself and must be selected in a statistical way. Sampling allows one to estimate the fraction of a stratum that belongs to a class, and variance can be calculated to estimate, given the proportion of a class, how likely other estimates of the same sample size would obtain the same area estimate. While sample-based area estimation has become the standard for forest monitoring (Penman et al., 2016), it is slower to take hold in other areas of land cover and land use change (LCLUC).

For estimating the area of elements of LCLUC that cover only a small fraction of the whole region of interest, maps can provide significant efficiency gains (Ying et al., 2017). In the case of inland surface water, which covers 3-4% of the continental landmass (Feng et al., 2016; Pekel et al., 2016), with simple random sampling, the mean case would only have 3-4 samples with water presence for every 100. To achieve high precision of surface water area estimation using random sampling, a

very high number of samples would be required. Stratification, on the other hand, enables an efficient targeting of the class of interest and is particularly valuable for rare classes, such as global inland surface water. Additionally, change dynamics can represent an even far smaller fraction of the landscape. For instance, Pekel et al. (2016) reported 162,000 km² of partial or complete loss, which equates to 0.1% of the land surface, making stratification all the more invaluable. In addition to being used as a stratifier, maps provide spatial information important for planning and management and for assessments of interactions with climate and land cover and land use change (UN Water, 2018; World Meteorological Organization (WMO) et al., 2016).

1.2. Dissertation research objectives and structure

This dissertation aims to advance our understanding of and capability for monitoring open inland surface water dynamics through a mixed mapping and sampling approach with a dense time-series of all Landsat 1999-2019 data and analyze the effects of temporal and spatial resolution on extent and change estimates. Here, open water is defined as water on the ground surface that (1) is visible from above and not obscured by objects on or above the water surface, for example, forest canopy, floating aquatic vegetation, bridges, clouds, or ice; and that (2) covers $\geq 50\%$ of a pixel. Figure 1.1 provides a graphical outline of the dissertation.

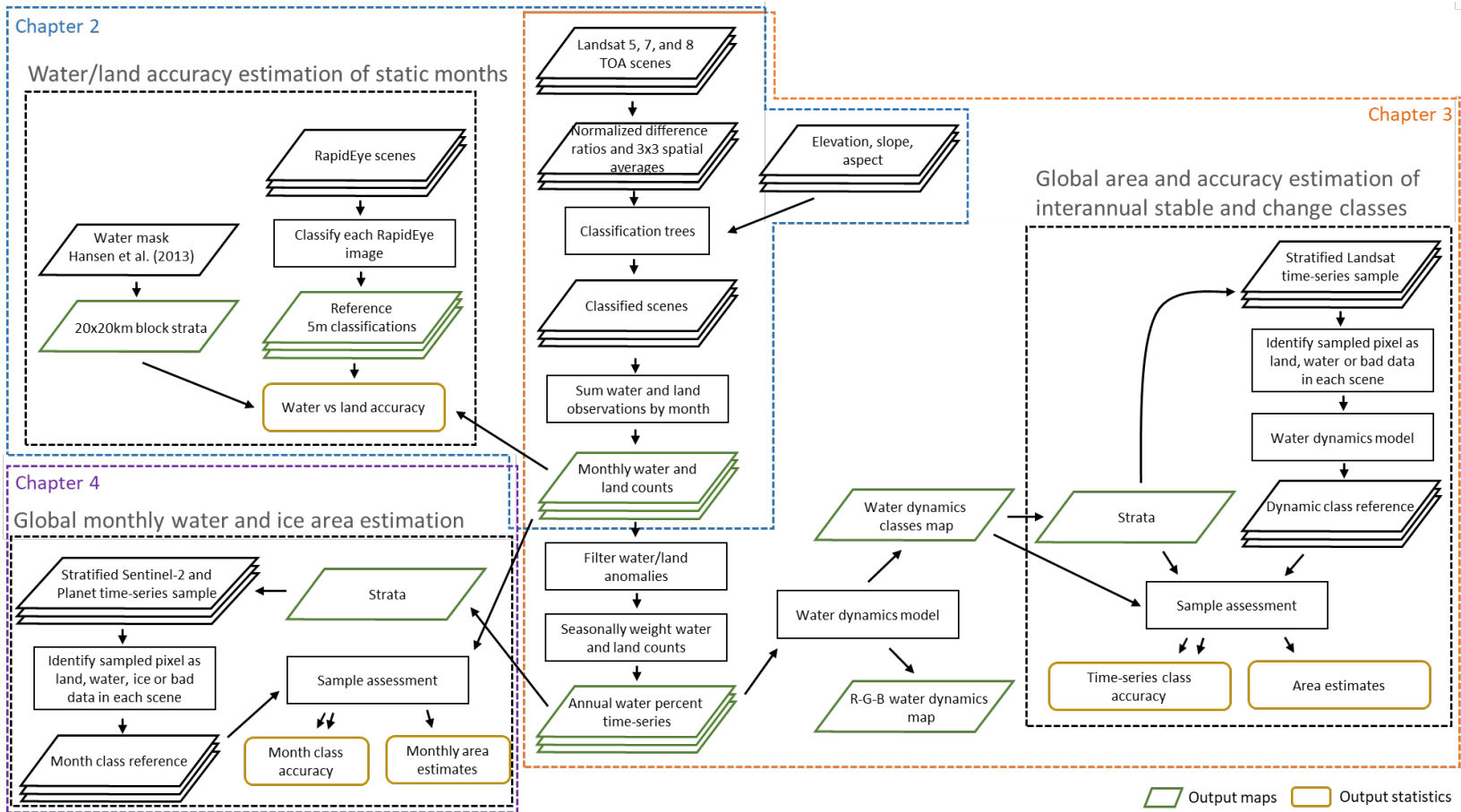


Figure 1.1: Outline of dissertation.

The first objective is to assess the current water detection algorithms using Landsat and characterize the spatial heterogeneity of surface water at 30m. The aim is to produce numerical answers with quantified uncertainty to the following questions: (1) How well can we map water using Landsat? (2) What are the spatial limitations of mapping with Landsat? Chapter 2 answers these questions using a stratified sample of 20x20km units of 5m reference data.

The second objective is to produce maps that characterize the dynamics of surface water extent using the entire Landsat time-series of 1999-2018 and to estimate the areas of permanent water, stable seasonal water, and five change dynamics with a probability sample analysis. The purpose of this is to answer these questions: (1) What is the global area of stable and dynamic surface water extent? (2) How much surface water extent has been lost, gained, fluctuates interannually, or fluctuates seasonally? (3) Globally, where are the areas of change? Chapter 3 addresses these questions through classifying all of the 1999-2018 Landsat archive, mapping stable and change dynamics of surface water globally, and estimating areas through a probability-based sample assessment.

The third objective is to advance our knowledge of seasonal dynamics by employing the 10m data with ≤ 5 day revisit of Sentinel-2 to answer: (1) What is the monthly distribution of inland open surface water and inland surface water ice? (2) What portion of global inland surface water freezes? (3) What is the ability of Landsat and Sentinel-2 to capture these dynamics? To address these, in Chapter 4 a global sample was selected and all 2019 Sentinel-2 images together with 3m imagery of PlanetScope was labeled for the selected pixels, and the monthly area of open

inland water and surface water ice were estimated with associated uncertainties.

Landsat based maps of surface water ice were developed and validated together with the 2019 maps of surface water from Chapter 3.

The final chapter of this dissertation highlights the main advances of this body of research, evaluates its strengths and limitations, and discusses important areas of future research.

Chapter 2: Ensemble approach for Landsat water detection with sub-pixel evaluation¹

Abstract

Many methods have been utilized to map water ranging from simple thresholds to more complex machine learning algorithms. Due to the variation in the reflectance properties of surface water due to factors such as sediment load or chlorophyll-*a* concentrations, information from multiple reflectance bands and indices is valuable. Here we present a classification tree ensemble approach to identify water, land, cloud, haze, shadow, and snow/ice. Using a stratified sample of 20x20km blocks with water presence classified from 5m RapidEye imagery, we performed a subpixel assessment of our proposed method as well as the most broadly applied algorithm, that of Pekel et al. (2016). We found user's and producer's accuracies of 93.7 (± 1.5)% and 96.0 (± 1.2)%, respectively. Evaluating accuracy as a function of distance, have a user's accuracy of 96.9 (± 0.9)% and a producer's accuracy of 99.0 (± 0.3)% for all pixels >30 m from the closest edge of a water body, and 70.9 (± 1.6)% and 66.0 (± 3.7)%, respectively, for all pixels <30 m from a water body edge. Results were similar for Pekel et al. (2016), but with a greater bias of omission particularly for mixed pixels. From this same probability sample of high resolution imagery, an estimated 10.9% (± 1.9)% of global inland surface water is

¹ The contents of this chapter have been published in: Pickens, A.H., Hansen, M.C., Hancher, M., Stehman, S.V., Tyukavina, A., Potapov, P., Marroquin, B., Sherani, Z., 2020. Mapping and sampling to characterize global inland water dynamics from 1999 to 2018 with full Landsat time-series. Remote Sensing of Environment 243, 111792. <https://doi.org/10.1016/j.rse.2020.111792>

within mixed pixels at Landsat resolution indicating significant benefits to monitoring of surface water changes with improved spatial detail.

2.1. Introduction

Since the advent of earth observation satellites, there has been a preponderance of methods to detect surface water. Surface water is darker than most other land covers, reflecting some light in the visible spectrum but absorbing almost all of the longer wavelengths (Martin, 2004; Pope and Fry, 1997; Smith and Baker, 1981). McFeeters (1996) found that the normalized difference ratio between green and near-infrared (NIR) was particularly effective for identifying water presence and designated it the Normalized Difference Water Index (NDWI). Other indices have been developed to address specific contexts such the normalized difference ratio between green and short water infrared (1.55 to 1.75 μm), termed the Modified Normalized Difference Water Index, which was developed to better distinguish between open surface water and built-up environments (Xu, 2006). These indices have been widely used in studies around the globe (Huang et al., 2018). However, water can have a diversity of spectral properties based on variation within the water column and surface roughness (Boland, 1976; Han et al., 1994; Han and Rundquist, 1994; Martin, 2004). Additionally, some land covers share reflectance properties of the various manifestations of surface water hindering single thresholds (Fisher et al., 2016). For these reasons, combinations of bands and indices have been used in more complex machine learning algorithms to capture water through the span of its representations (Tulbure et al., 2016).

However, most of these methods have been developed for local or regional contexts and have not been employed or tested globally. Pekel et al. (2016) have released the first global maps of surface water with a dense time-series of observations from the 1984-2015 Landsat archive. Their water detection algorithm was created by iteratively selecting portions of the feature space as surface water. Here we present a new globally-applicable water and land detection algorithm that is derived in a data-driven, machine learning approach from a large volume of training data. We employ a probability-based sample of high resolution (5m) data to evaluate the global performance of both this new algorithm and that of Pekel et al. (2016) across arid and water-saturated environments.

2.2 Methods

2.2.1 Scene classification

A time-series of open water presence was created through the automated implementation of per Landsat sensor ensembles of classification trees. For each sensor, classification tree models of observation quality and land or water state (Potapov et al., 2015) were developed in the Global Land Analysis and Discovery (GLAD) laboratory. These models were then implemented in Google Earth Engine (Gorelick et al., 2017) and applied to the entire 1999-2018 Landsat 5, 7, and 8 archive, classifying each scene into land, water, cloud, shadow, haze, and snow and ice. In each scene we aim to map as water all pixels with $\geq 50\%$ water cover according to the definition of open surface water given above.

Due to the diversity of reflectance patterns for open surface water targets, hierarchical, bagged classification trees (Breiman, 1996; Breiman et al., 1984) were used to discriminate clear observations from those contaminated by cloud, shadow, and ice and discriminate water from land. All images were first converted to top of atmosphere (TOA) reflectance (Chander et al., 2009). Water is sufficiently separable from land to employ TOA units in discrimination without conversion to surface reflectance or application of other normalization methods (Pekel et al., 2016; Tulbure et al., 2016; Yamazaki et al., 2015). The classification models utilize all the Landsat bands, normalized difference ratios of each pair of spectral bands, and 3x3 pixel spatial averages of all bands and ratios, as well as, utilize topographic inputs of elevation and derived slope, aspect, and hillshade data. There are 21 normalized difference ratios for Landsat 5 and 7 and 36 for Landsat 8 due to three additional spectral bands. These ratios include commonly applied water indices such as the Normalized Difference Water Index (NDWI, $(\text{Green}-\text{NIR})/(\text{Green}+\text{NIR})$) (McFeeters, 1996) and the Modified Normalized Difference Water Index (MNDWI, $(\text{Green}-\text{SWIR1})/(\text{Green}+\text{SWIR1})$) (Xu, 2006). Elevation was taken from Shuttle Radar Topography Mission (SRTM) (Jarvis et al., 2008) elevation data for areas south of 60°N, and Global Multi-resolution Terrain Elevation Data 2010 (Danielson and Gesch, 2011) for areas north of 60°N.

Five sets of seven bagged classification trees were built hierarchically for each sensor from a training set of fully classified scenes. These scenes were individually classified through manual training and using the same classification tree framework as the globally applied model. The sets of classified scenes were used to train the

global models, for example 165 Landsat 5 scenes were mapped with the six categories of water, land, cloud, shadow, and snow/ice and used in training a global Landsat 5 water model. The global models were iterated by testing images not included in the training, identifying errors and adding problematic scenes to the training set and adjusting sampling rates until results were deemed satisfactory at the global scale. The final number of scenes in the training set was 165, 164, and 120 per Landsat 5, 7, and 8, respectively, and these scenes were sampled with a rate of 0.5-1.5% depending on the class and the set, resulting in over a billion pixels used as training for the global models.

The first set of seven bagged classification trees separates cloud and snow and ice from haze, land, shadow and water; the second set separates water from haze, land, and shadow; the third set separates shadow from haze and land; and the fourth set separates haze from land; and the final set separates cloud from snow and ice. Thus, clear water observations are identified after the first two sets and clear land observations after four sets. The set of seven trees per sensor that discriminated water from clear land, shadow, and haze relied strongly on the normalized difference ratio of the near infrared and green bands (NDWI), accounting for 89%, 85%, and 81% of deviance decrease for the Landsat 5, 7 and 8 models respectively. For this set of trees separating water, all of the 3x3 pixel spatial average metrics accounted for 4.9%, 6.7%, and 7.9% of the total deviance decrease, but for the first set of trees identifying cloud, snow, and ice the 3x3 metrics contributed 86.5%, 82.9%, and 74.4%, which is likely due to the diffuse nature of clouds. However, all of the Landsat and topographic inputs contributed to discriminating water, land, and bad data. The

models are thus complex, with 50-1000 nodes per tree. However, overfitting is avoided by using a large training sample and aggregating each set of trees by selecting the median output probability. This enables the identification of open surface water across many different states, from sediment-laden to clear to eutrophic and from shallow to deep; water with the surface obscured from above by vegetation or other obstructions such as bridges is excluded.

2.2.2 Sample-based assessment

To quantify accuracy for mapping water at a given instance at a subpixel scale, we used a stratified sample of 5m resolution reference imagery from RapidEye. This sample was used to estimate accuracy of water and land classifications only at the individual month time scale and was not suitable for evaluating change. To create strata, we divided the global land surface into 20x20km blocks and calculated the percent water cover in each block based on the water mask created by Hansen et al. (2013) that they termed “datamask” within their global forest change product (Figure 2.1). This mask represents all pixels with water detection percent $\geq 50\%$ for all clear growing-season observations of 2000-2012 from Landsat 7. Blocks that had no water pixels, no pixels with $>0\%$ tree cover, and all pixels with $\geq 95\%$ bare ground were defined as desert blocks and excluded from the sampling frame (gray areas, Figure 2.1). Blocks that were entirely water in all the observations, found exclusively in very large lakes and seas, were also excluded. The remaining 307,195 eligible blocks were divided into four near equal size strata corresponding to block water cover of 0%, 0-0.08%, 0.08%-2%, and $>2\%$ (Figure 2.1).

Thirty-five blocks were randomly selected per stratum, and a 5m multispectral image was obtained from RapidEye for each block. Since we mapped each RapidEye image individually, no radiometric correction was necessary, other than to manually remove cloud or other artifacts from the image. However, RapidEye images were mis-registered by up to 40m when using reported ephemeris data. To overcome this issue, we implemented a post-processing step of shifting the RapidEye classifications to the x-y offset that yielded the greatest water overlap with the water mask of Hansen et al. (2013).

All sample RapidEye images were from 2010-2013 growing seasons based on availability, and each sample image was compared against the monthly percent water layer from this current study corresponding to the month in which the image was taken. This time range allowed for data from Landsat 5, 7, and 8 to all be represented. The RapidEye single date images and monthly aggregate map products were not coincident given the varying acquisition rates of Landsat and RapidEye data. However, the majority of surface water is stable at monthly time scales and, in general, any non-matching data will lower the accuracy estimates rather than inflate them. Some blocks for which the RapidEye data could not be obtained or that had over 25% cloud cover were replaced by selecting the next eligible block from a randomly ordered list of sample blocks up to 15 blocks. Some blocks did not have any Landsat data from the corresponding month and were excluded. The final sample sizes were 28, 33, 29, and 26 for the very low, low, medium, and high water cover strata, respectively, due to missing data.

Each RapidEye image was individually trained and classified through an iterative process of delineating water and land training polygons and then running an image-specific set of seven bagged classification trees to classify the entire sample block. The classification trees were built on the five spectral bands in RapidEye imagery and clouds and shadows were manually masked. For many blocks, we iterated and added training polygons numerous times to obtain high quality maps at 5m. These maps are suitable as reference data as the higher spatial resolution enables a more discrete mapping of surface water that is readily identifiable through a supervised mapping approach (Olofsson et al., 2014). The result is an independent and better characterization of water extent for the respective date than the corresponding Landsat map made using a global algorithm.

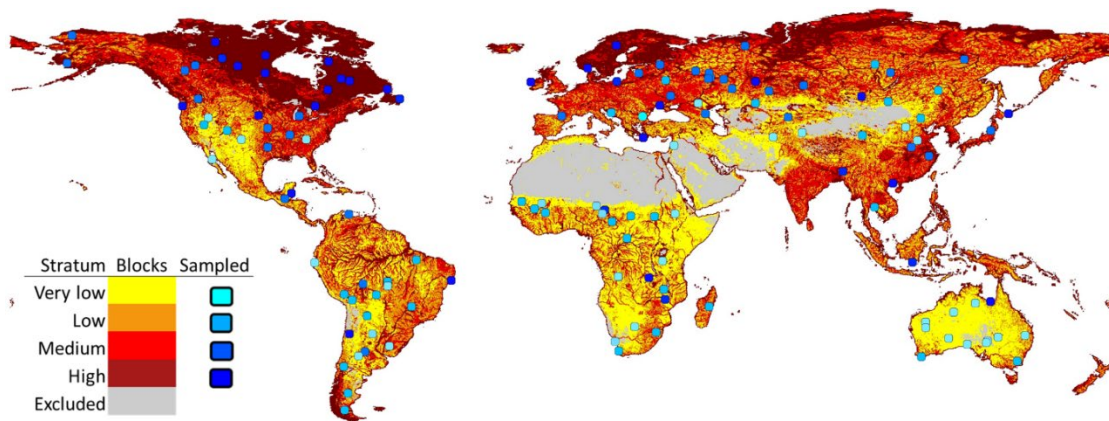


Figure 2.1: Distribution of strata and sampled blocks for 5m assessment. The thresholds of the percent of block area covered by surface water for the very low, low, medium, and high strata are 0%, 0-0.08%, 0.08%-2%, and >2%.

The resulting 5m discrete map of water, land, and no data was the reference set compared against the Landsat monthly percent water layers to obtain user's (corresponding to commission) and producer's (corresponding to omission)

accuracies at 5m and 30m resolutions. For this analysis, the Landsat monthly percent water was thresholded so that all pixels above 50% were labeled as water and all pixels below 50% were labeled as land, as the dominant state of land or water was more likely to match the surface conditions of when the RapidEye scene was imaged. Pixels with equal land and water observations were excluded to prevent introducing a bias, since there is no dominant state.

To estimate user's accuracy of the monthly mapped water class we used a ratio estimator (Stehman, 2013):

$$\hat{R} = \frac{\sum_{h=1}^H Y_h}{\sum_{h=1}^H X_h} \quad (1)$$

where H is the number of strata, Y_h is the total area of intersection between the Landsat monthly map of water and the reference classification from all sampled blocks of stratum h with the area from block i denoted y_i , X_h is the total area of mapped water within the Landsat map from all sampled blocks of stratum h with the area from block i denoted x_i , and \hat{R} is the estimator for user's accuracy. For producer's accuracy we used the same formula keeping the same definition for Y_h and y_i but now defining X_h to be the total area classified as water in the reference data from all sampled blocks of stratum h and x_i the area of this region in block i . The estimated variance of the ratio estimator is:

$$\hat{V}(\hat{R}) = \frac{1}{\hat{X}^2} \sum_{h=1}^H N_h^2 \left(1 - \frac{n_h}{N_h}\right) (s_{yh}^2 + \hat{R}^2 s_{xh}^2 - 2\hat{R} s_{xyh}) / n_h \quad (2)$$

where s_{yh}^2 and s_{xh}^2 are the sample variances of y and x in stratum h , $s_{xyh} = (\sum_{i=1}^{n_h} (x_i - \bar{x}_h)(y_i - \bar{y}_h)) / (n_h - 1)$ is the sample covariance between x and y in stratum h , n_h is the sample size in stratum h , N_h is the total number of blocks in

stratum h , and $\hat{X} = \sum_{h=1}^H N_h \bar{x}_h$. The standard error (SE) of the estimated accuracy is equal to the square root of the variance. The discrete 5m reference layers were also upscaled to continuous 30m maps of water with each 30m pixel representing the percent of 5m pixels within it that were labeled water. These new maps were also thresholded at 50% to create the 30m resolution, binary classified (land and water) reference set and we applied the ratio estimator to obtain user's and producer's accuracies of the monthly Landsat maps at 30m.

To assess the spatial heterogeneity of surface water, we used the continuous 30m reference data compute the percent of pixels, excluding pure land pixels, that were mixed, defined as having both water and land pixels at 5m. To explore the impact of these mixed pixels on the accuracy results as well as to determine the relationship between errors and the proximity to a land-water boundary, we calculated the distance to the nearest land-water boundary delineated in the 5m RapidEye classification (Figure 2.2). Distances were calculated in meters for every 5m pixel within each sample block with each 5m water pixel assigned the distance to the closest land pixel and each 5m land pixel assigned the distance to the closest water pixel. The distances were binned in 5m intervals and commission and omission rates were computed per bin using the ratio estimator (equation 1). For commission, y_i is defined as the area classified as water in the monthly map and land in the reference data within the given distance bin and x_i as the reference land area within the distance bin from the water-land boundary. For omission, y_i is defined as the area classified as land in the monthly map and water in the reference data within the given distance bin and x_i as the reference water area within the distance bin from the water-land

boundary. User's and producer's accuracies were also computed for the whole region within 30m of a land-water boundary which represents the potential mixed pixel region at Landsat scale and for the whole region beyond 30m from land-water boundary which represents the pure land or pure water pixel space at Landsat resolution. The spatial heterogeneity of surface water was further explored by estimating the percent of global inland water that is within mixed pixels at Landsat resolution. We used the ratio estimator (equations 1 and 2) with y_i representing the area of water within mixed pixels in block i and x_i representing the total area of water in block i .

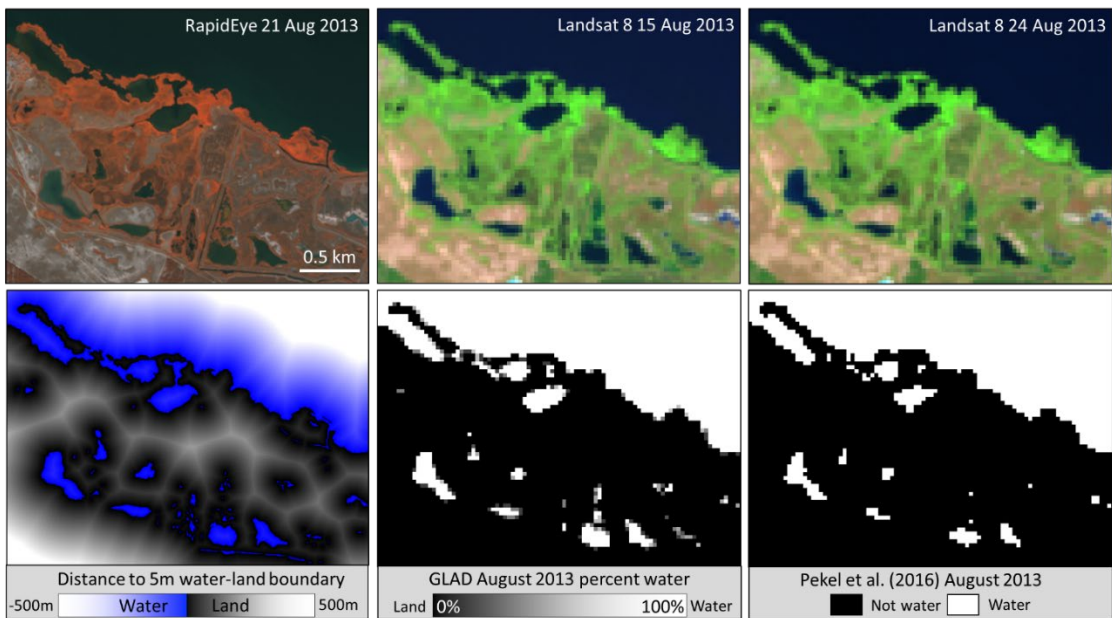


Figure 2.2: Zoom within a sample block in the high water stratum. Top-left: RapidEye data (NIR-Red Edge-Red) from August 21, 2013. Top-middle: Landsat data (SWIR1-NIR-Red) from August 15, 2013. Top-right: Landsat data (SWIR1-NIR-Red) from August 24, 2013. Bottom-left: 5m RapidEye classification of water and land with the distance to the closest water-land boundary, the blue gradients are classified as water and the gray gradients are classified as land. Bottom-middle: GLAD percent water for August 2013. Bottom-right: Pekel et al. (2016) not water and water classification for August 2013. Image centered at 46.52°N, 31.84°E on the Ukrainian coast of the Black Sea.

2.3 Results

The user's and producer's accuracies (corresponding to commission and omission rates) at 30m resolution of the monthly mapped water class defined by a threshold of 50% applied to the percent water are 93.7 (± 1.5)% and 96.0 (± 1.2)% respectively. The accuracies of the monthly mapped water class of Pekel et al. (2016) are 95.2 (± 1.2)% and 90.3 (± 2.3)% using the same reference sample data. All of the accuracies presented in this subsection refer to these water classes for different resolutions and regions. At 5m resolution, the user's and producer's accuracies in our study are 97.5 (± 0.7)% and 97.7 (± 0.7)% and Pekel et al.'s are 98.0 (± 0.5)% and 95.1 (± 1.3)%. These numbers are heavily impacted by the region that is within 30m of the water body edge, both within the water body and in adjacent land, as can be seen when the water class commission and omission rates are plotted as a function of distance away from the land-water boundary as delineated in the 5m reference data (Figure 2.3). At a distance greater than 30m, the mapped water class of our study has a user's accuracy of 96.9 (± 0.9)% and a producer's accuracy of 99.0 (± 0.3)%, and the mapped water class of Pekel et al. (2016) has user's and producer's accuracies of 99.4 (± 0.2)% and 99.5 (± 0.1)%. For the area 0-30m from the closest land-water boundary, our study's user's and producer's accuracies are 70.9 (± 1.6)% and 66.0 (± 3.7)% and Pekel et al.'s user's and producer's accuracies are 75.4 (± 2.0)% and 51.6 (± 3.3)%. Thus both datasets map water with high accuracy beyond 30m from shore lines and river banks, but both have difficulty distinguishing land and water when they are blurred together in mixed pixels. However, considering only the edge and mixed pixels, our map has less bias and correctly identifies as water 28% more of the 5x5m

footprints with water cover, and for this region within 30m of the land-water boundary two thirds of 5m space is correctly assigned. These contrasting commission and omission rates of the static water classification associated with mixed pixels carry over to the following change detection accuracy results because of the large area of mixed pixels. We found that 10.9 (± 1.9)% of global inland water is within mixed pixels at Landsat resolution, defined as having both land and water at 5m resolution within the pixel. The most common sources of commission error aside from mixed pixels are over lava flows, urban centers with tall buildings and shadowed streets, glaciers (particularly when mixed with debris), and cloud shadow over dark, dense forests with persistent cloud cover such as in Gabon.

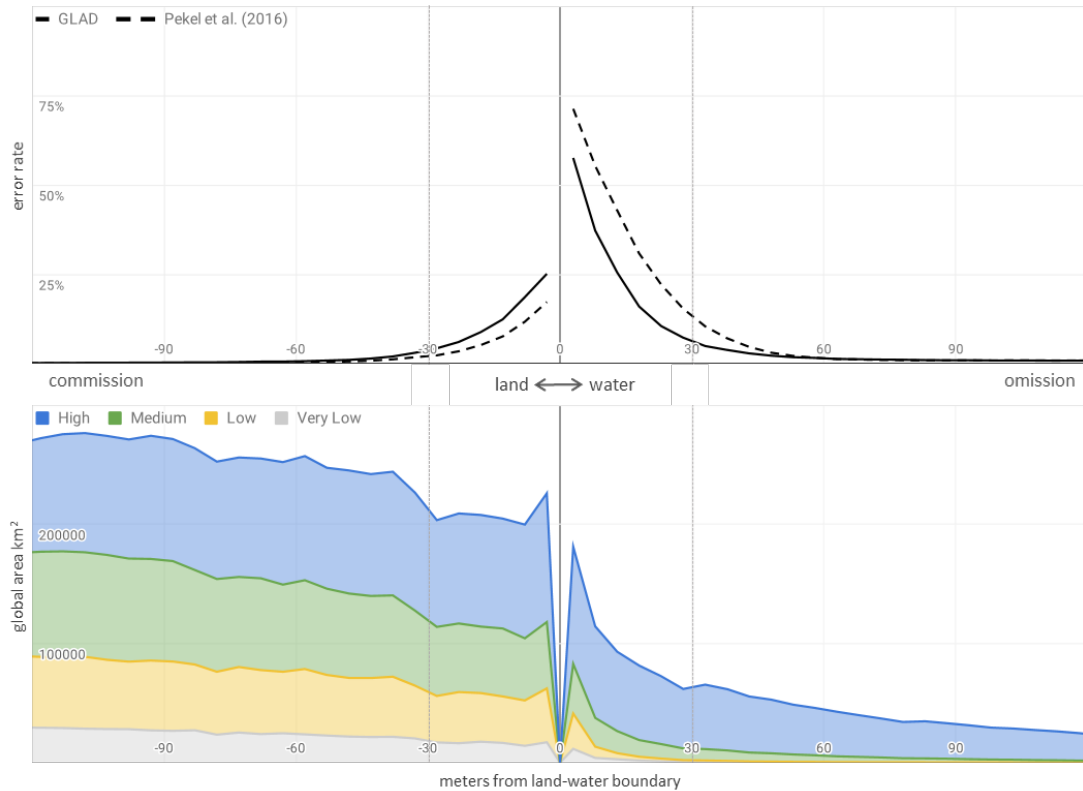


Figure 2.3: Error rates at 5m resolution of the monthly Landsat water detection as a function of distance from the land-water boundary as defined in the 5m reference data. Top: The left half of the figure has distances extending further into land and displays commission error rates of water for both this study and Pekel et al. (2016) and the right half has distances extending further into water bodies and displays omission error rates of water. Each vertical line represents 30m from the land-water boundary. The space within 30m on either side of the land-water boundary represents the mixed pixel space at Landsat resolution. Bottom: The area within each stratum at the given distance from the land-water boundary. The area of water that the low and the very low water strata contribute drops off very quickly due to small water body size. There is no area at 0m because this is the boundary line between land and water.

2.4 Discussion

The validation employing 5m RapidEye data shows that the classification algorithm performed well in discriminating pure land from pure water pixels. Example error sources included ice cover, lava, dark vegetation cover, high turbidity or very shallow water, issues of timing, and, more frequently, the combination of

shadow or haze with one of these covers, as well as, mixed pixels. To investigate the impact of mixed pixels, we assessed accuracy as a function of distance from the class transition. We found that water greater than 30m from the edge of the water body (i.e. the width of a Landsat pixel) had very high accuracy in both the maps produced in our study and in the study by Pekel et al. (2016). However, we must be concerned about the classification accuracy of mixed pixels given that 10.9 (± 1.9)% of inland water area is within mixed pixels. In this study, we achieved user's and producer's accuracies of the water class in the mixed pixel region of 0-30m from the water-land boundary of 70.9 (± 1.6)% and 66.0 (± 3.7)% for the single month layers at a scale of 5m. While theoretically a 30m map could have 100% accuracy at 30m, it could never have 100% accuracy at 5m. Thus, though mixed pixels have much lower accuracies, we correctly map two thirds of the 5m space within 30m of the land-water boundary. Furthermore, in our study we correctly identified 28% more of the 5x5m footprints with water cover compared to the only previous dense surface water record at 30m (Pekel et al. 2016). This increased accuracy translates to better quantification and monitoring of small water bodies.

2.5 Conclusion

Given that 10.9 (± 1.9)% of global water is mixed with land at a 30m resolution and that many change dynamics occur within mixed pixels, there is a clear need for improving spatial detail in tracking surface water changes. Fortunately, newer high spatial resolution data from the Sentinel-1 and Sentinel-2 series of satellites offer a ready input for advancing open surface water monitoring. Planet

data, while likely not a feasible alternative for global mapping due to its high cost, may be used as reference data in assessing map accuracies and providing area estimates for various dynamics. In addition to higher spatial resolution, incorporating Sentinel-1 and Sentinel-2 together with Landsat will provide higher temporal resolution, enabling better characterization of ephemeral surface water.

Chapter 3: Mapping and sampling to characterize global inland water dynamics from 1999 to 2018 with full Landsat time-series²

Abstract

Global surface water extent is changing due to natural processes as well as anthropogenic drivers such as reservoir construction and conversion of wetlands to agriculture. However, the extent and change of global inland surface water are not well quantified. To address this, we classified land and water in all 3.4 million Landsat 5, 7, and 8 scenes from 1999-2018 and performed a time-series analysis to produce maps that characterize inter-annual and intra-annual open surface water dynamics. We also used a probability sample and reference time-series classification of land and water for 1999-2018 to provide unbiased estimators of area of stable and dynamic surface water extent and to assess the accuracy of the surface water maps. From the reference sample data, we estimate that permanent surface water covers 2.93 (standard error ± 0.09) million km², and during this time period an estimated 138,011 ($\pm 28,163$) km² underwent only gain of surface water, over double the estimated 53,154 ($\pm 10,883$) km² that underwent only loss of surface water. The estimated area of 950,719 ($\pm 104,034$) km² that experienced recurring change between land and water states is far greater than the area undergoing these unidirectional trends. We provide the first unbiased area estimators of open surface water extent and

² The contents of this chapter have been published in: Pickens, A.H., Hansen, M.C., Hancher, M., Stehman, S.V., Tyukavina, A., Potapov, P., Marroquin, B., Sherani, Z., 2020. Mapping and sampling to characterize global inland water dynamics from 1999 to 2018 with full Landsat time-series. *Remote Sensing of Environment* 243, 111792. <https://doi.org/10.1016/j.rse.2020.111792>

its changes with associated uncertainties and illustrate the challenges of tracking changes in surface water area using medium spatial and temporal resolution data.

3.1 Introduction

Surface water presence is highly variable, with diverse trends around the world reflecting direct and indirect human as well as natural drivers. Meandering natural rivers and their floodplains support high biodiversity and provide nutrient-rich soil for agriculture, but are increasingly rare (Tockner and Stanford, 2002). Extensive areas of floodplains and natural wetlands have been engineered for food production, for example to rice and aquaculture (Davidson, 2014; Tessler et al., 2016; Zhao et al., 2008). Globally almost half of our river systems are moderately to severely fragmented by dams, levees, and other structures, affecting both ecosystems and economies (Grill et al., 2015). Climate change and diversion of rivers for irrigated agriculture have led to dramatic declines in the surface area of large saline lakes (Wurtsbaugh et al., 2017). Climatic changes are also intensifying rates of glacier melt, causing the lakes of the Tibetan plateau to expand and river discharge patterns to shift (Chevallier et al., 2011; Lutz et al., 2014).

Improved quantification of historical surface water trends will help us to better understand the impacts of such changes and to protect water resource-related ecosystem services. Historical archives of data from earth observation satellites are the only viable means to quantify these dynamics at a global scale and through time. Various efforts have advanced our understanding of historical surface water trends. Pekel et al. (2016) is the most comprehensive surface water product to date with 30m

monthly water/non-water layers, annual maps of seasonal and year-round water, and various multi-temporal maps initially for the period of March 1984-October 2015. In mid-2019, Pekel et al. (2016) released an update extending the mapped period through December 2018, which is available through the original sources. The water mask produced by Hansen et al. (2013) represents persistent water over 2000-2012, with all pixels having water in $\geq 50\%$ of all growing season Landsat 7 observations. Other global maps at 30-90m (Chen et al., 2015; Feng et al., 2016; Yamazaki et al., 2015) have been produced but for isolated years and based on one or a few Landsat scenes per path-row as found in the Global Land Survey collection (Gutman et al., 2008; Tucker et al., 2004). Other products have evaluated intra-annual and inter-annual surface water dynamics but at subnational or national scale (Mueller et al., 2016; Tulbure et al., 2016; Zou et al., 2018). However, the existing global maps that identify change are only based on two time periods. Change in Pekel et al. (2016) was defined in two different ways. In one map, change was defined as the difference in open water occurrence percent between 1984-1999 and 2000-2018. In the second map, change was defined as the transition between permanent water, seasonal water, and land between a first year and the last year, 2018. The first year was selected between 1984 and 2000 on a per-pixel basis as the first year which had sufficient observations through the year to characterize the water presence. All intervening years were ignored for pixels in which water was identified in one or both of the start and end years (Pekel et al. 2016). Due to the large extent of fluctuations between water and land both seasonally and inter-annually (Papa et al., 2010; Pekel et al.,

2016; Prigent et al., 2012; Yamazaki et al., 2015), it is necessary to evaluate the entire time-series to accurately assess surface water dynamics.

Previous quantifications of global water area have been based on “pixel counting” of the map (i.e., summing the area of pixels mapped as the target class). In contrast, current good practice guidelines recommend estimating area based on a probability sample of reference data (Eggleston et al., 2006; Olofsson et al., 2014; Penman et al., 2016). Because the reference class labels determined for the sample units have greater accuracy than the map classification, the area estimate based on the reference class labels is less subject to bias due to class labeling error. This greater accuracy of the reference class labels is achieved by using higher quality source data, such as by interpreting higher resolution imagery, or if using the same source data, by implementing an intensive interpretation effort to determine the reference class labels for the relatively small number of sample units (Olofsson et al., 2014). The variability of a sample-based area estimate is measured by the standard error, whereas, there is no measure of uncertainty associated with area derived from pixel counting.

According to the Intergovernmental Panel on Climate Change (IPCC) of the United Nations (Eggleston et al., 2006), it is essential for international reporting to follow these guidelines in order to obtain unbiased area estimators of known uncertainty as quantified by standard errors. Good practice methods provide definitive information on area extent and change that can inform science applications and policy initiatives.

We present a new map characterization of permanent open surface water and of various open surface water change dynamics from 1999-2018 based on the entire Landsat archive for this period, consisting of 3.4 million scenes. Using a probability

sample of reference data, we assess the accuracy of our global surface water maps for the 1999-2018 interval as well as the accuracy of the maps produced by Pekel et al. (2016). We also use these reference data from the probability sample to provide unbiased estimators of area of global open surface water extent and change. We define open surface water as water on the ground surface that (1) is visible from above and not obscured by objects on or above the water surface, for example, forest, floating aquatic vegetation, bridges, clouds, or ice and that (2) covers $\geq 50\%$ of a 30m pixel.

Here we analyze a more temporally dense time series than previous studies for both change maps and reference data, employing the full Landsat archive in improving the characterization of the dynamics of global open surface water extent. We employ the first probability-based sample that targets changes in global surface water extent, providing area estimates of dynamics derived from unbiased estimators. The results are less susceptible to the bias encountered when reporting change from pixel counts. The associated standard errors from the reference samples are an improvement over map product areas that lack measures of statistical uncertainty. Our accuracy assessment is another advance, covering the entire time-series of our map products as well as the entire global land surface, making it spatially and temporally comprehensive. Further, the accuracy assessment corroborates the quality of the maps of Pekel et al. (2016) based on a more complete reference sample data set than was used by Pekel et al. (2016) in their evaluation of their map.

3.2 Methods

The ensemble of classification trees evaluated in Chapter 2 were applied to all 3.4 million Landsat 5, 7, and 8 scenes from 1999 to 2018, totaling 2.4 petabytes of data. The resulting time-series of land and water observations are the input to our characterization of surface water dynamics.

3.2.1 Creation of annual percent water time-series

The land and water observations of a given pixel were summed per month and aggregated into water presence frequency at various time-scales, measured by the percent of clear observations flagged as water ($\text{water} / (\text{water} + \text{land})$), hereafter referred to as water percent. To create a more representative and stable measure of water percent, the individual observations were filtered and weighted, a practice also implemented by Pekel et al. (2016). First, clear observations ($\text{water} + \text{land}$) over the full study period were examined and if less than 12.5% of observations were in an opposite state of water or land (not covered with clouds, shadows, haze, snow or ice), and the total number of these observations was ≤ 3 , they were removed as outliers. This was done because cloud shadow over dense tree cover or other dark surfaces can erroneously be flagged as water, and image artifacts or undetected haze over water can sometimes be erroneously flagged as land. However the probability of these errors repeatedly happening over the same pixel is low, and we found that these thresholds removed considerable noise while not erasing real change.

We created a seasonally-normalized annual water percent to account for intra-annual variation in clear observation frequency (e.g. fewer observations in the far

north in winter due to low sun elevations or in tropical monsoon environments due to high cloud cover). The water and land observations were summed per meteorological seasons (December-February, March-May, June-August, September-November) of each year, and used to calculate the percent of water observations out of all clear observations per season. Months with less than 5 observations over the 20 years were excluded to remove a potentially irregular impact on the annual time-series due to different portions of the year being observed. The average of the four seasons with data was used to calculate percent of water per year. Given that the start day of hydrological years varies around the world, we selected a start day that corresponded with the meteorological seasons and that mostly closely aligned with a traditional calendar year. A year was thus defined as December 1 of the previous year through November 30 of the given year (e.g. 2003 was defined as December 2002-November 2003). Seasonal weighting was done to account for varying number of clear observations during different seasons of the year due to seasonal prevalence of weather events which often both obscure the surface and cause more surface water, seasonal snow cover, and varying acquisition rates related to sun angle for regions at high latitudes.

3.2.2 Dynamic type classification

An inter-annual water dynamics model was developed to characterize and visualize the changes occurring over the study period (Figure 3.1). To reduce short-term annual anomalies and inter-annual cloud-free observation variability, the annual open water percent time-series was smoothed using a 3-year mean moving window. Next, the range and mean of the annual percent water time-series data were calculated

per pixel. The range is representative of the difference between the maximum rate and the minimum rate of open water presence. Pixels with a range $\leq 33\%$ and a mean $\leq 10\%$ or $\geq 90\%$ were labeled permanent land and water, respectively, providing a stable target with low sensitivity to possible omission or commission effects due to image artifacts or atmospheric conditions. Change pixels were identified as pixels with a range $\geq 50\%$, and all other pixels labeled as stable seasonal, characterized by water presence having little or no inter-annual variation and consistent intra-annual variation. Further characterization was applied to pixels labelled as change to identify typologies defined by an analysis of all local maxima and minima in the time-series. These local extrema were used to segment the 17-year time-series; segments with an amplitude $< 30\%$ of the overall time-series amplitude were removed. Remaining dominant change segments were used to characterize the following main change types: gain, loss, dry period (water-land-water), wet period (land-water-land), and high frequency (3 or more) land-water transitions. All of these change types were mapped and validated along with the stable seasonal, permanent land, and permanent water classes. If a pixel had less than 10 years with observations or less than 15 total observations and did not meet the criteria for permanent water or land, it was marked as sparse-data.

Out of all clear water and land observations, if either water or land is flagged ≤ 3 times and in only $\leq 12.5\%$ of the observations, these instances are removed.								Data operations
Seasonally weight to create annual water percent time series								
3 year mean moving window								
Calculate range (interannual variability) of annual water percent								
Interannual variability $< 50\%$				Interannual variability $\geq 50\%$				Data thresholds
Calculate mean of annual percent water				Count change segments in alternating directions between local maxima and minima of annual percent water with amplitude $\geq 30\%$				
Mean $\leq 10\%$ water, Interannual variability $< 33\%$	Mean $\geq 90\%$ water, Interannual variability $< 33\%$	10% $<$ Mean $<$ 90% AND/OR Interannual variability $\geq 33\%$		1 transition		2 transitions		≥ 3 transitions
<i>Land</i>	<i>Permanent water</i>	<i>Stable seasonal</i>		Decreasing	Increasing	Decreasing then increasing	Increasing then decreasing	<i>High frequency</i>
				<i>Loss</i>	<i>Gain</i>	<i>Dry period</i>	<i>Wet period</i>	
				Monotonic		Multiple transitions		Class aggregations
Stable				All change types				
Permanent		All dynamic types						

Figure 3.1: Workflow of time-series analysis starting with the monthly water and land counts and resulting in dynamic class labels.

3.2.3 *Dynamic class mapping*

To visualize all of the classes in a continuum we reduced the time-series to three time-sequential values of water percent mapped in an R-G-B color space (Figure 3.2). Specifically, the aforementioned classification rules were refined to characterize the timing of monotonic changes and the intensity of all change types. For pixels with monotonic loss or gain of water, the red band value was taken from the maximum or minimum water percent, respectively, at the beginning of the period. The blue band value was taken from the minimum or maximum water percent, respectively, at the end of the period. The green band value was the mean of the entire period, which enabled a graphical representation of whether the change was comparatively early or late in the study period. For pixels with two changes, there was either a change from water to land to water (a dry period), or a change from land to water to land (a wet period). For pixels with a dry period, there was a local maximum, followed by the minimum, and then by a local maximum which were assigned time-sequentially to the R-G-B space. The minimum was assigned to the green band and the two maxima were assigned to the red and blue bands with the lesser maximum averaged with the beginning or end value of the time-series depending on whether it was before or after the minimum. For example, a pond that had year-round water that dried up for a few years and then filled up but only for half the year would be represented in R-G-B space by its initial maximum value of 100% (r), its minimum value of 0% (g), and its final seasonal value of 50% (b). Likewise, for pixels with a wet period, there was a local minimum then the maximum and then a

local minimum which were assigned time-sequentially to the R-G-B space. The maximum was assigned to the green band and the two minima were assigned to the red and blue bands with the greater minimum averaged with the beginning or end value of the time-series depending on whether it was before or after the maximum. For pixels with more than two changes, it was not possible to maintain the structure of the trend in an R-G-B reduction and the mean of the entire period was taken for all three points to show the average annual percent of time for which water was present. These R-G-B reduction heuristics were also applied to the stable seasonal class to show the continuum of changes with intensity <50%.

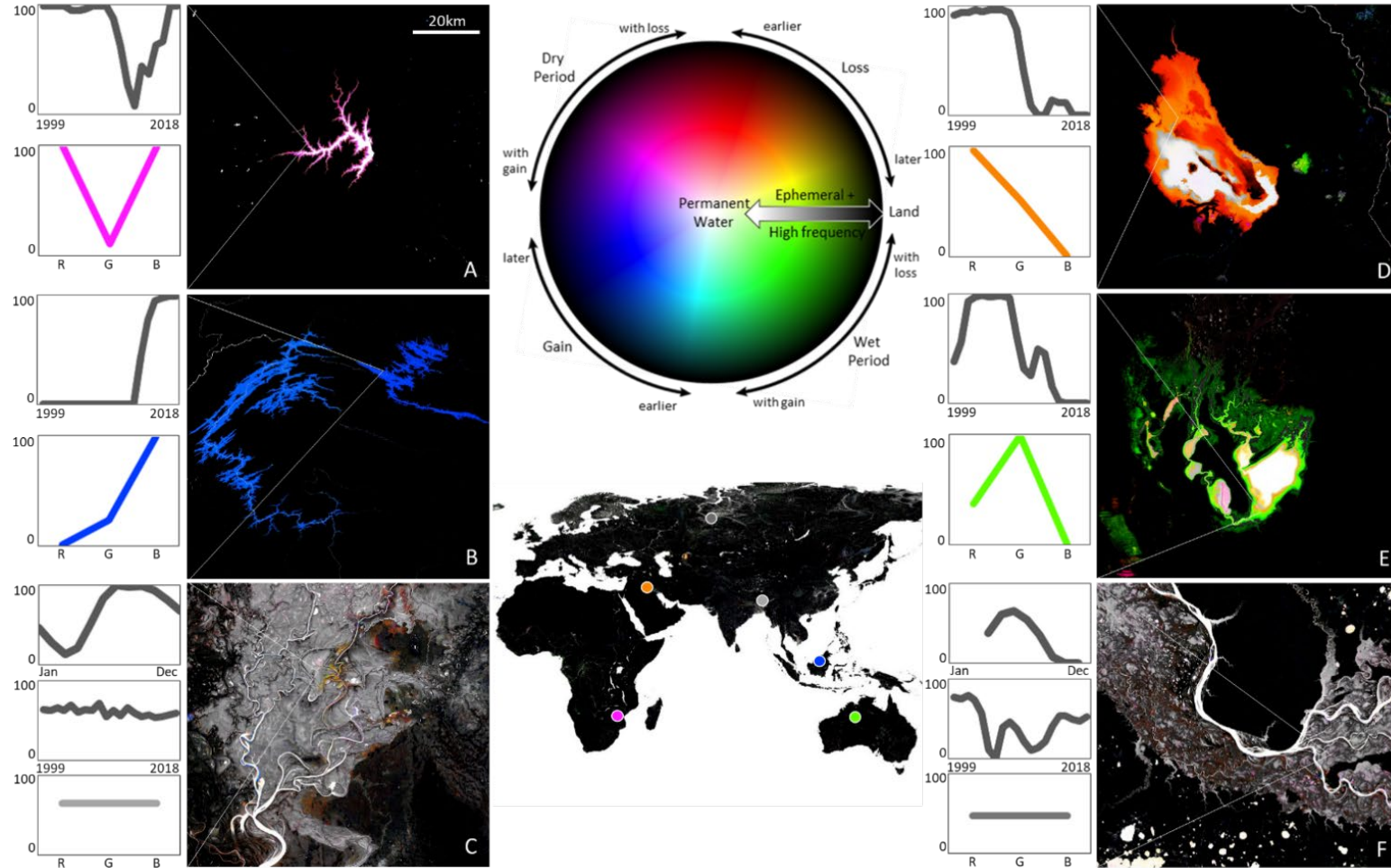


Figure 3.2: Examples of classes of the water dynamics map. Each example has the annual water percent time-series and resulting R-G-B reduction for a given pixel. For the stable seasonal and high frequency examples, the 17-year monthly mean water percent is also shown. (A) Dry period: Chicamba Real Dam, Mozambique. (B) Gain: Bakun Dam, Malaysia. (C) Stable seasonal: Meghna River floodplain, Bangladesh. (D) Loss: Razazza Lake, Iraq. (E) Wet period: Lake Gregory, Australia. (F) High frequency: Ob River floodplain, Russia.

3.2.4 Landsat time-series sample

A probability sample-based assessment was conducted to estimate areas and validate the inter-annual dynamics map from 1999-2018. The map was clipped using the Global Administrative Areas dataset (University of California, Berkley 2012) to exclude coastal and ocean waters, consistent with previous studies (Feng et al., 2016; Pekel et al., 2016). This assessment is for all areas with data within 56°S-75°N, excluding Greenland.

Twelve strata derived using the mapped classes were created from the time-series analysis, and fifty 0.00025° pixels were randomly selected per stratum, totaling 600 sampled pixels (Figure 3.3). Mapped permanent water was separated into two strata: 1) the high confidence permanent water stratum which included all pixels whose R-G-B transformation resulted in each value $\geq 90\%$, and 2) the likely water stratum which included all pixels that did not meet the criteria defining the first stratum but that had mean annual open water present for $\geq 90\%$ of the observable portion of the year and inter-annual variation $\leq 33\%$. Permanent land was separated into three strata to target possible omission errors. The land buffer stratum included all land pixels within 1km of any water class, the high confidence land stratum included all remaining land pixels whose R-G-B transformation resulted in each value $\leq 10\%$, and the likely land stratum included all land pixels that did not meet that criteria but that had mean annual open water present for $\leq 10\%$ of the observable portion of the year and inter-annual variation $\leq 33\%$. There was an additional sparse-data stratum which was defined as all pixels with < 10 years of observations or < 15

total observations. The sparse-data stratum was used for area estimation, but not for the accuracy assessment because it did not have a map dynamic type label.



Figure 3.3: Distribution of sampled pixels of the Landsat time series.

Stratification was essential to ensure that sufficient sample sizes were allocated to each class given that inland surface water only covers 3-4% of the planet and of that only a small fraction belongs to each of the dynamic classes (Pekel et al., 2016). It was also necessary to have the strata take into account the entire time period because 40% of surface water area was found to be dynamic. The reference data must also cover the entire time period monitored and the only data source for such a task is the Landsat archive. The standard for reference data is that the reference classification must be of equal or higher quality than the map itself. Manual interpretation of the time-series of individual sample pixels provided this more accurate time-series characterization relative to the output of our global-scale algorithm (Olofsson et al., 2014). For the reference data, an observation from every month was selected as a compromise between exhaustive interpretation of every scene and feasibility that maintained sufficient temporal density to capture inter-annual water dynamics.

Because the data were processed in geographic (Lat/Long) at 0.00025° resolution and not in equal area projection, pixels differ in area depending on latitude. Pixels were sampled with inclusion probabilities proportional to the area of the pixel using the following method (Brewer and Hanif, 1982). All pixels were listed per stratum and the cumulative sum of pixel areas was computed for all pixels previous to and including the current pixel in the list. Fifty floating point numbers between zero and the total stratum area were randomly generated. For each of the randomly selected numbers, the first pixel that had cumulative area larger than this number was selected. This protocol results in a stratified random sample for which the inclusion probability of a pixel in each stratum is proportional to the area of the pixel.

For each sampled pixel, a Landsat observation was randomly selected from each month for each year, resulting in up to 240 scenes being visually interpreted for each pixel. If for a given scene the sampled pixel was flagged as cloud, a new scene would be randomly selected from the same month if available, otherwise the original scene would be retained for interpretation. For each sampled pixel, a html page was built with thumbnails of all selected Landsat scenes (Figure 3.4). For each thumbnail, the pixel was labeled as land, water, or bad data through visual interpretation of the Landsat data and auxiliary high-resolution data from Google Earth was used to provide additional context. Since the data are resampled to 0.00025° via the nearest neighbor method, each 0.00025° pixel retains the spectral reflectance data of the nearest 30x30m pixel in the original Landsat data, which is in Universal Transverse Mercator (UTM) projection, and the footprint of the UTM pixel was utilized when considering the high-resolution data from Google Earth.

These land and water labels in the reference data were used to evaluate the inter-annual water dynamics map. A total of 87,926 scenes (600 sampled pixels x 12 months x 20 years minus months with no available scenes) were visually interpreted as land, water, or bad data, and out of these, 57,230 observations were labeled as land or water both through visual interpretation and via the map classification trees. While this is a large number of scenes, it was manageable because only the 600 sample pixels needed to be interpreted, many of which were stable through time. The individual visual interpretations were aggregated to form an annual time series by calculating the percent of clear reference observations that were water per year and smoothed with a 3-year mean moving window as was done with the algorithm-generated time-series. This reference time-series was input to the water dynamics model (Section 2.2) to generate class labels for each sampled pixel.

These class labels of the reference data were used to estimate area of the water dynamic classes and aggregations of the classes. Additionally, the area that is inundated each year for greater than 25, 50, 75, and 90 and equal to 100 percent of the time was calculated from the annual percent values of each sampled pixel. Using this same stratified sample, we estimate user's and producer's accuracies for the trend classes. Details of area and accuracy estimation calculations can be found in the Appendix.

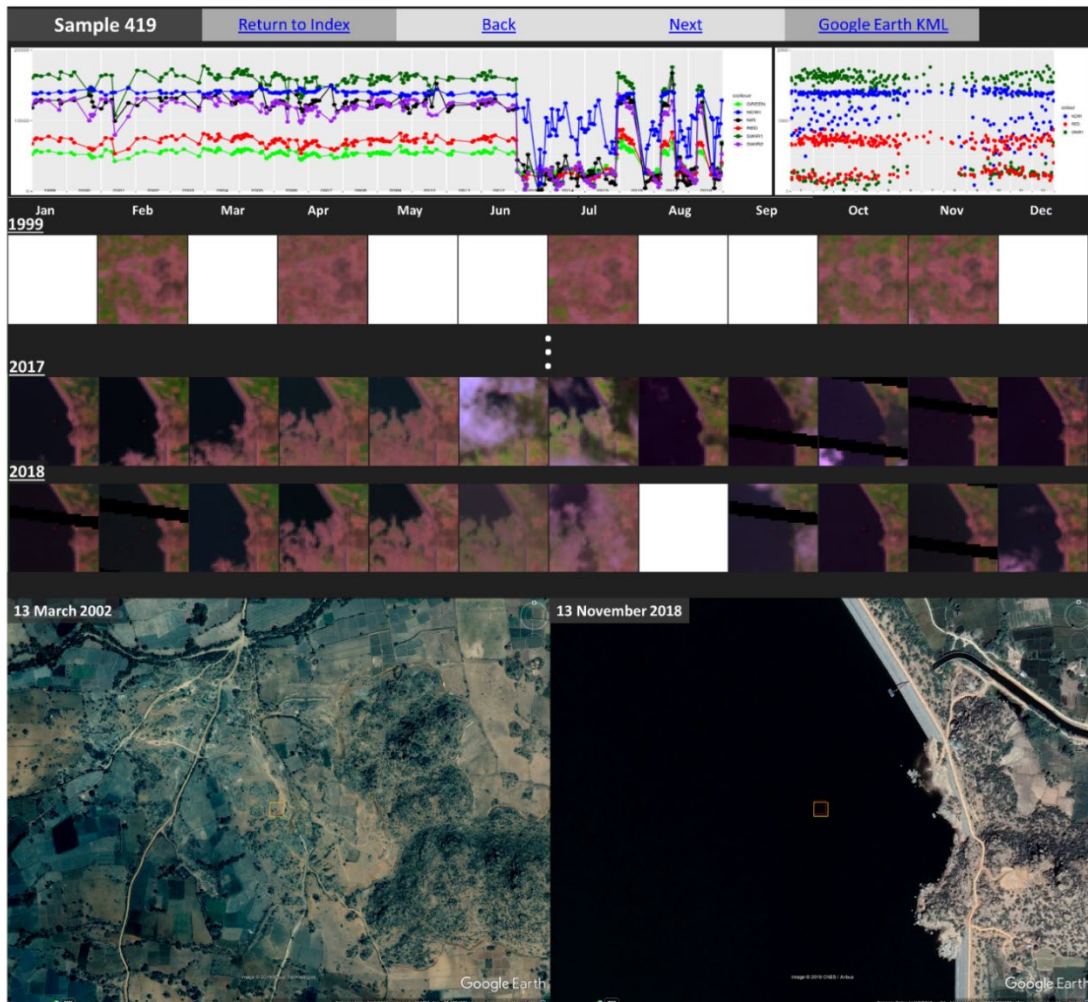


Figure 3.4: Example sampled pixel from the wet period stratum, centered at $16.189375^{\circ}\text{N}$, $77.659375^{\circ}\text{E}$ within the fluctuating footprint of Rayalumpad Reservoir in Telangana, India. The reservoir was constructed in 2009, first flooded the sampled pixel in 2013 and remained flooded through 2015, and then seasonally inundated the sampled pixel 2016-2018. The pixel is outlined in red in each of the Landsat thumbnails (SWIR1-NIR-red) and in the images from Google Earth, with an additional yellow outline for the source UTM pixel footprint. The graphs at the top are time series of the spectral reflectance of the pixel to aid interpretation (Green reflectance in light green, red reflectance in red, NIR in black, SWIR1 in dark green, SWIR2 in purple, and NDWI in blue). Each Landsat scene could be individually marked as land, water, or bad data or a month, year, or the whole collection could be labeled as one of these classes. The full reference html page includes all months and years 1999-2018 and can be viewed here: <https://glad.geog.umd.edu/timeSeriesReference/pagesUTM/sample419.html>.

3.2.5 Comparison with Pekel et al. (2016) dataset

The most comprehensive previous global surface water dataset is that of Pekel et al. (2016) with monthly water / not water maps from 1984-2018 with considerable data gaps pre-1999. They evaluate their product using a sample-based assessment that only quantifies water / not water state. The area estimates of change they provide are not produced using a probability-based sample of reference data but instead change is quantified from pixel counts, which ignores the biases inherent in the map products. Moreover, the multi-temporal maps made by Pekel et al. (2016) that identify change are principally bi-temporal, consisting of the change in percent of an epoch with open water present between two epochs, and a time-1 time-2 transition map. The transition map of Pekel et al. (2016) is derived from the first year with sufficient surface observations in the Landsat Thematic Mapper time-series, starting in 1984 through 2000, and a last year of 2018, for the map update released this year. The transition map represents the classes in a transition matrix generated from the annual labels of permanent, seasonal, and land in the first and last year, an approach that ignores all intervening years except for pixels where the first and last year both have land labels. Permanent water on an annual time-scale is defined as all months with data flagged as water, and seasonal water is defined as having at least one month flagged as water and at least one month flagged as land. In the case of land labels for both the first and last year, the annual time-series is checked whether or not there was ever labeled water between the start and end years. If there is such ephemeral water, it is determined whether permanent or seasonal water states were observed more frequently and the pixel is labeled ephemeral permanent or ephemeral seasonal

according to a majority rule. If either the first or last year are water, the class label is assigned only using bi-temporal first and last year labels.

Pekel et al. (2016) performed an extensive validation on their water / not water classification, but did not include the entirety of the map in the sampling frame. Importantly, their omission sampling frame for south of 60°N was only within the SRTM Water Bodies Dataset (SWBD) and for north of 60°N within the water class of Feng et al. (2015) and did not validate change. In SWBD, all water bodies with a width smaller than 183m are removed, and thus the omission accuracy only applies to bodies of water having width larger than 183m that are within the SWBD, a data set derived from a period of 10 days in February 2000. Finally, they did not use the reference data to report map-based area summations or to estimate uncertainty bounds of reported areas. In this study, we extended the results of the Pekel et al. (2016) study by producing maps that report various change classes based on all the years of the study period, conducting an accuracy assessment that represented the entire map, and reporting sample-based estimates of area of change accompanied by standard errors to quantify uncertainty of these estimates.

We evaluated Pekel et al.'s (2016) global water dataset in three different ways. (1) To evaluate the monthly water product of Pekel et al. (2016), we calculated accuracies for the monthly water/non-water labels of Pekel et al. (2016) using the same single-date 5m reference data set described in Section 2.3.1 and performed the same steps of accuracy analysis as we did for our monthly product, which allows for accuracy estimates that apply to the whole map. Pekel et al.'s (2016) monthly data are labeled as water, land, or no observation and thus no threshold was needed for the

single-date validation. (2) In order to compare the sensitivity of our monthly water layers with those of Pekel et al. (2016) to detect and correctly identify change, we applied the same water dynamics model we developed in this study (Section 2.2) to the monthly water history of Pekel et al. (2016). This task was performed using the same rules applied in the creation of our change categories with the input monthly water history being from Pekel et al. (2016) instead of GLAD and with their water labels converted to 100% and not-water labels to 0% on a per month basis. This enabled us to create an annual time-series from monthly data in an identical manner for Pekel et al. (2016), GLAD, and the reference data set. Water dynamics were therefore modeled consistently across all three data sets. Accuracies for Pekel et al. (2016) and GLAD were subsequently assessed using the same method. (3) To evaluate the transition map of Pekel et al. (2016), we compared their transition labels against the water dynamics class of the reference data. Since the readily available transition map of Pekel et al. (2016) is from the first representative year to 2018 rather than 1999-2018, we computed a 1999-2018 transition map from their yearly water history according to the rules outlined in their published study. A one-to-one correspondence does not exist between the transition map labels and the class definitions developed in this study. In this case, we did not compute accuracies, but instead we have provided the confusion matrix. In this way, we are able to quantitatively compare the Pekel et al. (2016) bi-temporal water dynamics to a reference data set that is stratified on change and that more completely characterizes surface water dynamics.

3.3 Results

3.3.1 Maps

Monthly, seasonal, and annual water percent layers were created and maps of inter-annual dynamics for 1999-2018 were created for the entire year as well as for each set of three consecutive months. Natural dynamics such as the meandering of the rivers in the Ganges-Brahmaputra basin (Coleman, 1969) are observed as well as direct human change such as the expansion of rice cultivation and aquaculture (Davidson, 2014; Tessler et al., 2016; Zhao et al., 2008) (Figure 3.5). Large areas of water gain include the lakes of the Tibetan Plateau (Zhang et al., 2014), the prairie potholes of the USA and Canada (Zou et al., 2018), and the creation of reservoirs, particularly in Southeast Asia (Zarfl et al., 2015). Many of the large saline lakes of the world have all substantially diminished in area since 1999 (Wurtsbaugh et al., 2017). Much of the area with multiple transitions between open water and land occur within wetlands and floodplains. In addition to visualizing inter-annual dynamics, mean water percent was also calculated per month for the period of 1999-2018, enabling analysis of seasonal water presence (Figure 3.6). Consistent annual seasonal open water can be seen in many of the floodplains around the world, for example, the Barotse floodplain in Zambia (Cai et al., 2017). Direct human seasonal dynamics such as single and double cropping of rice paddies can also be distinguished through the annual or biannual open water flooding regime. While much of the measured seasonal and inter-annual fluctuation is due to true variation in surface water presence, some of this fluctuation in open water presence, particularly in wetlands, is due to variation in vegetation levels that obscure the water surface. All layers are

available for visualization or download at www.glad.umd.edu/dataset/global-surface-water-dynamics.

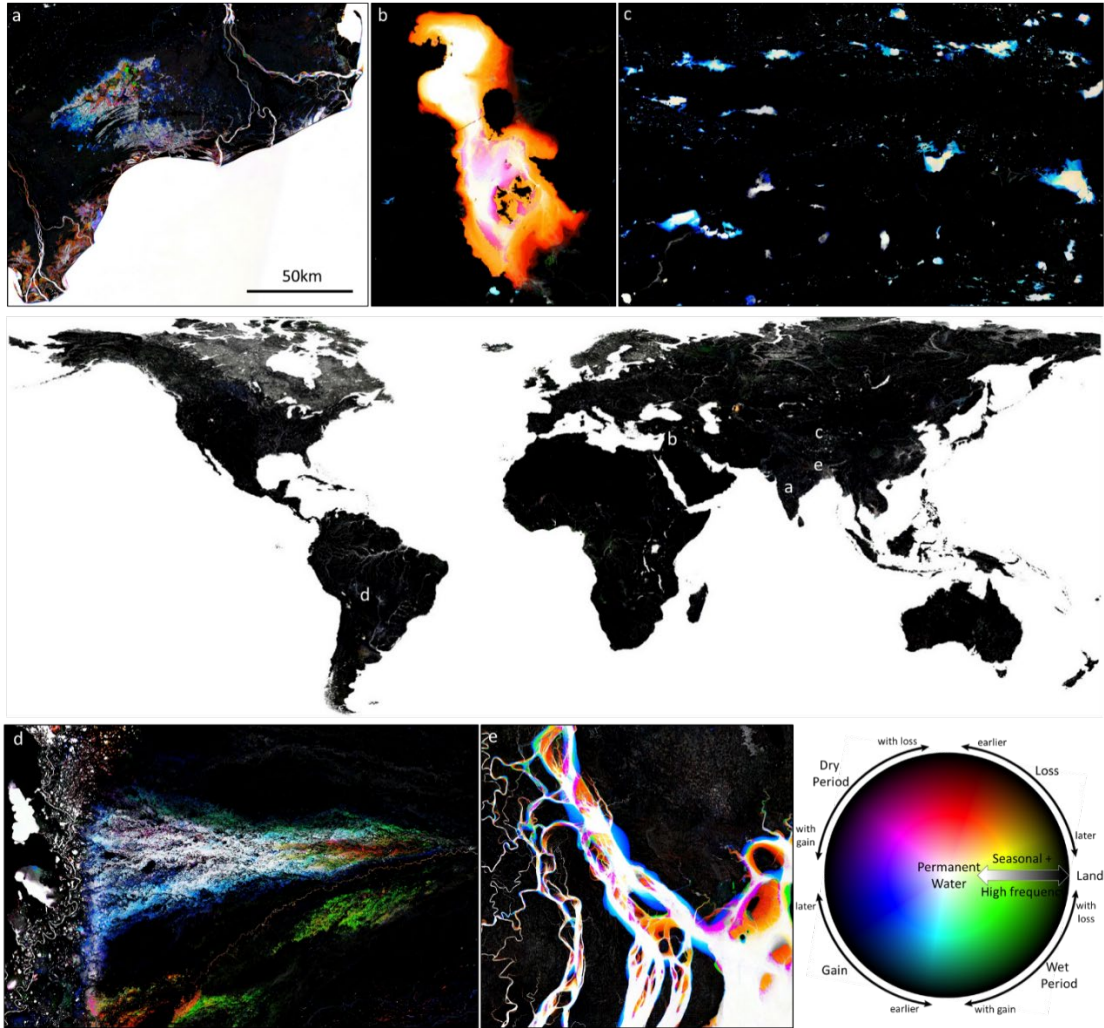


Figure 3.5: 1999-2018 inter-annual water dynamics map examples for all 12 months with hues representing the type of change dynamic, saturation the intensity of the change, and value or brightness representing the maximum percent of a year that was inundated. All examples are shown at the same scale. (a) Expansion of aquaculture and shifting management practices on the coast of India. (b) Dramatic reduction of Lake Urmia in Iran, with slight recovery. (c) Increase of lakes across the Tibetan Plateau. (d) Shifting open water patterns in the Pantanal in Brazil, the largest wetland in the world. (e) Meandering of the Meghna River in Bangladesh by 10km and the growth of new islands in the Bay of Bengal.

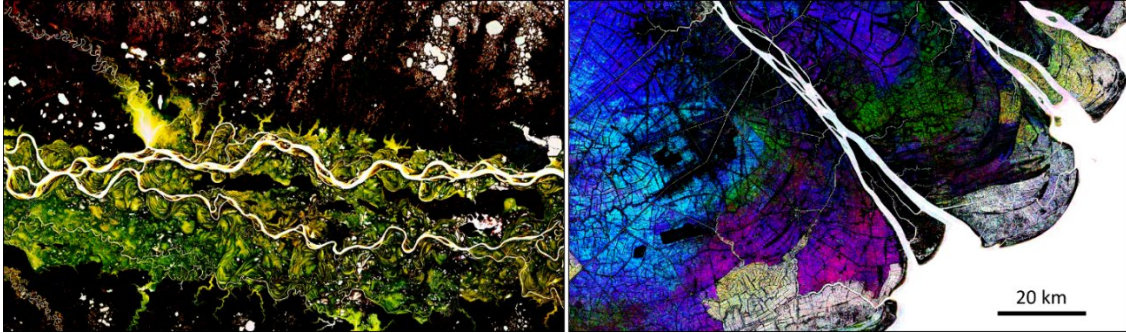


Figure 3.6: 1999-2018 seasonal water examples. Both examples are shown at the same scale. Left: R-G-B of monthly mean water percent of April-June-August showing the seasonal floodplains of the Ob River, Russia. Right: R-G-B of monthly mean water percent of June-August-October showing the various rice and aquaculture flooding cycles in the Mekong Delta, Vietnam with the magenta areas experiencing two separate open water flooding periods and the green areas experiencing three separate open water flooding periods.

We evaluated the effects of the filtering and smoothing of the time-series on the output inter-annual surface water dynamics maps. The filtering of anomalous water detections caused 0.17% of the final area mapped as land to be classified as land rather than a dynamic class and the filtering of anomalous land detections caused 0.29% of final area mapped as permanent water to be classified as permanent water rather than a dynamic class. We evaluated the impact of using 30% as the magnitude threshold defining a transition and found that if instead the threshold was set at 10, 20, 40, or 50 percent that 0.16-0.33% of the entire continental area changes class or, equivalently, 5.1-8.7% of the area mapped as permanent or dynamic water classes. Using the single year annual time-series as input to the water dynamics model instead of the 3-year mean annual time-series has a much larger impact, with 1.8% of the entire continental area changing class, or as a percent of the area mapped as permanent or dynamic water classes 45% changes class and increases the total area mapped as dynamic by 4.2%.

3.3.2 *Sample-based area estimates*

We estimated 2,928,992 ($\pm 93,027$) km² of the continental area to be permanent open water from 1999-2018 (Table 3.1). Areas that were open water at any point during 1999-2018 totaled 4,815,478 ($\pm 82,986$) km². There was a total of 138,011 ($\pm 28,163$) km² that had unidirectional gain of open surface water and 53,154 ($\pm 10,883$) km² that had unidirectional loss of open water, whereas, areas that changed between persistent water and persistent land two or more times through the period totaled 950,719 ($\pm 104,034$) km². The mean annual area with open water present for $\geq 50\%$ of the observable portion of the year was 3,687,781 km² (standard deviation over all years of the annual area estimates = 46,440 km²).

Table 3.1: Area estimates of trends with associated uncertainty of open water within the continental area between 75°N and 56°S as delineated by the Global Administrative Areas dataset (University of California, Berkeley 2012) and excluding Greenland. The last four categories are aggregates of the classes above.

	Area (\pm SE) km ²	Percent of total area	Percent of all water	Class definition
Land	126,971,335 (\pm 82,868)	96.34 (\pm 0.06)	—	Mean water percent \leq 10% and inter-annual variability \leq 33%
Permanent water	2,928,992 (\pm 93,027)	2.22 (\pm 0.07)	60.82 (\pm 1.93)	Mean water percent \geq 90% and inter-annual variability \leq 33%
Stable seasonal	735,347 (\pm 99,792)	0.57 (\pm 0.08)	15.69 (\pm 2.07)	Intra-annual variability with inter-annual variability $<$ 50%
Gain	138,011 (\pm 28,163)	0.10 (\pm 0.02)	2.87 (\pm 0.58)	Land-dominant to water-dominant
Loss	53,154 (\pm 10,883)	0.04 (\pm 0.01)	1.10 (\pm 0.23)	Water-dominant to land-dominant
Dry period	47,344 (\pm 8,982)	0.04 (\pm 0.01)	0.98 (\pm 0.19)	Water-dominant to land-dominant to water-dominant
Wet period	120,543 (\pm 49,543)	0.09 (\pm 0.04)	2.50 (\pm 1.03)	Land-dominant to water-dominant to land-dominant
High frequency	784,417 (\pm 93,460)	0.60 (\pm 0.07)	16.29 (\pm 1.94)	3+ transitions between water-dominant and land-dominant
Multiple transitions	950,719 (\pm 104,034)	0.72 (\pm 0.08)	19.74 (\pm 2.16)	Dry period, wet period, and high frequency (2+ transitions)
All change types	1,141,884 (\pm 106,120)	0.87 (\pm 0.08)	23.71 (\pm 2.20)	Gain, loss, dry period, wet period, high frequency
All dynamic types	1,895,159 (\pm 114,006)	1.44 (\pm 0.09)	39.36 (\pm 2.37)	Gain, loss, dry period, wet period, high frequency, stable seasonal
All with water	4,815,478 (\pm 82,986)	3.65 (\pm 0.06)	100.00	Permanent water, stable seasonal, gain, loss, dry period, wet period, high frequency

3.3.3 Accuracy of classes of water dynamics derived from time-series

The accuracy of each class of water dynamics derived from our dataset for 1999-2018 varied greatly by the number of changes represented by each class. The same was true for the accuracies of the classes derived from the monthly layers of the study by Pekel et al. (2016) when the same water dynamics model developed in our study was applied to the Pekel et al. (2016) data. The resulting map and labels derived from the water dynamics model were not produced by Pekel et al. (2016) but it is instructive to examine the accuracy of their product when their data are translated through this model. Accuracies were highest for land with the user's and producer's accuracies of our study at 99.9 (± 0.0)% and 99.7 (± 0.1)%, followed by permanent water with user's and producer's accuracies of 97.8 (± 1.8)% and 85.8 (± 2.4)%, both of which had similar accuracies for Pekel et al.'s (2016) dataset. These are the largest classes, accounting for 98.6% (± 0.1)% of the global continental area.

The accuracies of each of the classes where pixels sometimes are land and sometimes have water, hereafter referred to as 'all dynamic types', are much lower and for the GLAD dataset have higher rates of commission than omission (Table 3.2). For each of the dynamic types the data from our study have lower rates of omission than the results from using Pekel et al.'s (2016) monthly water history, and for three out of the six dynamic types our study has lower rates of commission. However, many of the misclassifications are between the change and seasonal classes themselves, rather than missing the transitory nature of the surface water entirely, as can be seen by the accuracies when all dynamic types are aggregated into a single class. Our study resulted in user's and producer's accuracies for the class "all

dynamic types” of 68.3(\pm 3.9)% and 93.4(\pm 0.6)%, respectively. Pekel et al. (2016) yielded user’s and producer’s accuracies for “all dynamic types” of 46.1(\pm 19.3.)% and 60.2(\pm 4.9)%. However, one of the sampled pixels in the land buffer stratum was labelled stable seasonal using the Pekel et al. (2016) dataset, and if this one sample unit is removed from the analysis, the user’s accuracy of “all dynamic types” increases to 78.5(\pm 5.0)% and the producer’s accuracy remains the same. Thus the user’s accuracy result is strongly impacted by one influential “outlier” sample pixel. Through comparison between the producer’s accuracies of ‘all dynamic types’ and of ‘all change types’, 93.4(\pm 2.7) % and 70.6(\pm 6.1)% respectively, we can see that many of the omissions of change occur when the sample pixel is classified in the map as stable seasonal, since that is the only additional class in ‘all dynamic types’. The amplitude threshold of the time-series for a pixel to be labeled as change rather than seasonal is 50%, meaning a pixel must gain or lose the equivalent of half a year of open water one or more times through the 20 years of the study. Thus, in this case, the amplitude of the inter-annual changes in the algorithm generated time-series was below the threshold of 50% to be labeled as change and was thus labeled stable seasonal, but in the reference data time-series was greater than the threshold of 50% and was labeled with a change type. The distribution of omission and commission errors can be seen in Table 3.3.

Table 3.2: The user's and producer's accuracies of the classes of water dynamics from the time-series data of this study and of Pekel et al. (2016) when the water dynamics model is applied to each monthly water history dataset and to the reference data. The last four categories are aggregates of the classes above and a sample pixel is considered correct for the aggregate if it is in one of the contributing classes. See Table 3.1 for class definitions.

	GLAD Accuracy		Accuracy of GLAD water dynamics model applied to Pekel et al. (2016) monthly water history	
	User's	Producer's	User's	Producer's
Land	99.9 (± 0.0)	99.7 (± 0.1)	99.5 (± 0.1)	99.1 (± 0.8)
Permanent water	97.8 (± 1.8)	85.8 (± 2.4)	95.1 (± 1.8)	89.9 (± 2.6)
Stable seasonal	44.0 (± 7.1)	73.0 (± 5.6)	17.4 (± 12.1)	36.3 (± 8.3)
Gain	59.6 (± 7.2)	74.8 (± 13.9)	48.0 (± 12.8)	45.4 (± 10.9)
Loss	30.0 (± 6.5)	86.2 (± 7.4)	49.8 (± 19.3)	65.5 (± 11.4)
Dry period	46.0 (± 7.1)	81.1 (± 11.8)	17.7 (± 8.0)	31.7 (± 9.5)
Wet period	34.0 (± 6.8)	39.8 (± 16.7)	62.5 (± 15.1)	37.5 (± 17.5)
High frequency	54.3 (± 7.4)	54.9 (± 6.2)	50.4 (± 9.3)	35.4 (± 7.1)
Multiple transitions	58.2 (± 5.8)	62.2 (± 6.6)	54.1 (± 7.9)	40.3 (± 6.4)
All change types	60.0 (± 4.6)	70.6 (± 6.1)	62.8 (± 6.9)	50.0 (± 5.8)
All dynamic types	68.3 (± 3.9)	93.4 (± 2.7)	46.1 (± 19.3)	60.2 (± 4.9)
All with water	92.1 (± 1.6)	98.6 (± 0.6)	79.1 (± 15.5)	85.9 (± 2.3)

Table 3.3: Confusion matrix of GLAD water dynamics map with the reference classification. In row i and column j , the left half of the cell represents in a gray gradient the estimated percent of pixels labeled i in the reference data and that were mapped j in GLAD, and the right half of the cell represents in a green gradient the estimated percent of pixels mapped j in GLAD that were labeled i in the reference data. The grays not along the center diagonal of correct classification show the distribution of omission and the greens show the distribution of commission. The percent estimates were derived from the estimated area of each (i,j) cell.

GLAD water dynamics classes map 1999-2018

		Land		Permanent water		Stable seasonal		Gain		Loss		Dry period		Wet period		High frequency	
Reference	Land	99.7	99.9	-	-	0.2	18.0	0.0	8.5	0.0	28.0	0.0	8.0	0.0	20.0	0.1	10.9
	Permanent water	-	-	86.1	97.8	6.8	16.0	0.5	8.5	0.9	18.0	0.2	8.0	0.5	10.0	4.9	19.6
	Stable seasonal	7.4	0.0	0.8	0.2	73.0	44.0	1.4	6.4	2.5	12.0	0.7	6.0	0.4	2.0	12.8	13.0
	Gain	-	-	-	-	17.9	2.0	74.8	59.6	-	-	1.2	2.0	6.4	6.0	-	-
	Loss	-	-	-	-	-	-	-	-	86.2	30.0	3.1	2.0	10.6	4.0	-	-
	Dry Period	-	-	12.7	0.2	-	-	-	-	-	-	81.3	46.0	6.0	2.0	-	-
	Wet period	-	-	37.4	1.8	-	-	6.1	4.3	2.6	2.0	-	-	39.8	34.0	13.2	2.2
	High frequency	1.4	0.0	-	-	31.8	20.0	2.8	12.8	2.1	10.0	3.0	28.0	4.2	22.0	54.9	54.3

We also compared the reference data time-series classification to the transition map of Pekel et al. (2016) (Table 3.4). The transition map underestimates water presence, as a number of water extent and dynamics classes are labeled as permanent land in Pekel et al (2016). Specifically, 6% of the reference area of permanent water is labeled as land, 43% of seasonal water area is labeled as land, and 41% of the area of all the change classes is labeled as land. Change was also underestimated with an additional 11% of reference change area classified as permanent water in Pekel et al.'s (2016) map. While there is not a one-to-one correspondence between the reference class definitions and Pekel et al.'s (2016) definitions, the nature of the change is also misidentified; for example, 45% of what was classified by Pekel et al. (2016) as new permanent water from land and 52% of lost permanent water to land actually experienced multiple transitions between land-dominated and water-dominated states, the 'high frequency' reference class. The three classes of Pekel et al. (2016) which had the majority of the area correctly mapped within the corresponding reference classes are land with 99%, permanent water with 93%, and ephemeral permanent with 100% within the corresponding reference classes. The remaining classes of Pekel et al. (2016) have the majority of their area in a reference class with a definition that does not overlap. In summary, the Pekel et al. (2016) map omits considerable areas of surface water extent and change and mischaracterizes change types.

Table 3.4: Confusion matrix of Pekel et al. (2016) transition map 1999-2018 with the reference classification. In row i and column j , the left half of the cell represents in a gray gradient the estimated percent of pixels labeled i in the reference data and that were mapped j by Pekel et al. (2016), and the right half of the cell represents in an orange gradient the estimated percent of pixels mapped j by Pekel et al. (2016) that were labeled i in the reference data. The percent estimates were derived from the estimated area of each (i,j) cell.

		Pekel et al. (2016) transition map 1999-2018																					
		Land		Permanent water		Seasonal		New permanent		New seasonal		Seasonal to permanent		Lost permanent		Lost seasonal		Permanent to seasonal		Ephemeral permanent		Ephemeral seasonal	
Reference	Land	99.1	99.3	0.0	0.6	0.8	77.3	-	-	-	-	-	-	-	-	0.0	16.7	-	-	-	-	0.0	36.8
	Permanent water	6.4	0.1	88.6	93.0	1.4	2.9	0.9	24.6	0.7	12.1	1.1	52.6	0.1	3.4	-	-	0.9	34.3	-	-	0.1	1.3
	Stable seasonal	43.1	0.3	6.9	1.9	24.2	12.8	-	-	7.6	31.0	-	-	0.4	3.6	10.5	52.2	1.2	12.6	-	-	6.0	35.2
	Gain	28.4	0.0	6.5	0.3	23.5	2.2	21.0	27.3	15.3	11.2	5.3	11.9	-	-	-	-	-	-	-	-	-	-
	Loss	5.7	0.0	-	-	11.5	0.4	-	-	-	-	-	-	65.5	41.4	17.2	6.2	-	-	-	-	-	-
	Dry period	6.0	0.0	26.8	0.5	21.2	0.7	-	-	7.1	1.9	7.1	5.7	-	-	7.1	2.3	24.8	16.2	-	-	-	-
	Wet period	48.0	0.0	2.4	0.1	4.7	0.4	2.4	2.8	25.6	16.9	-	-	-	-	4.9	4.0	-	-	4.7	26.4	7.1	6.8
	High frequency	46.5	0.3	13.7	3.7	6.1	3.2	6.2	45.3	6.5	27.0	2.3	29.8	5.9	51.6	3.7	18.7	3.6	36.9	2.1	73.6	3.3	19.9

3.4 Discussion

This study provides the first sample-based area estimates of global surface water extent and change. The method employs mapped surface water change to stratify the global land surface and uses a probability sample of reference data to produce unbiased estimators of area of surface water extent and change, accompanied by standard errors to quantify the associated uncertainties of the area estimates. Good practice methodology establishes that areas should be estimated via a sample-based analysis rather than by merely summing the area of class pixels in the map (Olofsson et al., 2014; Stehman, 2013). Given that there are errors in all maps, pixel counting will generally result in an over or under estimation of the true area with unknown magnitude. In contrast, a probability sample-based analysis allows for estimation of area bounded by quantified uncertainties that can be appropriately used in science and policy applications (Eggleston et al., 2006; Olofsson et al., 2013; Penman et al., 2016).

The time-series sample provides class accuracies of the inter-annual dynamics map, but more importantly, area estimators of surface water extent and change accompanied by standard errors to quantify uncertainty of these estimates. This analysis enables proper use of the inter-annual dynamics map as well as highlights the challenges of time-series change mapping. These two analyses extend the validation of Pekel et al. (2016) in that (1) accuracy estimates represent the entire map, and (2) the reference sample data explicitly evaluate change were used to calculate unbiased

estimators of areas, and (3) standard errors were reported to provide an assessment of uncertainty of the area estimates.

Results illustrate that while pure water pixels are usually easily discriminated from land pixels, change between the two categories is very difficult to characterize in mixed pixels and mixed pixels are prevalent as 22.8% of all 30m pixels with water present also have land present (Chapter 2). We found that the amount of area that has fluctuating rates of open water presence far exceeds the area that has unidirectional trends of gain and loss (Table 3.1). Of the pixels that experienced change in surface water, 83% did not experience unidirectional change. These results demonstrate how difficult it is to map water dynamics accurately at a 30m spatial resolution and highlights the need for time-series of higher spatial resolution data, such as Sentinel-2 (10-20m with 5 day revisit), or commercial data such as Planet (3m with daily revisit) to improve change area estimation. Radar data sources, such as Sentinel-1, also offer a path forward for mapping open water, with advantages in both the spatial and temporal domains compared to Landsat, particularly in rainy seasons and flood events due to radar's ability to penetrate clouds. However, since the first Sentinel-2 satellite was launched in 2015, the first of Planet in 2014, and the first of Sentinel-1 in 2014, historical analysis before these dates will still rely on Landsat.

It is unknown how much surface water is left undetected due to being under forest cover or other vegetation obscuring the surface of the water from above. As a result, it is unknown how much variation in open water presence is due to variation in vegetation cover rather than surface water presence. Much of the area of stable seasonal and multiple transitions is within natural wetlands. These are areas that

fluctuate greatly in both surface water extent as well as vegetation extent and density as part of a natural cycle. There have been various efforts to quantify wetland extent at regional and global extents, but as of yet, there is no consensus on global wetland area with some estimates double the area of others (Davidson et al., 2018), reflecting the current lack of consistency among map products of wetland extent (Hu et al., 2017). While coarser resolution products of global mapped surface water inundation exist (Fluet-Chouinard et al., 2015; Papa et al., 2010), no global inundation maps exist at medium spatial and temporal resolution. Medium resolution synthetic aperture radar has been used at a regional scale to map inundation during the wet and dry seasons, including in the forest (Hess et al., 2015).

3.4.1 Area comparison

Having reference data for every year enabled estimation of the mean annual area with various frequencies of open water presence (Figure 3.7) and the standard deviation (SD) over all years of the annual area estimates. For example, 3.13 million km² (SD = 0.06 million km²) has open water $\geq 90\%$ of the year, 3.69 (SD=0.04) million km² has open water $>50\%$ of the year, and 4.12 (SD=0.05) million km² is has open water $\geq 25\%$ of the year. These estimated areas represent the continental area within 56°S and 75°N delineated by the Global Administrative Areas dataset (GADM) (University of California, Berkley 2012) and exclude Greenland. Existing Landsat-based published studies fall within the range of annual areas with associated SDs for different rates of open water presence (Chen et al., 2015; Feng et al., 2016; Pekel et al., 2016; Yamazaki et al., 2015) (Figure 3.7). All but Pekel et al. (2016) use the Global Land Survey collection, which is comprised of single Landsat scenes from

isolated years, with some scenes selected from surrounding years instead, rendering analysis of seasonality impossible (Gutman et al., 2008; Tucker et al., 2004). Two other Landsat based products map sub-categories of global open water with an estimate of the global areas of lakes of 4.76 million km² by Verpoorter et al. (2014) and an estimate of the global area of rivers of 0.773 (\pm 0.079) million km² by Allen and Pavelsky (2018).

Pekel et al. (2016) report 2.78 million km² of permanent water and 0.81 million km² of seasonal water October 2014 - October 2015, where seasonal is defined as at least one month being labeled as land and at least one month being labeled as water. Pekel et al. (2016) use an upper bound of 78°N and the coast is also delineated by GADM. Pekel et al. (2016) additionally provide two time-series aggregate areas, 4.46 million km² with open water at any point between 1984 and 2015 and 2.4 million km² with permanent water from 1984-2015. For 1999-2018, we estimate 4.82 (\pm 0.08) million km² to be one of any of our water classes and 2.93 (\pm 0.09) million km² to be permanent open water as defined in this study (Table 3.1) and 2.43 (\pm 0.13) million km² to be permanent open water if we apply the strictest definition of 100% water detections. Although the studies cover two different time intervals, this strictest estimate from our analysis (2.43 million km²) nearly matches Pekel et al.'s (2016) permanent water estimate of 2.4 million km². Our estimate for the area in any of our water classes is 0.36 million km² larger than Pekel et al.'s (2016) area of water at any time, and if we broaden our definition to include water at any time, our estimate is 9.48 (\pm 1.97) million km² which is over twice as large as Pekel et al.'s (2016) reported area for 1984-2015. This larger estimate includes all

sample units that had a mean annual open water presence percent $\leq 10\%$ and inter-annual variation $\leq 33\%$ and also had at least one of the observations labeled water in the reference data, which is considered land in the smaller estimate. This estimate may be much larger due to the filtering of Pekel et al. (2016), which is not reproducibly described but is intended to remove cloud shadows, as well as, the bias of omission found for the Pekel et al. (2016) monthly water layers. Since our estimates are calculated only from the reference data and the strata areas, the GLAD map bias does not contribute to the reported difference. While not enough to account for the magnitude of the difference, our analysis also includes three additional years beyond the scope of Pekel et al.'s (2016) areas.

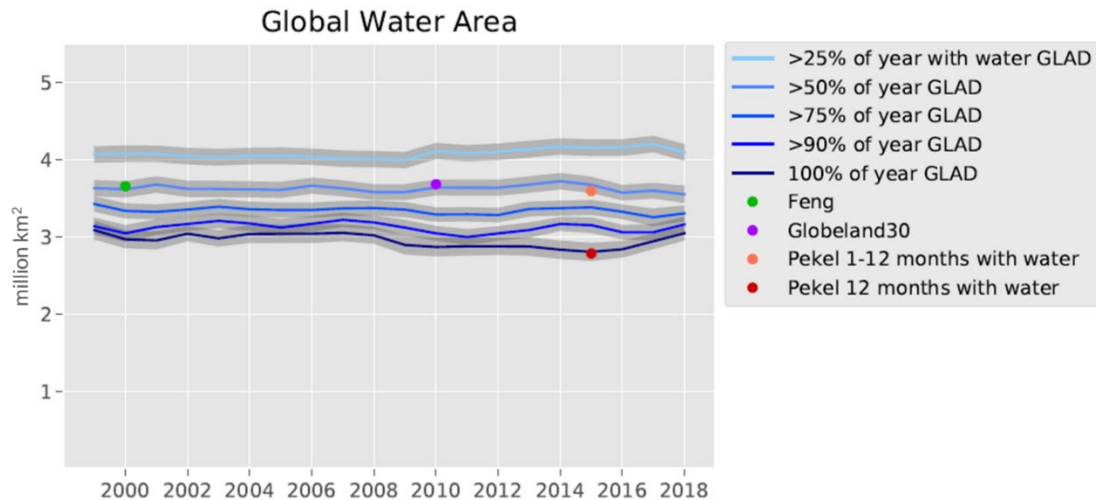


Figure 3.7: Global area estimates from this study and other previously published studies based on Landsat data. Each estimate from this study is the area with open water for the given percent of the year, and the gray area bounding it corresponds to the standard error of the estimate. Confidence intervals were not provided for the other studies.

Our study reports change areas based on the entire time-series rather than bi-temporally. Our sample-based estimates for 1999-2018 are 138,011 ($\pm 28,163$) km² of gained persistent water and 53,154 ($\pm 10,883$) km² of lost persistent water. Much of the increase is due to the creation of reservoirs (Zarfl et al., 2015) as well as climate impacts such as has caused the increase of lakes in the Tibetan plateau (Zhang et al., 2014) and in the prairie pothole region of North America (Zou et al., 2018) and much of the decrease comes from desiccation of many of the large saline lakes in the Middle East (Wurtsbaugh et al., 2017).

Given that the area that experienced multiple transitions between water and land on an annual time-scale was over 400% larger than the area with only unidirectional change (i.e. either loss or gain), it is imperative to look at the whole time-series to quantify trends of gain or loss. In contrast, previous studies only reported change areas bi-temporally from map pixel counts. Taking loss for example, Pekel et al. (2016) reported 162,000 km² of permanent water loss, 90,000 km² of which changed to land and 72,000 km² to seasonal water. These results cannot be appropriately compared to those of our study, because of differences in both their definition of loss and their time period. Pekel et al. (2016) defined loss as a transition from having all months labelled as water to having any months not labelled as water and this definition of loss was based on comparing only the first representative year (defined per pixel with a range of 1985-2000) and 2015, thereby ignoring all intervening years. The comparison of the Pekel et al. (2016) transition labels we generated for 1999-2018 versus the reference class for the time-series sample highlights this, showing that only 41% of the transition label lost permanent, defined

as permanent water to land, is actually loss when the intervening years are taken into account and 52% changes back and forth between land-dominant and water-dominant. The goal of the definitions of change types used in our study is to characterize the dominant behavior of the pixel through all 20 years, but change areas are inherently dependent on the definition and the complexity of defining change types increases for a land cover that is as dynamic as open surface water.

The areas reported in our study are the first to be estimated according to good practice guidelines. The areas reported by Pekel et al. (2016) were generated from summing the mapped area, or pixel counts. Doing so carries the classification bias into the estimated area. The validation performed by Pekel et al. (2016) within their study found a bias such that the number of seasonal water detections was 21-25% smaller than detected in their reference data set, which means there will be considerable bias in the areas computed from pixel counts. This bias is present even though their omission sampling frame itself omitted many smaller water bodies. Pekel et al. (2016) had separate sampling frames for omission and commission, and their omission sampling frame did not include many smaller water bodies due to only sampling within the SRTM Water Body Data (SWBD) for $<60^{\circ}\text{N}$. The SWBD only represents lakes that are at least the equivalent of 20x6 Landsat pixels, and only represents rivers that have a segment that is at least that same size (“SRTM Data Editing Rules,” 2003). Bodies of water with area $<0.1\text{km}^2$, which is a threshold roughly equal to the minimum size of SWBD water bodies, contribute a large fraction of total surface area of inland waters with estimates ranging between 12% and 17% of total inland water area (Downing et al., 2006; Verpoorter et al., 2014). Smaller water

bodies have a higher proportion of mixed pixels and are more likely to be transient, both of which make them harder to map. Since only pixels within the SWBD were eligible to be sampled (all other pixels had an inclusion probability of 0), the omission error estimates only apply to the area within that mask. The stratified random sample of reference data that we selected from the whole map and which targets each dynamic class yields unbiased estimators of area that are representative of the whole map, and the standard errors quantify the uncertainty of these area estimates. These uncertainty bounds inform the appropriate use of the estimates in further research as well as policy.

3.4.2 Maps

Water is unique compared to many other land cover types because it can be highly variable, literally ebbing and flowing over time, sometimes at regular annual rates and sometimes in long-term trends. Our approach to analyzing the time-series was to model high-confidence transitions for unidirectional and oscillating change dynamics. Monthly, seasonal, and annual percent water layers were generated and the annual time-series used to calculate a three-point model of inter-annual dynamics for deriving change categories. The resulting inter-annual dynamics map enables the viewing of mapped changes and their intensity (www.glad.umd.edu/dataset/global-surface-water-dynamics) (Figure 3.5). This map extends beyond the results of previous studies in that it characterizes eight different stable and dynamic classes in a continuum and from all years rather than just bi-temporally based on only the start and end dates. Given that the area that experienced multiple transitions between persistent water and persistent land was over four times larger than the area with

monotonic gain or loss, taking all years into account when mapping changes is critical for derivative studies that will use the water dynamic maps and/or area estimates.

In the previous chapter it was found that pure water and land pixels were identified with high accuracy within a single month (96.9 (± 0.9)% user's accuracy and 99.0 (± 0.3)% producer's accuracy), but there was greater classification error of mixed pixels (70.9 (± 1.6)% user's accuracy and 66.0 (± 3.7)% producer's accuracy). This extends to the inter-annual dynamics map and users should be aware that while core change pixels should be viewed with high confidence, edge and isolated pixels are more likely to be mapped inaccurately. Additionally, the dynamic classes have much lower accuracies than the permanent land and water classes.

3.5 Conclusion

This study presents the first set of area estimates for global open surface water extent and change that follow good practice guidance for area reporting (Eggleston et al., 2006; Olofsson et al., 2014; Penman et al., 2016; Stehman, 2013) as well as that use all Landsat imagery for the entire monitoring period to classify seven different temporal dynamics. We establish the necessity to evaluate time-series data through the entire period given that the area that transitioned multiple times between land and water inter-annually was four times larger than the area of unidirectional loss or gain. The maps produced in this study provide detailed visualizations of inter-annual surface water dynamics using the entire Landsat archive 1999-2018 that enable assessment of changes through the past 20 years. This analysis could be extended back to 1984 for regions that were regularly imaged from 1984-1998 such as the

United States and Australia. Map accuracy is high for permanent land, permanent water, and water change as a single theme, with considerably lower accuracies for individual water dynamics. The presented Landsat-based method will continue to be updated, with the current map products available through 2020, and is available for download at www.glad.umd.edu/dataset/global-surface-water-dynamics.

Chapter 4: Global seasonal inland water and ice dynamics

Abstract

Freezing temperatures and seasonal precipitation cause inland open surface water extent to vary dramatically through the year at both local and global scales. Though ice onset and melt patterns of inland waters have a significant impact on climate, and periodic inundation of floodplains is critical to natural ecosystem functioning, global seasonal dynamics of water and ice extent have not been well quantified. Here, we present the monthly areas of water and ice for 2019 with associated uncertainties divided into the areas of permanent and seasonal waters and into those that freeze over and those without ice presence. A probability-based sample of reference data was created from all 2019 Sentinel-2 observations for selected sample pixels together with 3m PlanetScope data. From this dataset, we find that 64% of permanent water freezes over, totaling $1.97 (\pm 0.21)$ million km^2 , and $1.13 (\pm 0.19)$ million km^2 remains liquid all year. Because of the vast area of freeze, June had the most open surface water with $3.91 (\pm 0.19)$ million km^2 and January had the least with $1.60 (\pm 0.21)$ million km^2 . Seasonal water that never has ice cover fluctuates between a January low of $0.31 (\pm 0.10)$ million km^2 to double the area in July ($0.63 (\pm 0.15)$ million km^2). In total, $4.86 (\pm 0.16)$ million km^2 had water presence at some point during the year. With this reference set we assessed the seasonal accuracy of the 30m Landsat-derived water layers of Pickens et al. (2020), and found an aggregate monthly user's accuracy of $88 (\pm 2)\%$ and producer's accuracy of $83 (\pm 2)\%$, showing

the potential to monitor water and ice dynamics spatially explicitly. Sentinel-2 provides an opportunity to map surface water and ice dynamics at fine spatial and temporal scales moving forward, and the Landsat mission enables potential assessment of long-term changes.

4.1 Introduction

Local and global hydrologic systems change dramatically through the year, with the annual freeze and thaw of the boreal biome resulting in dramatic river flow variation, and the annual progression of the intertropical convergence zone dictating seasonal inundation of tropical wetlands (Mitsch et al., 2010). Floodplain inundation is critical to ecosystem functioning (Poff et al., 1997) and areas of seasonal water are biodiversity hotspots, particularly for migrating species (Haig et al., 2019). Many wetlands are characterized by seasonal water pulses (Odum et al., 1995), and are among the most valuable ecosystems as centers for high biodiversity, carbon storage, pollution filtering, and flow regulation (de Groot et al., 2012). High latitude lakes and rivers cover a vast area with ecosystem services varying between the open water summer months and the ice-covered winter months, and including biogeochemical cycling (Wik et al., 2016), habitat provisioning (Vincent et al., 2011), and cultural services (Knoll et al., 2019). While the functioning is different between frozen and open water, few global studies have measured the timing and duration of these transitions (Klein et al., 2017; Xiao Yang et al., 2020), and there is no global data mapping this transition at medium to high resolution and no monthly area estimates of inland surface water and ice dynamics. Measuring these dynamics will enable a

better understanding of the current state and the ongoing and future impacts of climate change.

Several products map water dynamics at global scale, most notably Pekel et al. (2016) and Pickens et al. (2020), which provide dense time-series analysis of 30m Landsat multispectral data. Both of these studies primarily evaluated inter-annual open water extent dynamics, ignoring ice cover, but also mapped seasonal water cover. The only global area estimates that align with international reporting standards by providing uncertainty bounds are those by Pickens et al. (2020), producing area estimates of permanent water, five inter-annual change types, and stable seasonal water. However, this estimate of stable seasonal water was only a measure of the area with a mean annual occurrence percent of 10-90% of the ice-free period and inter-annual variability less than 50%, and did not provide estimates of the seasonal distribution of open surface water. Additionally, both of these studies ignored the frozen portion of the year with Pickens et al. (2020) removing snow and ice observations from the time series on a per-pixel basis and Pekel et al. (2016) excluding all data from the northern winter down to 30°N for December.

There are other studies that more closely examine seasonality, but lack either area estimates or global coverage. Klein et al. (2017) map seasonality globally as a percent of the entire year with 250m MODIS data, but do not provide area estimates or global seasonal distributions. Che et al. (2019) provided regional scale area estimates of the seasonal water cover of central Asia with associated uncertainty through a Landsat-based combined mapping and sampling approach.

The Sentinel-2 mission provides an additional public data source that is suitable for water monitoring moving forward. Sentinel-2A was launched in June 2015 and Sentinel-2B in March 2017 and full acquisition began in April 2017. While this limits its use for historical studies, it is better equipped than Landsat to evaluate seasonality in recent years due to its 5-day revisit interval at the equator and with much greater frequency toward the poles. Due to the increasing swath overlap of its orbits, twice as many unique observations are collected for every point at 56°N, 3x more at 67°N, 4x more at 72°N, and everywhere above 75°N is imaged daily during the period of the year with daylight at the time of overpass (mean local solar time of 10:30am). Visible and near-infrared bands are collected at 10m resolution with other bands collected at 20m and 60m. Given that the normalized difference ratio of NIR and green has been shown to be so effective for mapping surface water (McFeeters, 1996; Pickens et al., 2020; Tulbure et al., 2016), this dataset provides an opportunity to better capture small water bodies and to further explore the question of scale and heterogeneity of open surface water. While there are some national and subnational Sentinel-2 surface water dynamics studies (Carlson et al., 2020; Wieland and Martinis, 2020; Xiucheng Yang et al., 2020), there are no existing Sentinel-2 global products of any kind and no global surface water studies that have utilized this dataset.

In this study, we present the first global area assessment of seasonal inland open surface water dynamics together with the timing and duration of ice cover over water bodies through a combined mapping and sampling approach. Utilizing the water maps of Pickens et al. (2020) and a probability-based sample, we estimate the

area and associated uncertainties of open surface water and water body ice cover per month and as a fraction of the year according to good practice guidelines (Olofsson et al. 2014) and provide preliminary global 30m maps of ice cover.

4.2 Methods

To estimate the seasonal distribution of the global area of open surface water for 2019, a time-series of reference data was derived from visual interpretation of 10m Sentinel-2 and 3m PlanetScope imagery within a stratified, random, one-stage cluster sample. In parallel, we created a monthly time series of water percent and ice cover from the 2019 water layers of Pickens et al. (2020) and the GLAD Analysis Ready Data (Potapov et al. 2020) to provide the associated spatial distribution of seasonal and permanent surface water. The reference data set was also used to evaluate the monthly and annual performance of these layers.

4.2.1 Sample-based assessment

A total of 99,727 10m pixels were evaluated in a stratified, random, one-stage cluster sample of reference data to assess accuracy and to enable area estimation according to good practice guidelines (Olofsson et al., 2014). The mean of the 2017-2019 annual percent water layers from Pickens et al. (2020) was used as the stratifying layer (Figure 4.1). Although only 2019 is assessed in the reference data, a three-year period was chosen in order to include areas of seasonal water that may have had low observation density or low water presence in 2019. Three strata were selected: stable water presence ($\geq 90\%$), seasonal water presence ($< 90\%$ and $> 5\%$), and stable land ($\leq 5\%$). This strata map was projected into a 30m map per UTM zone

that aligns with the native Sentinel-2 data, resulting in an equal area population of clusters corresponding to all continental 30m grid cells. Each 30m grid cell represents a cluster of nine 10m Sentinel-2 pixels.

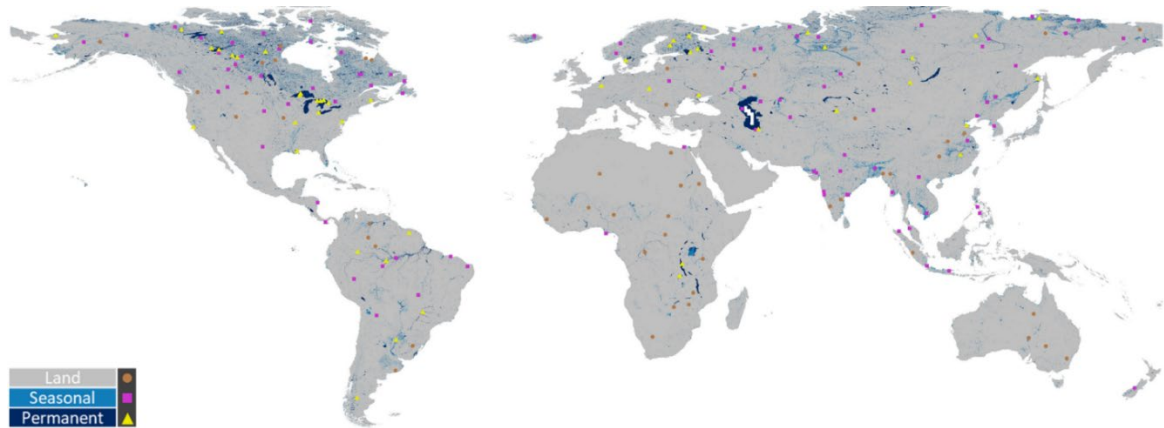


Figure 4.1: Stratification represented in geographic projection.

Fifty clusters were selected for each of the stable strata and 100 clusters for the seasonal stratum. Clusters were selected through first selecting a random point on the Earth's surface according to the method described in Hansen et al. (2020), checking what stratum that point belongs to within the corresponding UTM zone map, and adding it to the final sample set if the desired number of samples had not yet been reached in that stratum. All overlapping 2019 Sentinel-2 images were interpreted for each selected cluster, with a median of 110 dates per cluster. For each image, the nine sampled pixels were manually labelled land, water, cloud, haze, shadow, snow/ice, or bad (indistinguishable cloud, snow, or shadow or a corrupted image) through visual interpretation. For clusters with a mix of land and water in a single observation, 3m PlanetScope data was referenced to more accurately assign a

majority label to each 10m pixel. Ice, cloud, haze, and shadow were all labeled at the cluster level. Months with no images available that had a preceding and following calendar month with ice identified were labeled ice in the time-series. Due to the full systematic acquisition of Sentinel-2 imagery, the only areas and months with no images available are during the dark winter months of high latitudes when the sun has not risen by the time of the satellite overpass. Figure 4.2 shows the Sentinel-2 and PlanetScope data evaluated for one of the clusters.

The result is a dense time-series of water, land, and ice labels with a median of 44.5 clear observations. From this we calculated percent water for each month as the number of water labels divided by the sum of all clear observations. Annual percent water was derived as the mean percent water of all the months with data. Clear observations were defined in two different ways: by only land and water observations, and by land, water, and ice observations. The former provides the percent of the period in which open surface water can be observed (the ice-free period), and the latter the absolute percent of the year that open surface water exists. In the latter case, an ice time-series was derived from the reference data with all months with ice in $\geq 50\%$ of clear observations. A total of 186,435 10m observations were evaluated.

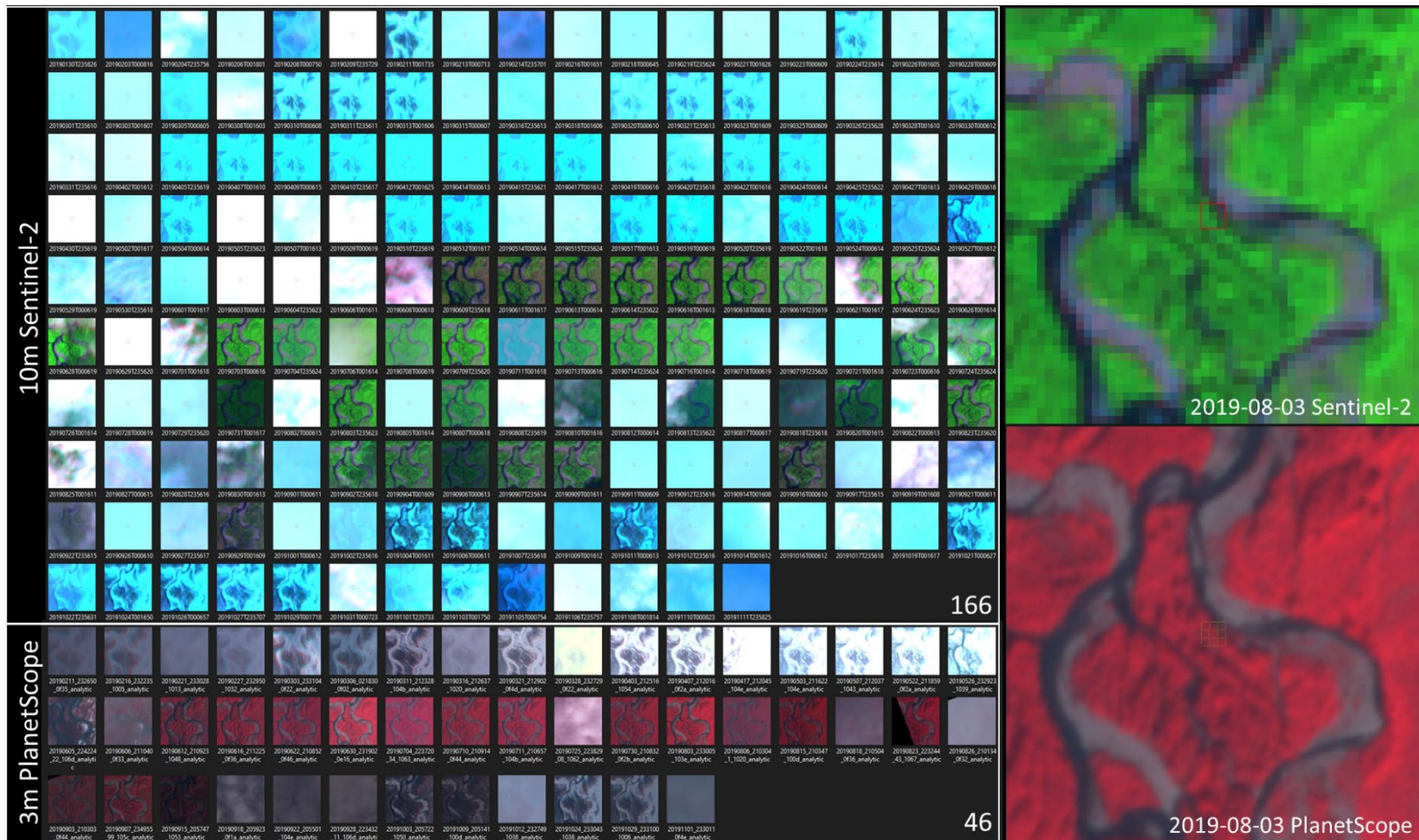


Figure 4.2: Example of Sentinel-2 and PlanetScope data for a selected cluster of 10m sample pixels centered at 173.330511°W, 64.2007883°N. Since there is a mix of land and water in the 30m cluster, this sample was interpreted using the 3m Planet labs data. The 30m cluster is identified with a red outline in the Sentinel-2 image and the 10m pixels with a yellow outline in the PlanetScope image.

Areas were estimated according to standard stratified one-stage cluster protocol. To calculate the area of water per month, the reference monthly water percent was first thresholded at $\geq 50\%$ per month for each 10m pixel to form a binary reference classification; and to calculate the annual area for a given threshold T , the reference annual percent was thresholded at $\geq T\%$. This binary data of the 10m secondary sampling units within each cluster u (30m unit) was then summed and divided by the number of 10m pixels with data within the cluster to create the cluster variable y_u that equals the proportion of the cluster that was the target class. This proportion, y_u , then serves as the variable for estimating the area, \hat{A} , for the given threshold (adapted from equation (3) of Stehman (2014)):

$$\hat{A} = \sum_{h=1}^H \bar{y}_h A_h \quad (3)$$

where $\bar{y}_h = \sum_{u \in h} y_u / n_h$, and n_h is the number of sampled clusters in stratum h , and A_h is the area of stratum h . Since all the sub-units (10m pixels) from a cluster are included in one-stage cluster sampling, the variance estimator used to estimate the standard error (SE) is based only on the cluster level data, y_u :

$$SE(\hat{A}) = A \sqrt{\left(\frac{1}{N^2}\right) \sum_{h=1}^H N_h^2 \left(1 - \frac{n_h}{N_h}\right) \left(\frac{s_{yh}^2}{n_h}\right)} \quad (4)$$

where A is the total area of all strata and $s_{yh}^2 = \sum_{u \in h} (y_u - \bar{y}_h)^2 / (n_h - 1)$ (adapted from equations (25) and (26) of Stehman (2014)).

Reference data were also calculated at 30m resolution by assigning to each observation the value of the majority class of the 10m labels. If no class covered ≥ 5 of the nine 10m pixels, the observation was marked as no data. Areas were then

estimated from this data in the same manner, except, as there are no longer subpixel proportions, y_u is either 0 or 1 based on the threshold.

4.2.2 Landsat time-series

We combined the 2019 water layers of Pickens et al. (2020) with the ice and no data flags from the GLAD Analysis Ready Data (ARD) (Potapov et al., 2020a) to create a preliminary integrated global monthly dataset of water and ice extent, and used the reference data to evaluate the performance. The data of Pekel et al. (2016) are not suitable for this study as the northern winter is not mapped, with December mapped only $\leq 30^\circ\text{N}$. The 2019 water layers consist of monthly water percent and annual water percent calculated by the number of water observations divided by the sum of land and water observations. Pickens et al. (2020) filtered the input to the annual water percent by removing up to three outliers from permanent land or water and months with < 5 observations over the 20 years, while the individual month layers were left unfiltered. To create a more stable monthly dataset, we used this 2019 annual water percent to filter out these same anomalous water or land flags from the monthly water percent maps. Given that there is not an ice label embedded in this product, we combined it with the flags within the quality assurance layer of the 16-day Landsat GLAD ARD (Potapov et al., 2020a) to add ice cover to the time-series. Each 16-day interval was assigned to the month with the most days in common. There is an ice/snow flag in the ARD. However, images are not processed for the intervals and 1° tiles that had $> 50\%$ snow cover on the tile-scale based on the average 2001-2019 monthly snow cover from MODIS/Terra Snow Cover Monthly L3 Global 0.05Deg CMG, Version 6, (<https://nsidc.org/data/MOD10CM/versions/6>). Images are

processed where available for all other periods and locations. Thus, we converted the ARD time-series into a monthly labels of ice, other processed data, and no processed data. Since all available Landsat scenes were classified in Pickens et al. (2020), a no-data value in that dataset represents either no image was available that month or that there were only ice, cloud, haze, or shadow observations. These months with no land or water observations in the Pickens et al. (2020) data were labeled ice if there was ice flagged in the ARD dataset, or there was (1) no processed ARD data, (2) evidence of ice in the time-series by an ARD flag or by ≥ 3 months with no processed data for regions $\geq 40^\circ\text{N}$, and (3) an adjacent month that matches these criteria or was flagged as ice. The final monthly time-series consisted of the 0-100% water labels of Pickens et al. (2020) with the no-data months either labeled ice as inferred from the ARD or remaining as no-data.

Using this combined dataset, we mapped the percent of the entire year with open liquid water presence, the number of months with ice cover over areas of seasonal or permanent water, and the months of ice onset and melt. Months that were labeled ice in the time-series without an explicit ice flag in the ARD and that are adjacent to a month with land or water observations are given the additional label of shoulder month. While more often truly having ice presence, these shoulder months have the greatest amount of uncertainty, and accuracies are computed with and without these months.

Accuracies were estimated at 30 m for both the monthly water and ice maps and the annual water maps using a ratio estimator (Stehman, 2014). Since the reference data were converted to 30 m at the observation level, the reference data was

then assigned as “water” or “no water” and “ice” or “no ice” in the same manner as the 10 m data as described in Section 2.1.3. For the map data, months that were labeled ice in the time-series without an explicit ice label in the ARD and that were adjacent to a month with land or water observations are here referred to as shoulder ice months with no data. While more often actually having ice presence, these shoulder months have the greatest amount of uncertainty, and accuracies were computed both with them as ice and as no data. For each of these cases, the same rules as for the reference data were then used to attribute water in the monthly and annual map data. As ice was already “ice” or “no ice” in the monthly map data, no additional thresholding was necessary. For both user’s and producer’s accuracies, $y_u = 1$ if both the reference and map labels were of the target class for a 30 m cell u , otherwise, $y_u = 0$. For user’s accuracy, $x_u = 1$ if the map label of cell u was of the target class, else $x_u = 0$; for producer’s accuracy, $x_u = 1$ if the reference label of cell u was of the target class, else $x_u = 0$. User’s and producer’s accuracies were then computed according to equation (27) of Stehman (2014).

$$\hat{R} = \frac{\sum_{h=1}^H N_h \bar{y}_h}{\sum_{h=1}^H N_h \bar{x}_h} \quad (5)$$

where \bar{y}_h and \bar{x}_h were the stratum-specific sample means of y_u and x_u . The variance estimator used to estimate the standard error (SE) is:

$$SE(\hat{R}) = \sqrt{\left(\frac{1}{(\sum_{h=1}^H N_h \bar{x}_h)^2} \right) \sum_{h=1}^H N_h^2 \left(1 - \frac{n_h}{N_h} \right) \left(\frac{s_{y_h}^2 + \hat{R}^2 s_{x_h}^2 - 2\hat{R} s_{xyh}}{n_h} \right)} \quad (6)$$

where $s_{y_h}^2 = \sum_{u \in h} (y_u - \bar{y}_h)^2 / (n_h - 1)$; $s_{x_h}^2 = \sum_{u \in h} (x_u - \bar{x}_h)^2 / (n_h - 1)$; and

$s_{yh}^2 = \sum_{u \in h} (y_u - \bar{y}_h)(x_u - \bar{x}_h)/(n_h - 1)$ (equations (26), (28), and (29) of Stehman (2014)).

To assess the accuracies of all the monthly maps combined, we again employ a one-stage cluster. However, instead of a spatial cluster of 10 m cells, the 30 m cell of each month becomes a secondary sampling unit and all months together form a temporal cluster. In this case, y_u equals the number of months with target class agreement for cluster u . For user's accuracy, x_u equals the number of months where the map label was of the target class for cluster u ; for producer's accuracy, x_u equals the number of months where the reference label was of the target class for cluster u . Accuracies and associated standard errors were then estimated with the same formulas as for an individual month, here termed aggregate user's and aggregate producer's accuracies.

4.3 Results

4.3.1 Area estimates

Almost two-thirds of the area of permanent water (defined as areas never having land) freezes over in the winter months for 2019, and truly permanent, year-round open water only comprises 23% of total area with open water presence (Fig. 4.3). June has the largest area of open surface water with 3.91 (± 0.19) million km² as well as the largest area of seasonal water that freezes (0.42 (± 0.11) million km²), reflecting the high flows and high water table after the spring melt of the northern hemisphere. January has the smallest area of open water with only 1.60 (± 0.21) million km². While 1.76 (± 0.19) million km² have seasonal water presence at some

point in the year, the largest monthly area of seasonal water is only 1.00 (± 0.17) million km² in June. However, April proportionately has the most seasonal water with 70% of water being permanent and October has proportionately the most permanent water (83%). Of regions that do not freeze, it is evenly split between permanent water (51%) and the total area of temporary water presence (49%), but for any given month, permanent water is 62% (July) – 79% (January) of existing open surface water that does not freeze. February has the largest area of ice cover over water bodies with 1.90 (± 0.22) million km² over stable water and 0.59 (± 0.13) million km² over regions with temporary water (2.49 (± 0.25) million km² total) (Fig. 4.4).

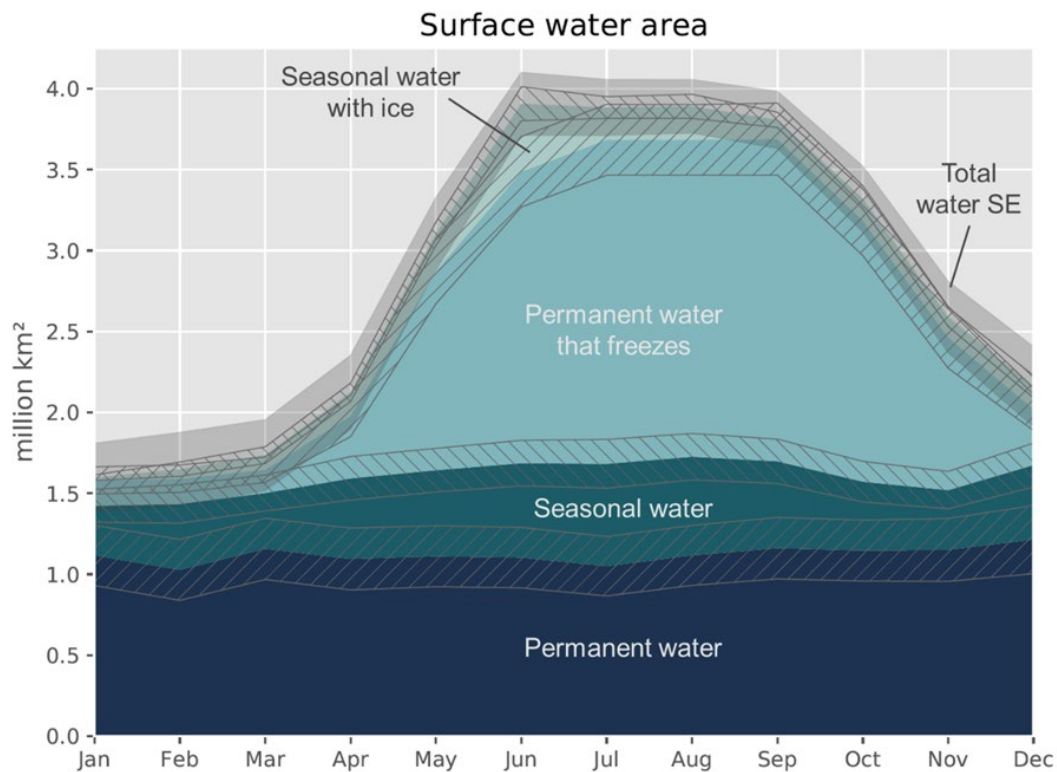


Figure 4.3: Area of open surface water surface water per month (km²). The regions with diagonal lines represent +/- one standard error (SE) of the single class total beneath it. The uncertainty associated with the total area of water per month is represented by +/- one SE.

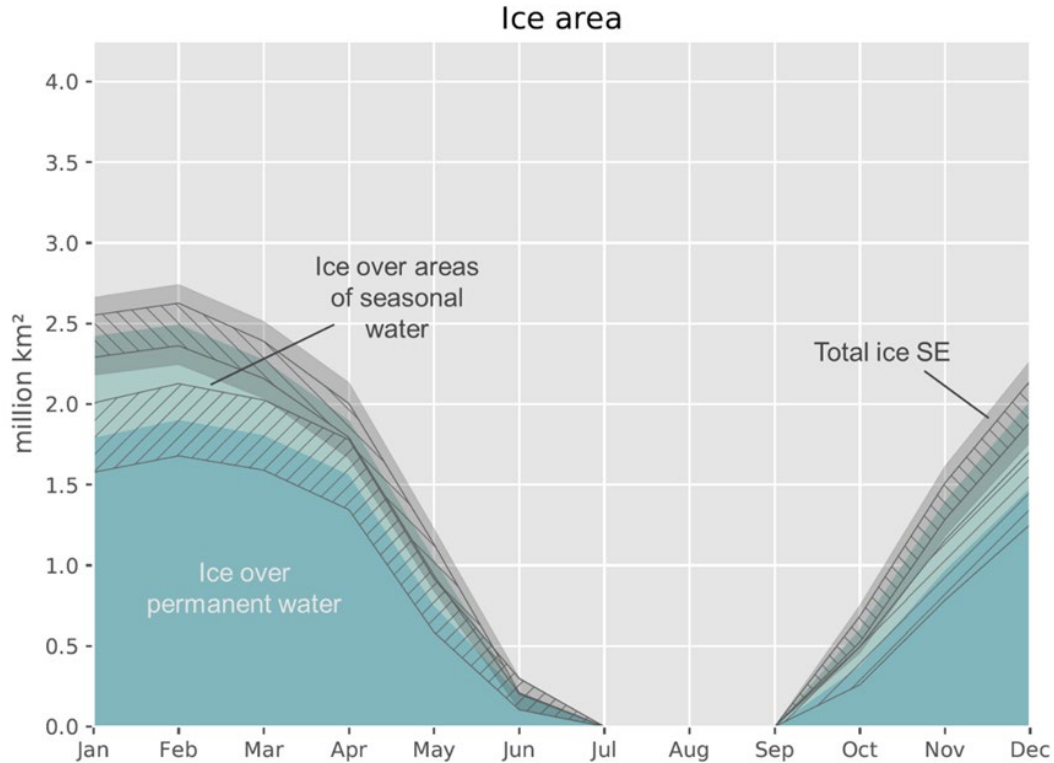


Figure 4.4: Area of ice cover per month (km²) over permanent water bodies and areas that had seasonal water presence. The regions with diagonal lines represent +/- one standard error (SE) of the single class total beneath it. The uncertainty associated with the total area of ice per month is represented by +/- one SE.

The sample-based estimates show the month with the largest area of melt of ice over permanent water bodies is May, and the month with the largest area of freeze onset is November (Fig. 4.4). Using the Landsat time-series for 2019, we mapped the month of melt and of ice onset for all permanent water bodies and found the month with the largest area of melt is June (24% of total melt area), followed by May (23% of total melt area), and the month with the largest area of ice onset was also November with 45% of the total area of ice onset. The mean month of melt and of freeze can be seen at 1° scale in Figure 4.5.

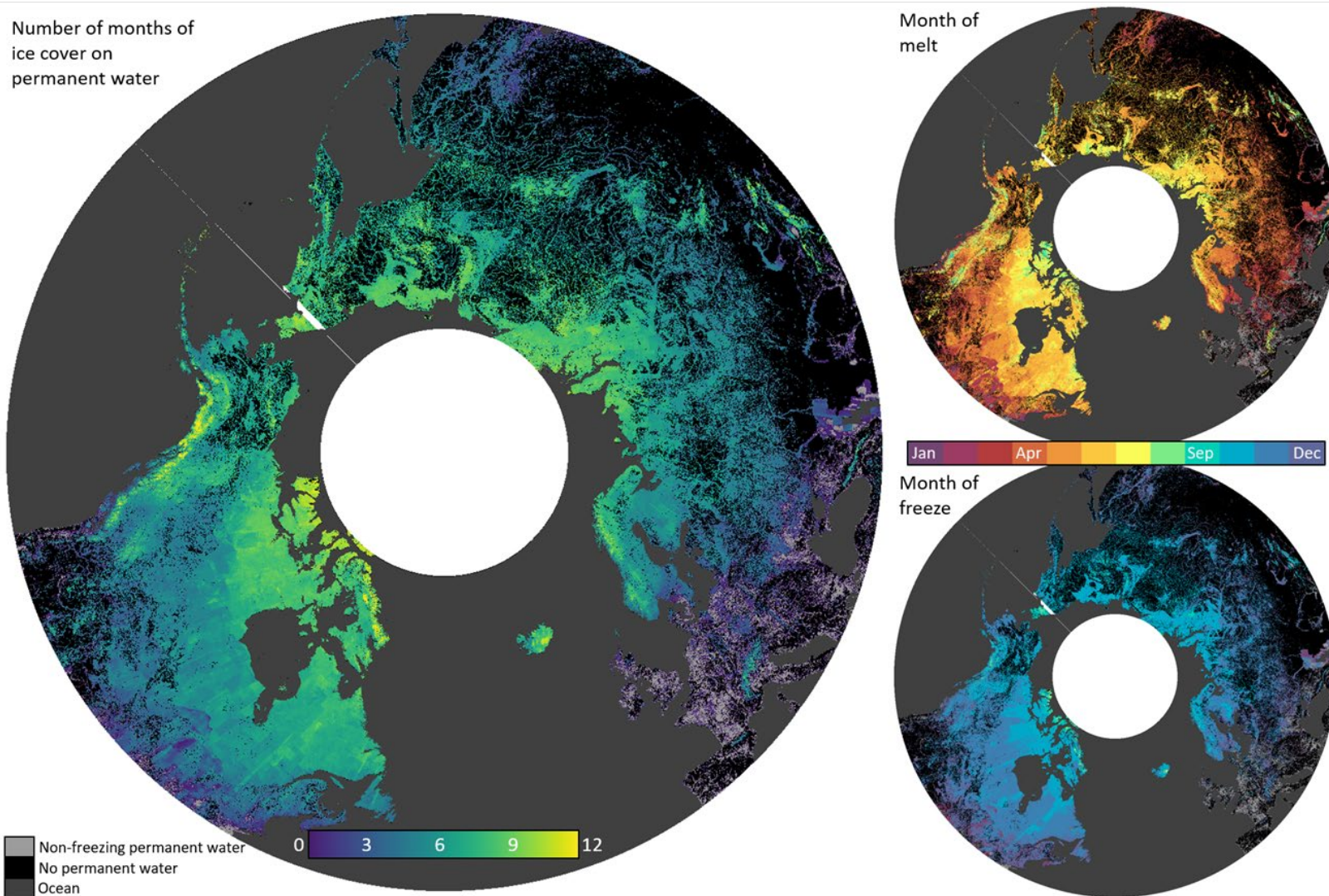


Figure 4.5: Number of months with ice cover, month of ice melt, and month of freeze for permanent water bodies $\geq 40^\circ\text{N}$ aggregated to roughly 5km resolution.

4.3.2 Accuracy

The monthly maps of Pickens et al. (2020) had aggregate user's and producer's accuracies of 92 (± 2)% and 89 (± 2)%, respectively, with no seasonal bias, in the case of ice being treated as no-data as it was by Pickens et al. (2020). When ice is considered valid non-water data (in either the reference or map), there are aggregate user's and producer's accuracies of 89 (± 2)% and 83 (± 2)%, respectively. Here the northern winter months have lower accuracies, particularly more omission (Fig. 4.6). If we refine the time-series so that the shoulder months without ice explicitly identified are labeled instead no-data as ice melt or onset may or may not have happened in that month, there is a reduction of omission errors with aggregate user's and producer's accuracies of 89 (± 2)% and 86 (± 2)% with the primary improvement within October and November. These omissions in the shoulder months are cases where there was no data in the Landsat time-series directly between months of ice and water/land and thus labeled ice, but there was water identified in the reference data of that month. However, there is still lower accuracy within the months with greater ice presence.

On the annual scale, the shoulder months with no data in the GLAD ARD and Pickens et al. (2020) also play a significant role in defining the accuracies as shown in the comparison of the two sets in Figure 4.7. Omission is much higher than commission in both sets, but when the shoulder months are defined as no-data, this gap shrinks. The precision of the percent of the year values is also a function of the number of clear observations and of clear months. The Landsat record had a median of 14 clear water and land observations during 2019 for the sample locations,

whereas, the Sentinel-2 reference data had a median of 35 clear water and land observations and the Planet reference data had a median of 40.

Monthly ice had aggregate user's and producer's accuracies of 85 (± 2)% and 88 (± 2)% when shoulder months with no data were treated as ice. If the shoulder months are treated as no-data, the accuracies go up to 93 (± 2)% and 87 (± 2)%, respectively. Accuracies were highest for January-April, and lowest for June and October, however, these latter months contribute little to the aggregate accuracies because of the small area of ice cover.

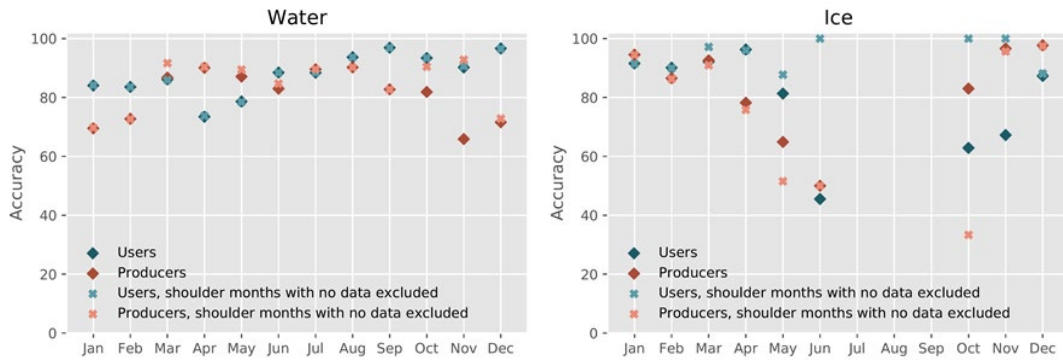


Figure 4.6: Accuracy of monthly water and ice maps.

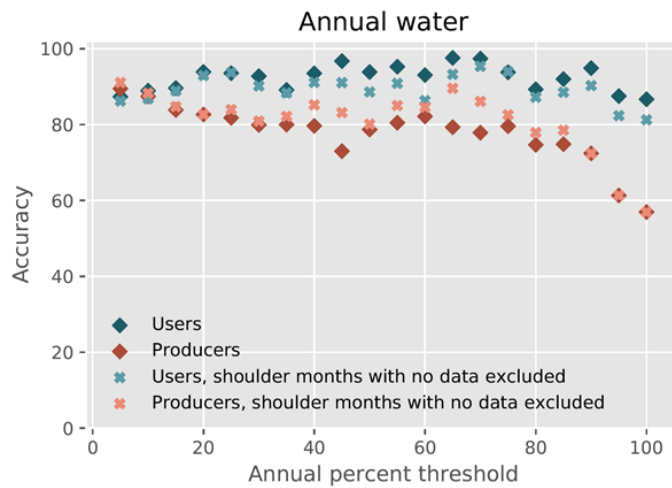


Figure 4.7: Accuracy of binary maps of water presence $\geq X\%$ of the year.

4.3.3 10m vs 30m reference data area estimates

Monthly water area computed with 30m reference data was very similar to when computed with 10m reference data, resulting in a median monthly area estimates of 0.3% larger and a range of 1.7% smaller to 3.3% larger. The standard errors were uniformly larger when computed at 30m with a median increase of 4.1% and a maximum increase of 12.8%. Very similar results were found at the annual scale with area estimates ranging from 1.8% smaller to 3.0% larger and a median increase of 0.2%, and standard errors all larger with a range of 1.1% - 12.4%. Thus, while assessing the reference data at 10m does not change the area estimates in a uniform way, with either more or less water detected, these estimates have greater precision and can be assumed to then provide better estimates. In both the monthly and annual sets, the 30m SEs had the largest percent increases when the estimated area was larger, e.g. the northern summer and low annual percent.

Based on 5m RapidEye imagery, Pickens et al. (2020) found that 10.9 (± 1.9)% of global inland surface water is within mixed pixels at Landsat scale. Using the same dataset, we estimate 3.3 (± 0.6)% of global inland is within pixels with <50% water cover at Landsat scale and should be excluded based on our mapping definition, and 7.6 (± 1.3)% is within pixels with $\geq 50\%$ and <100% water cover and will be more difficult to map accurately. The percent of change calculated in the 10m and 30m estimates provide an empirical example of the effect of this, and all 30m estimates for this study are within 3.3% of their 10m counterparts and have a mean absolute difference of 1.0% for the monthly and 0.9% for the annual estimates. However, these 10m estimates presented here may not represent the full area of fine-scale water

features since much of this will be just a minute fraction within the land stratum, but the 5m RapidEye sample should account for most of the surface water down to that resolution because of the utilization of 20x20km reference maps and the degree of co-location at that scale. Thus, while there are gains from the 10m, it will be application specific whether this greater degree of precision is needed.

4.4 Discussion

4.4.1 Water and ice dynamics

The World Meteorological Organization (WMO) identified lake area and lake ice extent as essential climate variables (ECV) in 2006, and further refined this in 2008 by specifying daily resolution and 20m and 300m spatial resolution respectively. While we still have not met this benchmark, our results are the first global estimates of seasonal water and water ice extent broken down by month and by percent of the year. Given that over half of the world's inland surface water freezes over during the northern winter, the estimates of permanent water derived from only the ice-free portion, as has been done previously (Pekel et al., 2016; Pickens et al., 2020), will be more than double the area with open surface water for all twelve months (Fig. 4.8). As indicated by the WMO, it is important to distinguish between frozen and liquid surface water because the ecosystem services provided by the two states are vastly different with changing habitats (Vincent et al., 2011), transportation networks (Stephenson et al., 2011), and climate factors such as albedo and emission rates (Wik et al., 2016).

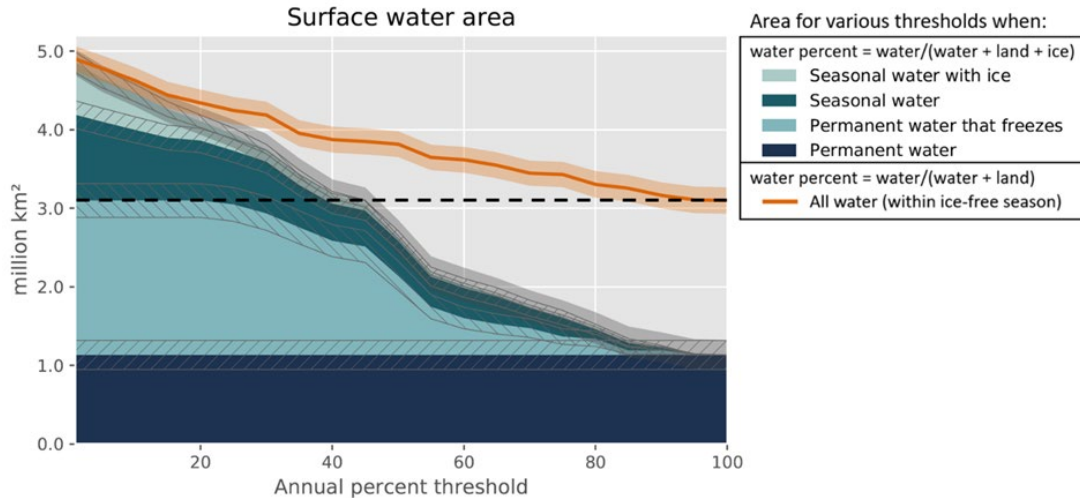


Figure 4.8: Comparison of the area estimates of annual water extent for varying temporal percent thresholds for two different annual aggregation methods. The stacked area graph represents the extent of open liquid water present $\geq X\%$ of the entire year. The orange line represents the extent of water present $\geq X\%$ of the portion of the year without ice (ice is considered no-data), with the area estimate of 100% water equal to the combined area of permanent liquid water and permanent water that freezes. There is a widening difference between the two estimates, such that the previous practice of ignoring ice results in an estimate of 100% water that is 2.5x larger than the area of permanent liquid water.

Ice is the dominant driver of the seasonality of global water area (Fig. 4.3).

However, ice cover phenology can differ on the scale of months among neighboring water bodies of varying size and type, as shown in Figure 9. Several previous estimates of ice phenology have been modeled by temperature constraints such as the 0°C isotherm model of Brooks et al. (2013), however these will have bias among different water body sizes and types. A recent study by Xiao Yang et al. (2020) mapped the seasonality of river ice at the Landsat scene scale and developed an empirically based model from the prior 30 day mean Surface Air Temperature (SAT). This provides greater accuracy not only because of the more accurate temperature effect monitoring, but also due to the restriction of only rivers with width $\geq 90\text{m}$. A global 30m, or even better, 10m dataset will enable an analysis of the differential

behavior of rivers and lakes of various scales, which could be modeled with climate data to have better indications of future change. There is already a documented increase in the ice-free season (Šmejkalová et al., 2016; Xiao Yang et al., 2020) with projections estimating a 15-50 day increase by late century (Dibike et al., 2011; Prowse et al., 2011). Wik et al. (2016) estimated that a 20-day increase would cause an 24-50% increase in methane emissions from lakes above 50°N. However, they also found high variability in emissions between water body types. High spatial and temporal resolution maps of water and ice extent and change together with water body typologies could greatly improve these estimates and our understanding of climate interdependencies.

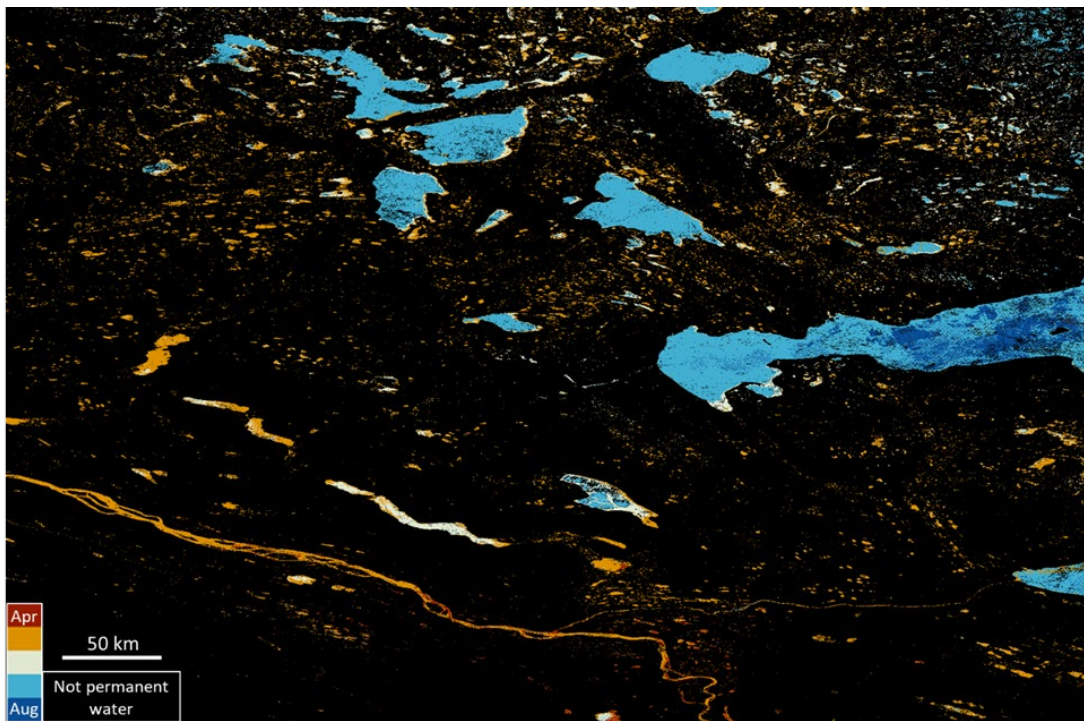


Figure 4.9: Landsat derived month of ice melt over permanent water bodies for 2019 with many small lakes melting two months earlier than the large lakes. Centered on 125.5°W, 66.0°N.

The Landsat derived maps of ice dynamics presented here provide a proof of concept for further mapping efforts (Fig. 4.5, Fig. 4.9). Given that some of the ice

labels are inferred from data availability and the MODIS snow cover product rather than being mapped directly, there is the most uncertainty for shoulder months without an explicit snow identification. Water ice phenology and land snow phenology can be significantly different. Ice is dependent on longer temperature patterns and on the latent heat of the water bodies. Snow is precipitation dependent and can come very quickly after below freezing temperatures or be delayed. The depth of the snowpack affects how soon the snow melts, but often there is a greater lag for water body ice thaw. Due to this potential temporal mismatch in ice and snow phenology and how our time-series is derived together with better imagery during the melt season due to higher sun angles, we are more likely to directly map ice in the thaw season rather than freeze season, as can be seen in the greater precision of the month of melt compared to the month of freeze in Figure 4.5. Additionally, due to not having a count of ice observations in a month, if there was water or land presence the month was labeled with the corresponding water percent value. Despite the ambiguity of labeling ice in the Landsat time-series, the maps have reasonable accuracies with aggregate monthly water user's and producer's accuracies of 88% and 83%, and aggregate monthly ice user's and producer's accuracies of 85% and 88%, respectively. These maps could be improved if ice was directly classified from the Landsat imagery, and the timing could be further improved by utilizing Sentinel-2 imagery.

However, both the water and the ice area estimates at the monthly and annual time scales are derived solely from the interpreted Sentinel-2 and PlanetScope

reference data. This means that any ambiguity in labeling the Landsat time-series does not affect these estimates.

4.4.2 Seasonal surface water

Seasonal waters are also significant, encompassing 16-28% of open surface water for any given month. Seasonal water is defined as locations with land and water presence during the year. Considering the entire year, 1.76 (± 0.19) million km² had seasonal waters at some time. This is over double the estimate of Pekel et al. (2016) for October 2014-October 2015. Pekel et al. (2016) defined seasonal water as at least one month not having water, which results in a minimum threshold of 8% of the year. Here we found that the area with seasonal water $\geq 10\%$ of the year totaled 1.37 (± 0.18) million km², 69% larger than the estimate of Pekel et al. (2016), though this does not exclude seasonal water that only is land for less than a month. Additionally, it is significantly larger than the area of stable seasonal water reported by Pickens et al. (2020), but that estimate only accounted for areas with inter-annual variability of half a year or less, and many areas of seasonal water can have significant year to year variation. Most seasonal waters are found in natural wetlands, floodplains, or crop or mineral extraction land use.

In a synthesis of over 320 case studies, de Groot et al. (2012) estimated the yearly value per hectare of coastal wetlands at \$193,845 and of inland wetlands at \$25,682, five times more than any other non-coastal terrestrial environment, followed by tropical forest valued at \$5,264. Rivers and lakes are estimated the next most valuable at \$4,267, though in a similar study by Costanza et al. (2014) rivers and lakes were valued instead at \$12,512 with other ecosystem values remaining

approximately the same. While these are not intended to be market prices, they connote the value of the ecosystem service benefits. Regulating services, particularly of waste treatment, regulation of water flows, and disturbance moderation, rank as the most valuable ecosystem services of wetland systems along with providing habitat for biodiversity.

Floodplain inundation is critical to the ecological integrity of river ecosystems (Poff et al., 1997). However, almost half of our river systems are moderately to severely fragmented by human-built impediments (Grill et al., 2015). While for some rivers, much of the inundation will be under vegetation cover, and thus invisible from above, for other rivers, such as the Ob, Parana, or Zambezi, this critical inundation can be monitored (Pickens et al. 2020, Pekel et al. 2016). Monitoring is of particular use to evaluate the impact of flow-altering dams and levees either built during the monitoring period or under changed management practices.

4.4.3 Future monitoring

Landsat may provide sufficient data to evaluate changes in inland surface water ice presence and timing over the last 20 years. While the monthly water and ice areas summed from the monthly Landsat maps have a similar general pattern and magnitude as the sample-based area estimates, there are also significant differences on the month level (Fig. 4.10). The area estimates derived from the 30m reference data were all within 3% of the 10m area estimates, indicating that if ice and water are properly labeled the dynamics could be derived directly from Landsat data. Before 1999 there was not a systematic global acquisition of scenes, resulting in long data gaps and some regions such as Siberia not being imaged until 1999 (Pekel et al.,

2016; Wulder et al., 2016), prohibiting long-term analyses. Since this study benefited from the higher acquisition rates since the launch of Landsat 8 in 2013, wall-to-wall mapping of the ice phenology of 1999-2012 will be more limited, and in all cases, areas should be estimated with a statistical sample.

The increased temporal resolution of the Sentinel-2 mission enables near-daily monitoring of the high latitudes. We found that there were 2.5 times more clear land and water observations in the Sentinel-2 times-series compared to Landsat for the reference samples. Together with the 10m spatial resolution of the visible and near infrared bands, this offers the potential to meet the ECV standards of the WMO for 2017 forward. The temporal domain would be further enhanced by the integration of Landsat and Sentinel-2 observations. Such a capability would enable a 3-5 day revisit interval for the tropics and increase the probability of capturing cloud-free observations of short duration flood events while providing precise quantification of seasonal hydroperiods. Additionally, while the area estimates derived from the 30m reference data are very close to those obtained with the 10m reference data, the full scale of water bodies smaller than 30m is not yet quantified due to the stratification and sampling strategy and the small fraction of the land surface they cover. With global Sentinel-2 time-series maps of surface water presence at 10m, we could further answer how much has remained unmapped and with greater accuracy map small water bodies. This is particularly valuable given the outsized importance of small water bodies for biodiversity, water regulation, and geochemical cycles (Biggs et al., 2017; Downing, 2006).

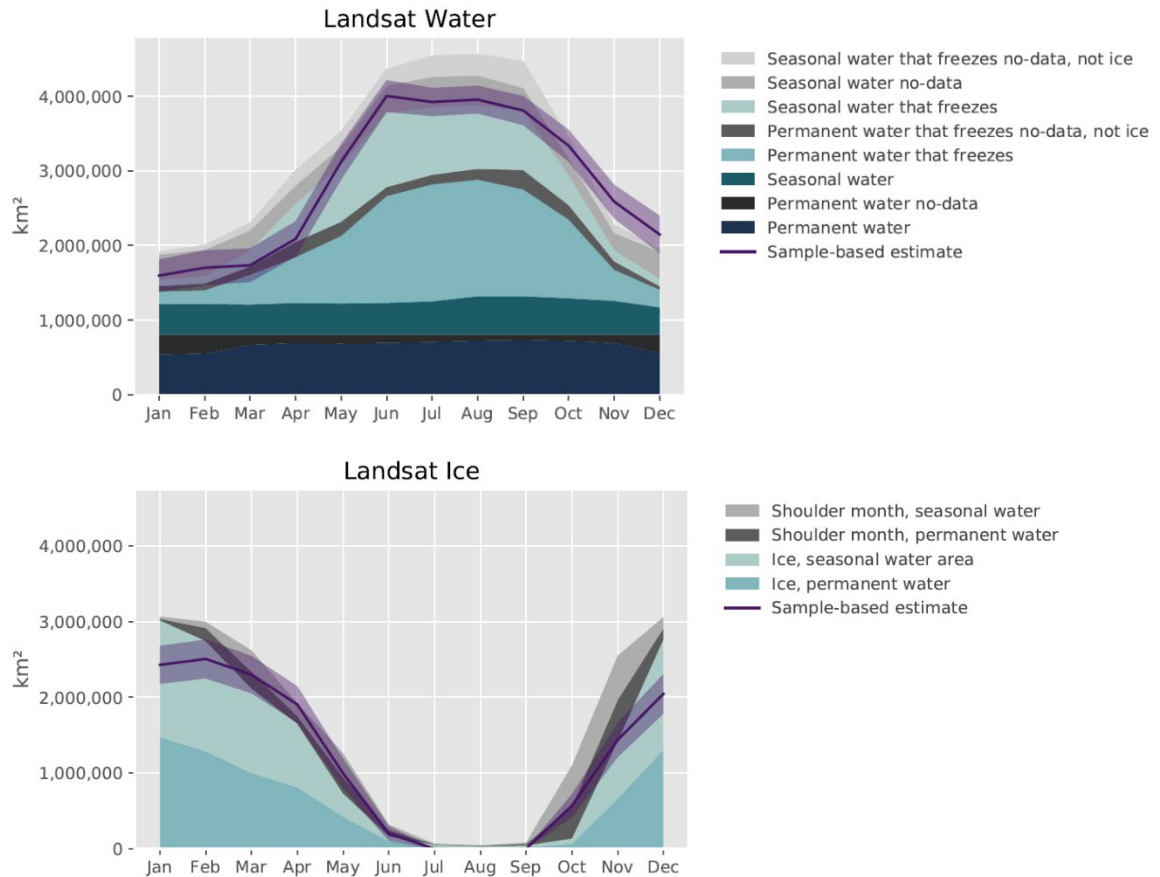


Figure 4.10: Map based areas from the Landsat time series. Area of no data for permanent water classes is most likely water, however, in the seasonal water classes, the no-data months could be water or land.

4.5 Conclusion

Global hydrology is constantly in flux. The global area of surface water in June is 2.5 times that of January. While $4.86 (\pm 0.16)$ million km^2 had water at some point during 2019, only $1.13 (\pm 0.19)$ million km^2 was truly permanent without freezing. The rest experienced either a water-land or water-ice transition, with all such changes impacting climate and ecosystem functioning. Significant progress has been made mapping interannual change (Pekel et al., 2016, Pickens et al., 2020), but the results presented here are the first global estimates of monthly water and surface

water ice presence with associated uncertainties. Landsat offers possibilities to evaluate changes in the timing of ice onset and melt over the past 20 years, and since 2017, Sentinel-2 has offered unprecedented monitoring potential with 10m spatial resolution and a 5-day revisit rate at the equator and near-daily in the boreal. As we continue to modify the surface of the earth and the climate continues to change, improved quantification of inland surface water and ice change will provide insights into the impacts and feedbacks of climate and weather, and of land cover and land use change.

Chapter 5: Conclusion

5.1 Summary of contributions

This dissertation presents the first set of area estimates for global open surface water extent and inter-annual and seasonal change that follow good practice guidance for area reporting (Eggleston et al., 2006; Olofsson et al., 2014; Penman et al., 2016; Stehman, 2013). The results are also the first that employ all Landsat imagery for the entire study period. Seven types of inter-annual dynamics were mapped and estimated globally: permanent, stable seasonal, loss, gain, wet period, dry period, and ≥ 3 transitions between water and land (Ch. 3). Sample-based area estimates showed that of the area with water at some point from 1999 to 2018, only 60.82 (± 1.93)% was permanent, totaling 2.93 (± 0.09) million km². Unidirectional loss and gain represented a small portion with 1.10 (± 0.23)% and 2.87 (± 0.58)%, respectively. The area that transitioned multiple times between land and water inter-annually was more than 4x larger, accounting for 19.74 (± 2.16)% of total water area and totaling 0.95 (± 0.10) million km². This establishes the necessity to evaluate time-series data through the entire period to report trends of loss or gain as well as other dynamics. Much of the area of multiple transitions is seasonal water in any given year, and stable seasonal comprised an additional 15.69 (± 2.07)% of 1999-2018 water area, defined as places with mean annual water presence 10-90% of a year and interannual variation $< 50\%$. Together, these seasonal waters are found primarily in floodplains and other natural wetlands, or in human land uses such as for rice cultivation or mineral extraction.

Providing a more in-depth investigation into the dynamics of seasonal waters, area estimates of the monthly distribution of surface water and ice were derived according to good practice guidelines for 2019 using a multi-sensor approach combining Landsat, Sentinel-2, and PlanetScope imagery together with elevation data (Ch. 4). This analysis is the first global study to combine water and ice dynamics at $\leq 30\text{m}$ resolution. Results show that 63% of the area of permanent water, defined as areas with continuous water or ice cover, have ice cover for some duration. Correspondingly, June had the largest area of water with $3.91 (\pm 0.19)$ million km^2 and January had the least with $1.59 (\pm 0.21)$ million km^2 due to the vast amount of surface water in the high-latitude northern hemisphere. $1.76 (\pm 0.19)$ million km^2 had seasonal water presence defined as having both water and land in the time-series. February had the maximum ice extent over permanent and seasonal waters with a total of $2.53 (\pm 0.24)$ million km^2 . To derive these estimates, 2017-2019 Landsat annual water percent layers from Chapter 3 were used to stratify 30m grid-cells into land, permanent water, and seasonal water and each 30m grid-cell was subdivided into nine 10m pixels. All 2019 Sentinel-2 images were evaluated and labeled per sampled pixel; if there was both water and land presence within the sample unit for any date, 3m data for every 5 days was obtained from PlanetScope and labeled. This enabled a subpixel accuracy assessment of the 2019 monthly Landsat water percent maps. Additionally, this study showed the potential advantages of using Sentinel-2 data, with its 10m spatial resolution and, more importantly, offering 2.5 times more clear observations through the year than the Landsat 7 and 8 time-series. In the boreal,

Sentinel-2 offers near-daily observations with weekly clear observations, enabling high spatial and temporal mapping of the freeze and thaw dynamics of ice cover.

Undergirding these analyses of the Landsat time-series, Chapter 2 showed the accuracy of mapping water with the employed detection method at the month scale at 5m resolution, with user's and producer's accuracies of 97.5 (± 0.7)% and 97.7 (± 0.7)%, respectively. The 5m reference maps of open surface water from classified RapidEye imagery enable estimation of accuracy as a function of distance from the closest water-land boundary. This product was shown to have 96.9 (± 0.9)% user's accuracy and 99.0 (± 0.3)% producer's accuracy for pixels >30m from a boundary and 70.9 (± 1.6)% user's accuracy and 66.0 (± 3.7)% producers accuracy for pixels within the 30m of the land-water boundary. Handling of these mixed pixels is important as 10.9 (± 1.9)% of global inland water is within mixed pixels at Landsat resolution, as estimated with the 5m reference data.

Together, this dissertation provides the most temporally dense area estimates of interannual and seasonal change at 30m resolution, and the maps produced in this study provide detailed visualizations of seasonal and inter-annual surface water dynamics using the entire Landsat archive from 1999 to 2020. These maps enable local and regional assessment of changes through the past 20 years and have many potential applications in ecological, LCLUC, and climate studies. The presented Landsat-based method will continue to be updated, with the current monthly, annual, and interannual map products available through 2020, and is available for download at www.glad.umd.edu/dataset/global-surface-water-dynamics.

5.2 Potential improvements and outstanding issues

While high accuracies are obtained at the monthly scale, change was shown to be difficult to map, with much lower accuracies. This is due in part to not only having to accurately identify water and land, but also the timing and duration of changes of state of water or land. This is compounded by the fact that there are some land covers and water properties that are difficult to accurately map every time. There are classification issues with volcanic and other dark rock or debris-laden glacial flows labeled water, particularly if they coincide with cloud shadow. Very shallow waters or those with partial vegetation cover are sometimes classified as land. Mixed pixels are also a source of classification confusion. Due to this, persistent mixed pixels were often labeled as dynamic. Additionally, mixed pixels are inherent in change and many of the problematic classification cases are also present.

In both Chapters 3 and 4, the time-series samples employed enabled area estimates of stable and dynamic classes with associated uncertainty, but these global estimates could be improved and have greater precision with a larger sample allocation. Additionally, a greater allocation of samples could enable regional estimation of stable and change extents. This could be done within both studies through selecting additional sample locations within the existing sampling designs. For national or regional reporting of the extent and change of open surface water, additional sample locations could be selected and interpreted for just that region.

Through the process of evaluating the reference data for the seasonal assessment of Chapter 4, the importance of surface water ice became apparent. There is no ice flag embedded in the current set of maps, however, given that over half of

global surface water freezes over (Ch. 4), ice plays a critical role. In the classification that results in the water and land labels ice is also identified, but unfortunately, those labels were not saved. To visualize some of these dynamics in 2019, an ice label was retroactively given through a combined analysis with the GLAD Analysis Ready Data (ARD) Landsat (Potapov et al., 2020a). As shown in other studies (Prowse et al., 2011; Wik et al., 2016), there are differential rates of ice onset and melt between different types and sizes of water bodies. Thus, a 30m map of ice dynamics would provide valuable additional data for forecasting the interactions with climate. In addition to mapping ice, I should have also labeled ice as I interpreted the 1999-2018 time-series sample data. This would have illuminated the large impact of ice earlier and may have been able to show change or variability in ice patterns.

While I repeatedly use the term global throughout this dissertation, the geographical scope is 56°S – 75°N, excluding Greenland, as has been done in other studies (Hansen et al., 2013; Potapov et al., 2020b; Ying et al., 2017). While this does not affect estimates for some land covers such as tree cover, it does have a marginal effect on water estimates and a much larger effect of estimates of water ice due to water bodies north of 75°N being frozen nearly the entire year.

An additional caveat is that optical sensors such as the TM, ETM+, and OLI of Landsat and MSI of Sentinel-2 cannot penetrate through clouds or vegetation cover, thus preventing water from being mapped that is under these conditions. For this reason, the maps of this dissertation represent open surface water which is here defined as water on the ground surface that (1) is visible from above and not obscured by objects on or above the water surface, for example, forest, floating aquatic

vegetation, bridges, clouds, or ice and that (2) covers $\geq 50\%$ of a pixel. It is unknown how much surface water is left undetected due to persistent monsoonal cloud cover or under persistent vegetation canopy such as in forested wetlands of the Amazon.

5.3 Future research

Many more questions arising from these studies remain unanswered - How would 10m maps with ≤ 5 day revisit aid further studies? What are the differences in ice phenology between water body types? What are the trends in ice phenology? What is the extent and duration of storm event floods? How much surface water is under vegetation canopy? What are the trends in various water quality measures? How do water and ice extent and quality interact with climate? How do water extent and quality interact with land cover and land use change?

As has been discussed, Sentinel-2 offers an unprecedented opportunity to monitor open surface water from 2017 forward. There have been several regional time-series Sentinel-2 derived maps, but no global maps. While this dissertation has reduced the bounds of uncertainty, the question still remains how much additional water could be identified with a 10m map? Through classifying all the Sentinel-2 observations into water, land, ice, and cloud or shadow, the seasonality and extent of water and ice could be shown at the greatest detail to date, and finally give a well quantified answer to this question. The higher resolution of Sentinel-2 would also be helpful for water body type identification and for small rivers and streams to be shown with more continuity. As testified to in Chapter 4 and shown in other research (Prowse et al., 2011; Wik et al., 2016), there is different behavior of ice for different

types of water bodies based on various properties such as size, depth, and flow. Additionally water body size and type affect ecological functioning, geochemical cycling, and other ecosystem services (Biggs et al., 2017; Raymond et al., 2013; Wik et al., 2016; Woolnough et al., 2009).

As our climate continues to change, warming is particularly fast in the Arctic with lake ice projected to have a shorter season by 20 or more days by late century (Dibike et al., 2011; Prowse et al., 2011). There is a clear need to better document current ice phenology, to have a water body typology map, and to assess current and future ice dynamics. Chapter 4 showed the feasibility of monitoring water and ice with Landsat for the current period, but this can best be done with Sentinel-2 data for 2017 forward. However, of particular interest would also be to retrospectively map surface water ice using Landsat to establish trends in ice dynamics. The feasibility of this for given scales remains to be seen. Landsat provides the longest total period of observation, but there are low acquisition rates before 1999 and some of Siberia was not imaged until 1998. Additionally, there are less acquisitions before 2013 and the operation of Landsat 8. Thus, some ice maps and sample-based assessments will be able to be made, but they may not have the temporal density to inform trends at the per-pixel level across the Arctic. Data may instead be able to be aggregated across regions to assess trends. However, there have always been dense observations over the USA and this may provide an opportunity to assess trends in Alaska back to 1985 and make potential inferences for more of the Arctic. MODIS provides an additional data stream for 2000 forward, but the 250-1000m resolution of its bands limits it to larger water bodies. Given the relatively small scale of the shift in ice timing,

particularly relative to the revisit rate of Landsat, with estimates of the shift of freeze and break up in the Arctic over the last decades ranging from a shift of a day per year to a day per 8 years (Lopez et al., 2019; Prowse et al., 2011; Šmejkalová et al., 2016), a high degree of precision will be required, necessitating a larger volume of samples.

To expedite disaster response, it would be conducive to have near-real-time maps of flood extent resulting from large storms. However, typically there is concurrent prevailing cloud cover that prevents observation with Landsat or Sentinel-2 satellites. However, another ESA satellite mission, Sentinel-1, has C-band synthetic aperture radar (SAR) sensors which can penetrate clouds. Concurrent Sentinel-2 and Landsat observations could be used to train a global Sentinel-1 water detection model. Various regionally or locally derived models have been produced for flood extent monitoring (DeVries et al., 2020; Twele et al., 2016; Zhang et al., 2020). There are two Sentinel-1 satellites, together offering 6-day revisit data since 2016, with higher frequency toward the poles. Unfortunately, while the timing could line up between the satellite overpass and the maximum flood extent, in many cases, the overpass will not coincide and could be several days after when it would be useful. Two more Sentinel-1 satellites are planned, with Sentinel-1C scheduled for a 2022 launch. On the optical side, Landsat 9 is scheduled for a September 2021 launch, and there are also two more Sentinel-2 satellites planned. This will provide an optical sensor constellation of $\leq 30\text{m}$ resolution and near daily repeat. While Landsat and Sentinel-2 cannot see through the clouds, more observations provide more opportunities to image the land surface, and together with Sentinel-1 data will enable more accurate maps of flood extent in near-real time.

It is unknown how much surface water remains undetected due to forest canopy or other vegetation cover. While Sentinel-1 can record the ground surface through clouds, C-band SAR has limited penetration in forest canopies. L-band SAR has a greater capacity to penetrate vegetation, and inundation maps have been produced with it for the wet and dry seasons of the Amazon basin (Hess et al., 2015). However, while it may not be possible to map water under the canopy directly with C-band SAR, it may be possible to detect fluctuations within a delineated wetland extent. I am developing a wetland map using Landsat and topographical metrics indicating water accumulation (Bwangoy et al., 2010; Margono et al., 2014) with preliminary results contained in Hansen et al. (2021, submitted).

In addition to extent, water quality is a critical issue. Both climate and land use impact water quality (Tong and Chen, 2002; Whitehead et al., 2009), with current relationships modeled with in situ or remote sensing data from local and regional studies. Landsat has been employed to model water quality parameters, including total suspended solids (TSS), chlorophyll-*a*, and surface temperature, though due to the empirical nature of many of the algorithms, they are often applicable only to particular regions (Wulder et al., 2019). While, several regional Landsat time-series analyses of water quality exist (Dang et al., 2018; Heege et al., 2014; Olmanson et al., 2008), global assessments are needed to evaluate past impacts and future risks (UNEP, 2016). Water masks like those produced in this study provide a spatial target for developing water quality models and applying them through time. Within the Global Environment Monitoring System for Freshwater (GEMS/Water) program of the United Nations Environment Programme (UNEP), a global database of water

quality measurements containing data from 75 countries and 5,700 stations and totaling more than 7 million entries is publicly available and continues to be updated (<https://gemstat.org/>). With careful data cleaning, this dataset could be harnessed together with satellite data from Landsat and Sentinel-2 to develop reflectance-based models that could be applied globally and through time. In addition to the benefits of a global scale assessment, it could aid local water resource management, particularly in data poor regions.

5.4 Conclusion

Global hydrologic systems are continually in flux with increasing direct impacts from humanity and continuing future impacts from climate. Quantifying the dynamics of change in the past decades enables better understanding of impacts in the next decades. This dissertation provides a small piece of this task and provides insights into how to further do so. As our water resources become more strained in many parts of the world, new monitoring capacities and analyses of causes and effects will enable better management of water resources in balancing the needs of humankind and the maintenance of natural hydrologic systems.

Appendices

A.I Area estimation of water dynamics classes

Area was estimated for each of the eight classes of water dynamics as well as for aggregations of these classes with these reference data. For a given class, the global area W of that class is estimated by:

$$\widehat{W} = \sum_{h=1}^H \widehat{W}_h \quad (7)$$

where H is the number of strata. The estimated area of the class within stratum h is $\widehat{W}_h = A_h \widehat{p}_h$ where A_h is the area of stratum h and \widehat{p}_h is the sample proportion of pixels of that class within stratum h . The stratum area A_h is calculated by summing the areas of all pixels within the stratum. The estimated variance of a stratum-specific area estimate is:

$$\widehat{V}(\widehat{W}_h) = s_{h,u}^2/n_h \quad (8)$$

where n_h is the number of sampled pixels in stratum h , $s_{h,u}^2$ is the sample variance for the n_h values of u , where $u=A_h$ if the sample pixel is of the class being estimated and $u=0$ if the sample pixel is not of that class. The standard error for the global estimated area is the square root of the sum of the variances over all strata:

$$SE(\widehat{W}) = \sqrt{\sum_{h=1}^H \widehat{V}(\widehat{W}_h)}. \quad (9)$$

For area estimates of aggregations of classes, the aggregation was defined as a new class and the above calculations were performed for each. Additionally, the area that

is inundated each year for greater than 25, 50, 75, and 90 and equal to 100 percent of the time was calculated from the annual percent values of each sampled pixel.

A.II Accuracy estimation of water dynamics classes

Using the stratified sample of Landsat time-series data, we estimate user's and producer's accuracies for the trend classes. Each pixel within the global continental area had a non-zero inclusion probability, so the accuracy estimates are representative of the entire map. To estimate the accuracies for a given class c , one can estimate with equation (3) the four areas of intersection of map class c and non- c and reference class c and non- c within an error matrix and calculate the derived accuracies.

Standard error estimates require the per pixel inclusion probabilities and pairwise inclusion probabilities, designated by π_u and π_{uv} where u and v denote pixels. The pairwise inclusion probability is the probability that pixels u and v will both be included in the sample. The estimated variance for an estimated ratio (either user's or producer's accuracy) is:

$$\widehat{V}(\widehat{R}) = \frac{1}{\widehat{Z}^2} \sum \sum \left(1 - \frac{\pi_u \pi_v}{\pi_{uv}} \right) \frac{(y_u - \widehat{R}z_u)}{\pi_u} \frac{(y_v - \widehat{R}z_v)}{\pi_v} \quad (10)$$

where the double summation is over all possible pairs of sample pixels, and where the estimated ratio is $\widehat{R} = \frac{\widehat{Y}}{\widehat{Z}}$ and $\widehat{Y} = \sum_s y_u / \pi_u$ and $\widehat{Z} = \sum_s z_u / \pi_u$ (Särndal et al., 1992).

The inclusion probability for a pixel u in stratum h is $\pi_u = n_h a_u / A_h$ where a_u is the area of pixel u , n_h is the sample size from stratum h , and A_h is the total area of all pixels in stratum h . The pairwise inclusion probability between two sample pixels u and v depends on whether the two pixels are from the same stratum. If from different strata, the pairwise inclusion probability is simply the product of the inclusion

probabilities, $\pi_{uv} = \pi_u \pi_v$, which means $\left(1 - \frac{\pi_u \pi_v}{\pi_{uv}}\right) = \left(1 - \frac{\pi_u \pi_v}{\pi_u \pi_v}\right) = 0$ in equation (5).

If the two pixels are from the same stratum,

$$\pi_{h,uv} = \frac{(n_h - 1)\pi_{h,u}\pi_{h,v}}{[n_h - \pi_{h,u} - \pi_{h,v} + K]} \quad (11)$$

where $K = \sum_{U_h} \pi_u^2 / n_h$ and U_h denotes all pixels in stratum h , including those outside the sample (Hartley et al., 1962). Lastly, if u and v are the same pixel, $\pi_{uu} = \pi_u$. For both accuracy estimates, \hat{Y} is the estimated total area correctly mapped as class c and $y_u =$ area of pixel u if pixel u is both mapped as class c and has reference class c , otherwise, $y_u = 0$. For user's accuracy, \hat{Z} is the estimated area mapped as class c and $z_u =$ area of pixel u if pixel u is mapped as class c , otherwise $z_u = 0$. For producer's accuracy, \hat{Z} is the estimated area of reference class c and $z_u =$ area of pixel u if pixel u has reference class c , otherwise $z_u = 0$. For each estimated accuracy \hat{R} , $SE(\hat{R}) =$

$$\sqrt{\hat{V}(\hat{R})}.$$

Bibliography

- Abbott, B.W., Bishop, K., Zarnetske, J.P., Minaudo, C., Chapin, F.S., Krause, S., Hannah, D.M., Conner, L., Ellison, D., Godsey, S.E., Plont, S., Marçais, J., Kolbe, T., Huebner, A., Frei, R.J., Hampton, T., Gu, S., Buhman, M., Sara Sayedi, S., Ursache, O., Chapin, M., Henderson, K.D., Pinay, G., 2019. Human domination of the global water cycle absent from depictions and perceptions. *Nature Geoscience* 12, 533–540. <https://doi.org/10.1038/s41561-019-0374-y>
- Allen, G.H., Pavelsky, T.M., 2018. Global extent of rivers and streams. *Science* eaat0636. <https://doi.org/10.1126/science.aat0636>
- Alsdorf, D., Lettenmaier, D., Vörösmarty, C., 2003. The need for global, satellite-based observations of terrestrial surface waters. *Eos, Transactions American Geophysical Union* 84, 269–276. <https://doi.org/10.1029/2003EO290001>
- Arvidson, T., Goward, S., Gasch, J., Williams, D., 2006. Landsat-7 Long-Term Acquisition Plan. *Photogrammetric Engineering & Remote Sensing* 72, 1137–1146. <https://doi.org/10.14358/PERS.72.10.1137>
- Biggs, J., von Fumetti, S., Kelly-Quinn, M., 2017. The importance of small waterbodies for biodiversity and ecosystem services: implications for policy makers. *Hydrobiologia* 793, 3–39. <https://doi.org/10.1007/s10750-016-3007-0>
- Binding, C.E., Greenberg, T.A., Bukata, R.P., 2013. The MERIS Maximum Chlorophyll Index; its merits and limitations for inland water algal bloom monitoring. *Journal of Great Lakes Research, Remote Sensing of the Great Lakes and Other Inland Waters* 39, 100–107. <https://doi.org/10.1016/j.jglr.2013.04.005>
- Boland, D.H.P., 1976. Trophic Classification of Lakes Using LANDSAT-1 (ERTS-1) Multispectral Scanner Data. U.S. Environmental Protection Agency, Office of Research and Development, Corvallis Environmental Research Laboratory, Assessment and Criteria Development.
- Breiman, L., 1996. Bagging predictors. *Mach Learn* 24, 123–140. <https://doi.org/10.1007/BF00058655>
- Breiman, L., Friedman, J., Ohlsen, R., Stone, C., 1984. Classification and regression trees. Wadsworth International Group, Monterey, California.
- Brewer, K.R.W., Hanif, M., 1982. Sampling With Unequal Probabilities. Springer New York.

- Bwangoy, J.-R.B., Hansen, M.C., Roy, D.P., Grandi, G.D., Justice, C.O., 2010. Wetland mapping in the Congo Basin using optical and radar remotely sensed data and derived topographical indices. *Remote Sensing of Environment* 114, 73–86. <https://doi.org/10.1016/j.rse.2009.08.004>
- Cael, B.B., Seekell, D.A., 2016. The size-distribution of Earth's lakes. *Scientific Reports* 6, 29633. <https://doi.org/10.1038/srep29633>
- Cai, X., Haile, A.T., Magidi, J., Mapedza, E., Nhamo, L., 2017. Living with floods – Household perception and satellite observations in the Barotse floodplain, Zambia. *Physics and Chemistry of the Earth, Parts A/B/C, Infrastructural Planning for Water Security in Eastern and Southern Africa* 100, 278–286. <https://doi.org/10.1016/j.pce.2016.10.011>
- Carlson, B.Z., Hébert, M., Van Reeth, C., Bison, M., Laigle, I., Delestrade, A., 2020. Monitoring the Seasonal Hydrology of Alpine Wetlands in Response to Snow Cover Dynamics and Summer Climate: A Novel Approach with Sentinel-2. *Remote Sensing* 12, 1959. <https://doi.org/10.3390/rs12121959>
- Carroll, M., DiMiceli, C., Wooten, M., Hubbard, A., Sohlberg, R., Townshend, J., 2017. MOD44W MODIS/Terra Land Water Mask Derived from MODIS and SRTM L3 Global 250m SIN Grid V006. <https://doi.org/10.5067/MODIS/MOD44W.006>
- CBD, 2010. COP 10 Decision X/28: Inland waters biodiversity., 10th Meeting of the Conference of the Parties to the Convention on Biological Diversity. Nagoya, Japan.
- Chander, G., Markham, B.L., Helder, D.L., 2009. Summary of current radiometric calibration coefficients for Landsat MSS, TM, ETM+, and EO-1 ALI sensors.
- Chen, J., Zhu, X., Vogelmann, J.E., Gao, F., Jin, S., 2011. A simple and effective method for filling gaps in Landsat ETM+ SLC-off images. *Remote Sensing of Environment* 115, 1053–1064. <https://doi.org/10.1016/j.rse.2010.12.010>
- Chen, Jun, Chen, Jin, Liao, A., Cao, X., Chen, L., Chen, X., He, C., Han, G., Peng, S., Lu, M., Zhang, W., Tong, X., Mills, J., 2015. Global land cover mapping at 30m resolution: A POK-based operational approach. *ISPRS Journal of Photogrammetry and Remote Sensing, Global Land Cover Mapping and Monitoring* 103, 7–27. <https://doi.org/10.1016/j.isprsjprs.2014.09.002>
- Chevallier, P., Pouyaud, B., Suarez, W., Condom, T., 2011. Climate change threats to environment in the tropical Andes: glaciers and water resources. *Reg Environ Change* 11, 179–187. <https://doi.org/10.1007/s10113-010-0177-6>

- Coleman, J.M., 1969. Brahmaputra river: Channel processes and sedimentation. *Sedimentary Geology, Brahmaputra river: Channel processes and sedimentation* 3, 129–239. [https://doi.org/10.1016/0037-0738\(69\)90010-4](https://doi.org/10.1016/0037-0738(69)90010-4)
- Costanza, R., de Groot, R., Sutton, P., van der Ploeg, S., Anderson, S.J., Kubiszewski, I., Farber, S., Turner, R.K., 2014. Changes in the global value of ecosystem services. *Global Environmental Change* 26, 152–158. <https://doi.org/10.1016/j.gloenvcha.2014.04.002>
- Crist, E.P., 1985. A TM Tasseled Cap equivalent transformation for reflectance factor data. *Remote Sensing of Environment* 17, 301–306. [https://doi.org/10.1016/0034-4257\(85\)90102-6](https://doi.org/10.1016/0034-4257(85)90102-6)
- Dai, A., 2013. Increasing drought under global warming in observations and models. *Nature Clim. Change* 3, 52–58. <https://doi.org/10.1038/nclimate1633>
- Dai, A., Qian, T., Trenberth, E., Milliman, D., 2009. Changes in continental freshwater discharge from 1948 to 2004. *Journal of Climate* 22, 2773. <https://doi.org/10.1175/2008JCLI2592.1>
- Danaher, T., Collett, L., 2006. Development, optimisation and multi-temporal application of a simple Landsat based water index, in: *Proceedings of the 13th Australasian Remote Sensing and Photogrammetry Conference*, Canberra, Australia.
- Dang, T.D., Cochrane, T.A., Arias, M.E., 2018. Quantifying suspended sediment dynamics in mega deltas using remote sensing data: A case study of the Mekong floodplains. *International Journal of Applied Earth Observation and Geoinformation* 68, 105–115. <https://doi.org/10.1016/j.jag.2018.02.008>
- Davidson, N.C., 2014. How much wetland has the world lost? Long-term and recent trends in global wetland area. *Mar. Freshwater Res.* 65, 934–941. <https://doi.org/10.1071/MF14173>
- Davidson, N.C., Fluet-Chouinard, E., Finlayson, C.M., 2018. Global extent and distribution of wetlands: trends and issues. *Mar. Freshwater Res.* 69, 620–627. <https://doi.org/10.1071/MF17019>
- de Groot, R., Brander, L., van der Ploeg, S., Costanza, R., Bernard, F., Braat, L., Christie, M., Crossman, N., Ghermandi, A., Hein, L., Hussain, S., Kumar, P., McVittie, A., Portela, R., Rodriguez, L.C., ten Brink, P., van Beukering, P., 2012. Global estimates of the value of ecosystems and their services in monetary units. *Ecosystem Services* 1, 50–61. <https://doi.org/10.1016/j.ecoser.2012.07.005>
- DeVries, B., Huang, C., Armston, J., Huang, W., Jones, J.W., Lang, M.W., 2020. Rapid and robust monitoring of flood events using Sentinel-1 and Landsat

- data on the Google Earth Engine. *Remote Sensing of Environment* 240, 111664. <https://doi.org/10.1016/j.rse.2020.111664>
- Dibike, Y., Prowse, T., Saloranta, T., Ahmed, R., 2011. Response of Northern Hemisphere lake-ice cover and lake-water thermal structure patterns to a changing climate. *Hydrological Processes* 25, 2942–2953. <https://doi.org/10.1002/hyp.8068>
- Downing, J., 2006. Emerging global role of small lakes and ponds: little things mean a lot 15.
- Downing, J.A., Prairie, Y.T., Cole, J.J., Duarte, C.M., Tranvik, L.J., Striegl, R.G., McDowell, W.H., Kortelainen, P., Caraco, N.F., Melack, J.M., Middelburg, J.J., 2006. The global abundance and size distribution of lakes, ponds, and impoundments. *Limnology and Oceanography* 51, 2388–2397. <https://doi.org/10.4319/lo.2006.51.5.2388>
- Doxani, G., Vermote, E., Roger, J.-C., Gascon, F., Adriaensen, S., Frantz, D., Hagolle, O., Hollstein, A., Kirches, G., Li, F., Louis, J., Mangin, A., Pahlevan, N., Pflug, B., Vanhellemont, Q., 2018. Atmospheric Correction Inter-Comparison Exercise. *Remote Sensing* 10, 352. <https://doi.org/10.3390/rs10020352>
- Eggleston, H.S., Buendia, L., Miwa, K., Ngara, T., Tanabe, K., 2006. 2006 IPCC Guidelines for National Greenhouse Gas Inventories.
- Feng, M., Sexton, J.O., Channan, S., Townshend, J.R., 2016. A global, high-resolution (30-m) inland water body dataset for 2000: first results of a topographic–spectral classification algorithm. *International Journal of Digital Earth* 9, 113–133. <https://doi.org/10.1080/17538947.2015.1026420>
- Feyisa, G.L., Meilby, H., Fensholt, R., Proud, S.R., 2014. Automated Water Extraction Index: A new technique for surface water mapping using Landsat imagery. *Remote Sensing of Environment* 140, 23–35. <https://doi.org/10.1016/j.rse.2013.08.029>
- Fisher, A., Flood, N., Danaher, T., 2016. Comparing Landsat water index methods for automated water classification in eastern Australia. *Remote Sensing of Environment* 175, 167–182. <https://doi.org/10.1016/j.rse.2015.12.055>
- Fluet-Chouinard, E., Lehner, B., Rebelo, L.-M., Papa, F., Hamilton, S.K., 2015. Development of a global inundation map at high spatial resolution from topographic downscaling of coarse-scale remote sensing data. *Remote Sensing of Environment* 158, 348–361. <https://doi.org/10.1016/j.rse.2014.10.015>

- Frappart, F., Papa, F., Famiglietti, J.S., Prigent, C., Rossow, W.B., Seyler, F., 2008. Interannual variations of river water storage from a multiple satellite approach: A case study for the Rio Negro River basin. *Journal of Geophysical Research: Atmospheres* 113. <https://doi.org/10.1029/2007JD009438>
- Frappart, F., Papa, F., Güntner, A., Werth, S., Ramillien, G., Prigent, C., Rossow, W.B., Bonnet, M.-P., 2010. Interannual variations of the terrestrial water storage in the Lower Ob' Basin from a multisatellite approach. *Hydrology and Earth System Sciences* 14, 2443–2453. <https://doi.org/10.5194/hess-14-2443-2010>
- Gorelick, N., Hancher, M., Dixon, M., Ilyushchenko, S., Thau, D., Moore, R., 2017. Google Earth Engine: Planetary-scale geospatial analysis for everyone. *Remote Sensing of Environment, Big Remotely Sensed Data: tools, applications and experiences* 202, 18–27. <https://doi.org/10.1016/j.rse.2017.06.031>
- Grill, G., Lehner, B., Lumsdon, A.E., MacDonald, G.K., Zarfl, C., Liermann, C.R., 2015. An index-based framework for assessing patterns and trends in river fragmentation and flow regulation by global dams at multiple scales. *Environ. Res. Lett.* 10, 015001. <https://doi.org/10.1088/1748-9326/10/1/015001>
- Grill, G., Lehner, B., Thieme, M., Geenen, B., Tickner, D., Antonelli, F., Babu, S., Borrelli, P., Cheng, L., Crochetiere, H., Ehalt Macedo, H., Filgueiras, R., Goichot, M., Higgins, J., Hogan, Z., Lip, B., McClain, M.E., Meng, J., Mulligan, M., Nilsson, C., Olden, J.D., Opperman, J.J., Petry, P., Reidy Liermann, C., Sáenz, L., Salinas-Rodríguez, S., Schelle, P., Schmitt, R.J.P., Snider, J., Tan, F., Tockner, K., Valdujo, P.H., van Soesbergen, A., Zarfl, C., 2019. Mapping the world's free-flowing rivers. *Nature* 569, 215–221. <https://doi.org/10.1038/s41586-019-1111-9>
- Gutman, G., Byrnes, R.A., Masek, J., Covington, S., Justice, C., Franks, S., Headley, R., 2008. Towards monitoring land-cover and land-use changes at a global scale: the global land survey 2005. *Photogrammetric Engineering and Remote Sensing* 74, 5.
- Haig, S.M., Murphy, S.P., Matthews, J.H., Arismendi, I., Safeeq, M., 2019. Climate-Altered Wetlands Challenge Waterbird Use and Migratory Connectivity in Arid Landscapes. *Scientific Reports* 9, 4666. <https://doi.org/10.1038/s41598-019-41135-y>
- Han, L., Rundquist, D.C., 1994. The Response of both Surface Reflectance and the Underwater Light Field to Various Levels of Suspended Sediments: Preliminary Results. *American Society for Photogrammetry and Remote Sensing* 60, 1463–1471.

- Han, L., Rundquist, D.C., LIU, L.L., FRASER, R.N., SCHALLES, J.F., 1994. The spectral responses of algal chlorophyll in water with varying levels of suspended sediment. *International Journal of Remote Sensing* 15, 3707–3718. <https://doi.org/10.1080/01431169408954353>
- Hansen, M.C., Potapov, P.V., Moore, R., Hancher, M., Turubanova, S.A., Tyukavina, A., Thau, D., Stehman, S.V., Goetz, S.J., Loveland, T.R., Kommareddy, A., Egorov, A., Chini, L., Justice, C.O., Townshend, J.R.G., 2013. High-Resolution Global Maps of 21st-Century Forest Cover Change. *Science* 342, 850–853. <https://doi.org/10.1126/science.1244693>
- Heege, T., Kiselev, V., Wettle, M., Hung, N.N., 2014. Operational multi-sensor monitoring of turbidity for the entire Mekong Delta. *International Journal of Remote Sensing* 35, 2910–2926. <https://doi.org/10.1080/01431161.2014.890300>
- Hess, L.L., Melack, J.M., Affonso, A.G., Barbosa, C., Gastil-Buhl, M., Novo, E.M.L.M., 2015. Wetlands of the Lowland Amazon Basin: Extent, Vegetative Cover, and Dual-season Inundated Area as Mapped with JERS-1 Synthetic Aperture Radar. *Wetlands* 35, 745–756. <https://doi.org/10.1007/s13157-015-0666-y>
- Hu, S., Niu, Z., Chen, Y., 2017. Global Wetland Datasets: a Review. *Wetlands* 37, 807–817. <https://doi.org/10.1007/s13157-017-0927-z>
- Huang, C., Chen, Y., Zhang, S., Wu, J., 2018. Detecting, Extracting, and Monitoring Surface Water From Space Using Optical Sensors: A Review. *Reviews of Geophysics* 56, 333–360. <https://doi.org/10.1029/2018RG000598>
- International Commission on Large Dams, 2020. *World Register of Dams*.
- Jin, C., 2008. Biodiversity dynamics of freshwater wetland ecosystems affected by secondary salinisation and seasonal hydrology variation: a model-based study. *Hydrobiologia* 598, 257–270. <https://doi.org/10.1007/s10750-007-9161-7>
- Kaptué, A.T., Hanan, N.P., Prihodko, L., 2013. Characterization of the spatial and temporal variability of surface water in the Soudan-Sahel region of Africa. *Journal of Geophysical Research: Biogeosciences* 118, 1472–1483. <https://doi.org/10.1002/jgrg.20121>
- Kayranli, B., Scholz, M., Mustafa, A., Hedmark, Å., 2010. Carbon Storage and Fluxes within Freshwater Wetlands: a Critical Review. *Wetlands* 30, 111–124. <https://doi.org/10.1007/s13157-009-0003-4>
- Kirschke, S., Bousquet, P., Ciais, P., Saunois, M., Canadell, J.G., Dlugokencky, E.J., Bergamaschi, P., Bergmann, D., Blake, D.R., Bruhwiler, L., Cameron-Smith, P., Castaldi, S., Chevallier, F., Feng, L., Fraser, A., Heimann, M., Hodson,

- E.L., Houweling, S., Josse, B., Fraser, P.J., Krummel, P.B., Lamarque, J.-F., Langenfelds, R.L., Le Quéré, C., Naik, V., O'Doherty, S., Palmer, P.I., Pison, I., Plummer, D., Poulter, B., Prinn, R.G., Rigby, M., Ringeval, B., Santini, M., Schmidt, M., Shindell, D.T., Simpson, I.J., Spahni, R., Steele, L.P., Strode, S.A., Sudo, K., Szopa, S., van der Werf, G.R., Voulgarakis, A., van Weele, M., Weiss, R.F., Williams, J.E., Zeng, G., 2013. Three decades of global methane sources and sinks. *Nature Geoscience* 6, 813–823. <https://doi.org/10.1038/ngeo1955>
- Klein, I., Gessner, U., Dietz, A.J., Kuenzer, C., 2017. Global WaterPack – A 250m resolution dataset revealing the daily dynamics of global inland water bodies. *Remote Sensing of Environment* 198, 345–362. <https://doi.org/10.1016/j.rse.2017.06.045>
- Knoll, L.B., Sharma, S., Denfeld, B.A., Flaim, G., Hori, Y., Magnuson, J.J., Straile, D., Weyhenmeyer, G.A., 2019. Consequences of lake and river ice loss on cultural ecosystem services. *Limnology and Oceanography Letters* 4, 119–131. <https://doi.org/10.1002/lo2.10116>
- Liu, G., Schwartz, F.W., 2012. Climate-driven variability in lake and wetland distribution across the Prairie Pothole Region: From modern observations to long-term reconstructions with space-for-time substitution. *Water Resources Research* 48. <https://doi.org/10.1029/2011WR011539>
- Lopez, L.S., Hewitt, B.A., Sharma, S., 2019. Reaching a breaking point: How is climate change influencing the timing of ice breakup in lakes across the northern hemisphere? *Limnology and Oceanography* 64, 2621–2631. <https://doi.org/10.1002/lno.11239>
- Louis, J., Debaecker, V., Pflug, B., Main-Knorn, M., Bieniarz, J., Mueller-Wilm, U., Cadau, E., Gascon, F., 2016. SENTINEL-2 SEN2COR: L2A PROCESSOR FOR USERS 8.
- Lutz, A.F., Immerzeel, W.W., Shrestha, A.B., Bierkens, M.F.P., 2014. Consistent increase in High Asia's runoff due to increasing glacier melt and precipitation. *Nature Clim. Change* 4, 587–592. <https://doi.org/10.1038/nclimate2237>
- Margono, B.A., Bwangoy, J.-R.B., Potapov, P.V., Hansen, M.C., 2014. Mapping wetlands in Indonesia using Landsat and PALSAR data-sets and derived topographical indices. *Geo-spatial Information Science* 17, 60–71. <https://doi.org/10.1080/10095020.2014.898560>
- Martin, S., 2004. *An Introduction to Ocean Remote Sensing*. Cambridge University Press.

- McFeeters, S.K., 1996. The use of the Normalized Difference Water Index (NDWI) in the delineation of open water features. *International Journal of Remote Sensing* 17, 1425–1432. <https://doi.org/10.1080/01431169608948714>
- Mekonnen, M.M., Hoekstra, A.Y., 2016. Four billion people facing severe water scarcity. *Science Advances* 2, e1500323. <https://doi.org/10.1126/sciadv.1500323>
- Mitsch, W.J., Gosselink, J.G., 2015. *Wetlands*. John Wiley & Sons.
- Mitsch, W.J., Nahlik, A., Wolski, P., Bernal, B., Zhang, L., Ramberg, L., 2010. Tropical wetlands: seasonal hydrologic pulsing, carbon sequestration, and methane emissions. *Wetlands Ecol Manage* 18, 573–586. <https://doi.org/10.1007/s11273-009-9164-4>
- Mueller, N., Lewis, A., Roberts, D., Ring, S., Melrose, R., Sixsmith, J., Lymburner, L., McIntyre, A., Tan, P., Curnow, S., Ip, A., 2016. Water observations from space: Mapping surface water from 25 years of Landsat imagery across Australia. *Remote Sensing of Environment* 174, 341–352. <https://doi.org/10.1016/j.rse.2015.11.003>
- NOAA, N.C. for E.I., 2020. *State of the Climate: Global Climate Report for Annual 2019*.
- Odum, W.E., Odum, E.P., Odum, H.T., 1995. Nature's pulsing paradigm. *Estuaries* 18, 547. <https://doi.org/10.2307/1352375>
- Olmanson, L.G., Bauer, M.E., Brezonik, P.L., 2008. A 20-year Landsat water clarity census of Minnesota's 10,000 lakes. *Remote Sensing of Environment, Applications of Remote Sensing to Monitoring Freshwater and Estuarine Systems* 112, 4086–4097. <https://doi.org/10.1016/j.rse.2007.12.013>
- Olofsson, P., Foody, G.M., Herold, M., Stehman, S.V., Woodcock, C.E., Wulder, M.A., 2014. Good practices for estimating area and assessing accuracy of land change. *Remote Sensing of Environment* 148, 42–57. <https://doi.org/10.1016/j.rse.2014.02.015>
- Olofsson, P., Foody, G.M., Stehman, S.V., Woodcock, C.E., 2013. Making better use of accuracy data in land change studies: Estimating accuracy and area and quantifying uncertainty using stratified estimation. *Remote Sensing of Environment* 129, 122–131. <https://doi.org/10.1016/j.rse.2012.10.031>
- Papa, F., Prigent, C., Aires, F., Jimenez, C., Rossow, W.B., Matthews, E., 2010. Interannual variability of surface water extent at the global scale, 1993–2004. *Journal of Geophysical Research: Atmospheres* 115. <https://doi.org/10.1029/2009JD012674>

- Pekel, J.-F., Cottam, A., Gorelick, N., Belward, A.S., 2016. High-resolution mapping of global surface water and its long-term changes. *Nature* 540, 418–422. <https://doi.org/10.1038/nature20584>
- Penman, J., Green, C., Olofsson, P., Raison, J., Woodcock, C., Balzter, H., Baltuck, M., Foody, G.M., 2016. Integration of remote-sensing and ground-based observations for estimation of emissions and removals of greenhouse gases in forests: methods and guidance from the Global Forest Observations Initiative.
- Pham-Duc, B., Prigent, C., Aires, F., 2017. Surface Water Monitoring within Cambodia and the Vietnamese Mekong Delta over a Year, with Sentinel-1 SAR Observations. *Water* 9, 366. <https://doi.org/10.3390/w9060366>
- Pickens, A.H., Hansen, M.C., Hancher, M., Stehman, S.V., Tyukavina, A., Potapov, P., Marroquin, B., Sherani, Z., 2020. Mapping and sampling to characterize global inland water dynamics from 1999 to 2018 with full Landsat time-series. *Remote Sensing of Environment* 243, 111792. <https://doi.org/10.1016/j.rse.2020.111792>
- Poff, N.L., Allan, J.D., Bain, M.B., Karr, J.R., Prestegard, K.L., Richter, B.D., Sparks, R.E., Stromberg, J.C., 1997. The Natural Flow Regime. *BioScience* 47, 769–784. <https://doi.org/10.2307/1313099>
- Pope, R.M., Fry, E.S., 1997. Absorption spectrum (380–700 nm) of pure water. II. Integrating cavity measurements. *Appl. Opt.*, AO 36, 8710–8723. <https://doi.org/10.1364/AO.36.008710>
- Postel, S.L., Daily, G.C., Ehrlich, P.R., 1996. Human Appropriation of Renewable Fresh Water. *Science* 271, 785–788. <https://doi.org/10.1126/science.271.5250.785>
- Potapov, P., Hansen, M.C., Kommareddy, I., Kommareddy, A., Turubanova, S., Pickens, A., Adusei, B., Tyukavina, A., Ying, Q., 2020a. Landsat Analysis Ready Data for Global Land Cover and Land Cover Change Mapping. *Remote Sensing* 12, 426. <https://doi.org/10.3390/rs12030426>
- Potapov, P., Li, X., Hernandez-Serna, A., Tyukavina, A., Hansen, M.C., Kommareddy, A., Pickens, A., Turubanova, S., Tang, H., Silva, C.E., Armston, J., Dubayah, R., Blair, J.B., Hofton, M., 2020b. Mapping global forest canopy height through integration of GEDI and Landsat data. *Remote Sensing of Environment* 112165. <https://doi.org/10.1016/j.rse.2020.112165>
- Potapov, P.V., Turubanova, S.A., Tyukavina, A., Krylov, A.M., McCarty, J.L., Radeloff, V.C., Hansen, M.C., 2015. Eastern Europe’s forest cover dynamics from 1985 to 2012 quantified from the full Landsat archive. *Remote Sensing of Environment* 159, 28–43. <https://doi.org/10.1016/j.rse.2014.11.027>

- Prigent, C., Papa, F., Aires, F., Jimenez, C., Rossow, W.B., Matthews, E., 2012. Changes in land surface water dynamics since the 1990s and relation to population pressure. *Geophysical Research Letters* 39. <https://doi.org/10.1029/2012GL051276>
- Prowse, T., Alfredsen, K., Beltaos, S., Bonsal, B., Duguay, C., Korhola, A., McNamara, J., Pienitz, R., Vincent, W.F., Vuglinsky, V., Weyhenmeyer, G.A., 2011. Past and Future Changes in Arctic Lake and River Ice. *AMBIO* 40, 53–62. <https://doi.org/10.1007/s13280-011-0216-7>
- Qiu, S., Zhu, Z., He, B., 2019. Fmask 4.0: Improved cloud and cloud shadow detection in Landsats 4–8 and Sentinel-2 imagery. *Remote Sensing of Environment* 231, 111205. <https://doi.org/10.1016/j.rse.2019.05.024>
- Raymond, P.A., Hartmann, J., Lauerwald, R., Sobek, S., McDonald, C., Hoover, M., Butman, D., Striegl, R., Mayorga, E., Humborg, C., Kortelainen, P., Dürr, H., Meybeck, M., Ciais, P., Guth, P., 2013. Global carbon dioxide emissions from inland waters. *Nature* 503, 355–359. <https://doi.org/10.1038/nature12760>
- Rebelo, L.-M., Finlayson, C.M., Strauch, A., Rosenqvist, A., Perennou, C., Tøttrup, C., Hilarides, L., Paganini, M., Wielaard, N., Siegert, F., Ballhorn, U., Navratil, P., Franke, J., Davidson, N., 2018. The use of Earth Observation for wetland inventory, assessment and monitoring: An information source for Ramsar Convention on Wetlands.
- Reid, A.J., Carlson, A.K., Creed, I.F., Eliason, E.J., Gell, P.A., Johnson, P.T.J., Kidd, K.A., MacCormack, T.J., Olden, J.D., Ormerod, S.J., Smol, J.P., Taylor, W.W., Tockner, K., Vermaire, J.C., Dudgeon, D., Cooke, S.J., 2019. Emerging threats and persistent conservation challenges for freshwater biodiversity. *Biological Reviews* 94, 849–873. <https://doi.org/10.1111/brv.12480>
- Restrepo, J.D., Kjerfve, B., 2000. Magdalena river: interannual variability (1975–1995) and revised water discharge and sediment load estimates. *Journal of Hydrology* 235, 137–149. [https://doi.org/10.1016/S0022-1694\(00\)00269-9](https://doi.org/10.1016/S0022-1694(00)00269-9)
- Rodell, M., Famiglietti, J.S., Wiese, D.N., Reager, J.T., Beaudoing, H.K., Landerer, F.W., Lo, M.-H., 2018. Emerging trends in global freshwater availability. *Nature* 1. <https://doi.org/10.1038/s41586-018-0123-1>
- Šmejkalová, T., Edwards, M.E., Dash, J., 2016. Arctic lakes show strong decadal trend in earlier spring ice-out. *Scientific Reports* 6, 38449. <https://doi.org/10.1038/srep38449>
- Smith, R.C., Baker, K.S., 1981. Optical properties of the clearest natural waters (200–800 nm). *Appl. Opt.*, AO 20, 177–184. <https://doi.org/10.1364/AO.20.000177>

- SRTM Data Editing Rules, 2003. USGS.
https://dds.cr.usgs.gov/srtm/version2_1/Documentation/SRTM_edit_rules.pdf,
Accessed dat: 5 April 2019.
- Stehman, S.V., 2014. Estimating area and map accuracy for stratified random sampling when the strata are different from the map classes. *International Journal of Remote Sensing* 35, 4923–4939.
<https://doi.org/10.1080/01431161.2014.930207>
- Stehman, S.V., 2013. Estimating area from an accuracy assessment error matrix. *Remote Sensing of Environment* 132, 202–211.
<https://doi.org/10.1016/j.rse.2013.01.016>
- Stephenson, S.R., Smith, L.C., Agnew, J.A., 2011. Divergent long-term trajectories of human access to the Arctic. *Nature Climate Change* 1, 156–160.
<https://doi.org/10.1038/nclimate1120>
- Straub, C.L., Koontz, S.R., Loomis, J.B., 2019. Economic valuation of landsat imagery (USGS Numbered Series No. 2019–1112), Open-File Report. U.S. Geological Survey, Reston, VA.
- Tarboton, D.G., Bras, R.L., Rodriguez-Iturbe, I., 1988. The fractal nature of river networks. *Water Resources Research* 24, 1317–1322.
<https://doi.org/10.1029/WR024i008p01317>
- Tarrio, K., Tang, X., Masek, J.G., Claverie, M., Ju, J., Qiu, S., Zhu, Z., Woodcock, C.E., 2020. Comparison of cloud detection algorithms for Sentinel-2 imagery. *Science of Remote Sensing* 2, 100010.
<https://doi.org/10.1016/j.srs.2020.100010>
- Tessler, Z.D., Vörösmarty, C.J., Grossberg, M., Gladkova, I., Aizenman, H., 2016. A global empirical typology of anthropogenic drivers of environmental change in deltas. *Sustain Sci* 11, 525–537. <https://doi.org/10.1007/s11625-016-0357-5>
- Ticehurst, C., Guerschman, J.P., Chen, Y., 2014. The Strengths and Limitations in Using the Daily MODIS Open Water Likelihood Algorithm for Identifying Flood Events. *Remote Sensing* 6, 11791–11809.
<https://doi.org/10.3390/rs61211791>
- Tockner, K., Stanford, J.A., 2002. Riverine flood plains: present state and future trends. *Environmental Conservation* 29, 308–330.
<https://doi.org/10.1017/S037689290200022X>
- Tong, S.T.Y., Chen, W., 2002. Modeling the relationship between land use and surface water quality. *J. Environ. Manage.* 66, 377–393.
<https://doi.org/10.1006/jema.2002.0593>

- Tucker, C.J., Grant, D.M., Dykstra, J.D., 2004. NASA's Global Orthorectified Landsat Data Set. <https://doi.org/10.14358/pers.70.3.313>
- Tulbure, M.G., Broich, M., Stehman, S.V., Kommareddy, A., 2016. Surface water extent dynamics from three decades of seasonally continuous Landsat time series at subcontinental scale in a semi-arid region. *Remote Sensing of Environment* 178, 142–157. <https://doi.org/10.1016/j.rse.2016.02.034>
- Twele, A., Cao, W., Plank, S., Martinis, S., 2016. Sentinel-1-based flood mapping: a fully automated processing chain. *International Journal of Remote Sensing* 37, 2990–3004. <https://doi.org/10.1080/01431161.2016.1192304>
- UN Water, 2018. Sustainable Development Goal 6: synthesis report 2018 on water and sanitation, United Nations publications. United Nations, New York, New York, United States of America.
- UNEP, 2016. A Snapshot Report of the World's Water Quality: Towards a global assessment. United Nations Environment Programme, Nairobi, Kenya.
- U.S. Army Corps of Engineers, 2018. National inventory of dams. Washington, DC : US Army Corps of Engineers : Federal Emergency Management Agency.
- Vermote, E., Justice, C., Claverie, M., Franch, B., 2016. Preliminary analysis of the performance of the Landsat 8/OLI land surface reflectance product. *Remote Sensing of Environment, Landsat 8 Science Results* 185, 46–56. <https://doi.org/10.1016/j.rse.2016.04.008>
- Verpoorter, C., Kutser, T., Seekell, D.A., Tranvik, L.J., 2014. A global inventory of lakes based on high-resolution satellite imagery. *Geophysical Research Letters* 41, 6396–6402. <https://doi.org/10.1002/2014GL060641>
- Vincent, W.F., Callaghan, T.V., Dahl-Jensen, D., Johansson, M., Kovacs, K.M., Michel, C., Prowse, T., Reist, J.D., Sharp, M., 2011. Ecological Implications of Changes in the Arctic Cryosphere. *Ambio* 40, 87–99. <https://doi.org/10.1007/s13280-011-0218-5>
- Wang, X., Xie, S., Zhang, X., Chen, C., Guo, H., Du, J., Duan, Z., 2018. A robust Multi-Band Water Index (MBWI) for automated extraction of surface water from Landsat 8 OLI imagery. *International Journal of Applied Earth Observation and Geoinformation* 68, 73–91. <https://doi.org/10.1016/j.jag.2018.01.018>
- White, L., Brisco, B., Daboor, M., Schmitt, A., Pratt, A., 2015. A Collection of SAR Methodologies for Monitoring Wetlands. *Remote Sensing* 7, 7615–7645. <https://doi.org/10.3390/rs70607615>

- Whitehead, P.G., WILBY, R.L., BATTARBEE, R.W., KERNAN, M., WADE, A.J., 2009. A review of the potential impacts of climate change on surface water quality. *Hydrological Sciences Journal* 54, 101–123. <https://doi.org/10.1623/hysj.54.1.101>
- Wieland, M., Martinis, S., 2020. Large-scale surface water change observed by Sentinel-2 during the 2018 drought in Germany. *International Journal of Remote Sensing* 41, 4742–4756. <https://doi.org/10.1080/01431161.2020.1723817>
- Wik, M., Varner, R.K., Anthony, K.W., MacIntyre, S., Bastviken, D., 2016. Climate-sensitive northern lakes and ponds are critical components of methane release. *Nature Geoscience* 9, 99–105. <https://doi.org/10.1038/ngeo2578>
- Woolnough, D.A., Downing, J.A., Newton, T.J., 2009. Fish movement and habitat use depends on water body size and shape. *Ecology of Freshwater Fish* 18, 83–91. <https://doi.org/10.1111/j.1600-0633.2008.00326.x>
- World Meteorological Organization (WMO), (UNESCO) United Nations Educational, S. and C.O., Commission, (IOC) Intergovernmental Oceanographic, Programme, (UNEP) United Nations Environment, Unions, (ICSU) International Council of Scientific, 2016. GCOS, 200. The Global Observing System for Climate : Implementation Needs. WMO, Geneva.
- Wulder, M.A., Loveland, T.R., Roy, D.P., Crawford, C.J., Masek, J.G., Woodcock, C.E., Allen, R.G., Anderson, M.C., Belward, A.S., Cohen, W.B., Dwyer, J., Erb, A., Gao, F., Griffiths, P., Helder, D., Hermosilla, T., Hipple, J.D., Hostert, P., Hughes, M.J., Huntington, J., Johnson, D.M., Kennedy, R., Kilic, A., Li, Z., Lymburner, L., McCorkel, J., Pahlevan, N., Scambos, T.A., Schaaf, C., Schott, J.R., Sheng, Y., Storey, J., Vermote, E., Vogelmann, J., White, J.C., Wynne, R.H., Zhu, Z., 2019. Current status of Landsat program, science, and applications. *Remote Sensing of Environment* 225, 127–147. <https://doi.org/10.1016/j.rse.2019.02.015>
- Wulder, M.A., Masek, J.G., Cohen, W.B., Loveland, T.R., Woodcock, C.E., 2012. Opening the archive: How free data has enabled the science and monitoring promise of Landsat. *Remote Sensing of Environment, Landsat Legacy Special Issue* 122, 2–10. <https://doi.org/10.1016/j.rse.2012.01.010>
- Wulder, M.A., White, J.C., Loveland, T.R., Woodcock, C.E., Belward, A.S., Cohen, W.B., Fosnight, E.A., Shaw, J., Masek, J.G., Roy, D.P., 2016. The global Landsat archive: Status, consolidation, and direction. *Remote Sensing of Environment, Landsat 8 Science Results* 185, 271–283. <https://doi.org/10.1016/j.rse.2015.11.032>

- Wurtsbaugh, W.A., Miller, C., Null, S.E., DeRose, R.J., Wilcock, P., Hahnenberger, M., Howe, F., Moore, J., 2017. Decline of the world's saline lakes. *Nature Geoscience* 10, 816. <https://doi.org/10.1038/ngeo3052>
- Xu, H., 2006. Modification of normalised difference water index (NDWI) to enhance open water features in remotely sensed imagery. *International Journal of Remote Sensing* 27, 3025–3033. <https://doi.org/10.1080/01431160600589179>
- Yamazaki, D., Trigg, M.A., Ikeshima, D., 2015. Development of a global ~90m water body map using multi-temporal Landsat images. *Remote Sensing of Environment* 171, 337–351. <https://doi.org/10.1016/j.rse.2015.10.014>
- Yang, Xiao, Pavelsky, T.M., Allen, G.H., 2020. The past and future of global river ice. *Nature* 577, 69–73. <https://doi.org/10.1038/s41586-019-1848-1>
- Yang, Xiucheng, Qin, Q., Yésou, H., Ledauphin, T., Koehl, M., Grussenmeyer, P., Zhu, Z., 2020. Monthly estimation of the surface water extent in France at a 10-m resolution using Sentinel-2 data. *Remote Sensing of Environment* 244, 111803. <https://doi.org/10.1016/j.rse.2020.111803>
- Ying, Q., Hansen, M.C., Potapov, P.V., Tyukavina, A., Wang, L., Stehman, S.V., Moore, R., Hancher, M., 2017. Global bare ground gain from 2000 to 2012 using Landsat imagery. *Remote Sensing of Environment* 194, 161–176. <https://doi.org/10.1016/j.rse.2017.03.022>
- Zarfl, C., Lumsdon, A.E., Berlekamp, J., Tydecks, L., Tockner, K., 2015. A global boom in hydropower dam construction. *Aquat Sci* 77, 161–170. <https://doi.org/10.1007/s00027-014-0377-0>
- Zhang, G., Yao, T., Xie, H., Zhang, K., Zhu, F., 2014. Lakes' state and abundance across the Tibetan Plateau. *Chin. Sci. Bull.* 59, 3010–3021. <https://doi.org/10.1007/s11434-014-0258-x>
- Zhang, M., Chen, F., Liang, D., Tian, B., Yang, A., 2020. Use of Sentinel-1 GRD SAR Images to Delineate Flood Extent in Pakistan. *Sustainability* 12, 5784. <https://doi.org/10.3390/su12145784>
- Zhao, X., Huang, Y., Jia, Z., Liu, H., Song, T., Wang, Yuesi, Shi, L., Song, C., Wang, Yiyong, 2008. Effects of the conversion of marshland to cropland on water and energy exchanges in northeastern China. *Journal of Hydrology* 355, 181–191. <https://doi.org/10.1016/j.jhydrol.2008.03.019>
- Zou, Z., Xiao, X., Dong, J., Qin, Y., Doughty, R.B., Menarguez, M.A., Zhang, G., Wang, J., 2018. Divergent trends of open-surface water body area in the contiguous United States from 1984 to 2016. *PNAS* 201719275. <https://doi.org/10.1073/pnas.1719275115>